Oxygen surface exchange and oxidative dehydrogenation on oxide ion conductors

Chunlin Song

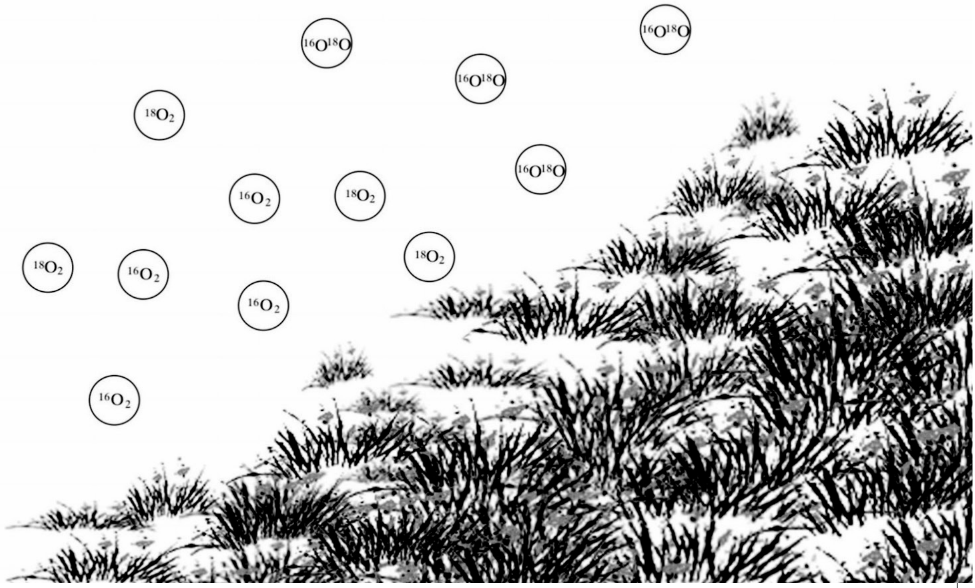

Oxygen surface exchange and oxidative dehydrogenation on oxide ion conductors

Graduation committee:

Promotor:	prof. dr. ir. A. Nijmeijer	University of Twente
Assistant promotor:	dr. H.J.M. Bouwmeester	University of Twente
Committee members:	dr. B.A. Boukamp	University of Twente
	prof. dr. ir. L. Lefferts	University of Twente
	prof. dr. ing. D.H.A. Blank	University of Twente
	prof. C.S. Chen	USTC (University of Science and Technology of China)
	prof. dr. ir. M. van Sint-Annaland	TU/e (Eindhoven University of Technology)

The research described in this thesis was carried out in the Inorganic Membranes Group and the MESA$^+$ Institute of Nanotechnology at the University of Twente, Enschede, the Netherlands. This project was financially supported by ASPECT program, ACTS (Advanced Catalytic Technologies for Sustainability, the Netherlands) under project number 053.62.004.

Oxygen surface exchange and oxidative dehydrogenation on oxide ion conductors

Chunlin Song, PhD Thesis, University of Twente, the Netherlands

ISBN: 978-90-365-3410-9
DOI: 10.3990/1.9789036534109

OXYGEN SURFACE EXCHANGE AND OXIDATIVE DEHYDROGENATION ON OXIDE ION CONDUCTORS

DISSERTATION

to obtain
the degree of doctor at the University of Twente,
on the authority of the rector magnificus,
prof. dr. H. Brinksma,
on account of the decision of the graduation committee,
to be publicly defended
on Wednesday, October 17, 2012 at 16:45 hrs.

by
Chunlin Song
born on 10th of January, 1979
in Lezhi County, Sichuan Province, P.R. China

This dissertation has been approved by,

Promotor :	prof. dr. ir. A. Nijmeijer
Assistant promotor :	dr. H.J.M. Bouwmeester

- To my family

采菊东篱下，悠然见南山
-陶渊明

Table of contents

1 Introduction

2 Pulse-response ^{18}O-^{16}O isotopic exchange – A novel method for rapid determination of the rate of oxygen surface exchange on oxide ion conductors

Supplementary information

3 Importance of oxygen vacancies in oxygen surface exchange on phases $La_{1-x}Sr_xCoO_{3-\delta}$

4 Influence of CO_2 on stability and surface oxygen exchange of the perovskite-type $Ba_{0.5}Sr_{0.5}Co_{0.8}Fe_{0.2}O_{3-\delta}$

5 Oxidative dehydrogenation of alkanes using oxygen-permeable ceramic membrane reactor

6 Evaluation and recommendations

Chapter 1

Introduction

Abstract

In this chapter, oxide-ion conductors and their major applications are introduced. The importance of the oxygen surface exchange reaction in determining oxygen transport is emphasized. Next, methods to study the oxygen exchange between gaseous oxygen and lattice oxygen are briefly described. Finally, the scope of this thesis is presented.

1.1 General introduction

Oxide-ion conductors are solid oxides that contain highly mobile oxygen ions. Some are solid electrolytes, with a pure oxide-ion conductivity, others are mixed oxide-ion and electron conductors (MIECs) [1]. The materials form the basis of devices that have a huge market potential, including their use in solid-oxide fuel cells (SOFCs) and as oxygen separation membranes, as discussed below. Oxygen transport in known oxide-ion conductors is mediated by highly mobile oxygen vacancies or interstitial oxygens. Since oxygen transport occurs diffusively, where the oxide ion must overcome an energetic barrier to hop to an adjacent vacant or interstitial site in the oxide lattice, substantial oxide-ion conductivity is only obtained at elevated temperature, typically in the range 700-1000 °C.

Oxides with a pure oxide-ion conductivity can be used as a solid electrolyte in a solid oxide fuel cell (SOFC), where the solid electrolyte acts as a separator between air and fuel streams [1, 2]. The SOFC electrochemically converts the chemical energy of a fuel into electrical power. The working principle is shown in Fig. 1.1. Major advantages

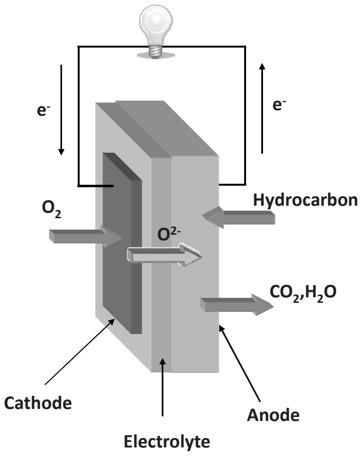

Fig. 1.1 Operating principle of a solid oxide fuel cell

of the SOFC over other types of fuel cells include high efficiency, flexibility in the choice of fuel (such as carbon-based fuels) and low emission. Popular solid oxide electrolytes include doped ZrO_2 and CeO_2 with a fluorite structure [3], perovskite oxides, e.g., $La_{0.9}Sr_{0.1}Ga_{0.8}Mg_{0.2}O_{3-\delta}$ [4], and the recently developed complex oxides, e.g., doped $Bi_2VO_{5+\delta}$ [5]. Some other uses of solid oxide electrolytes are in oxygen pumps and oxygen sensors [6].

Membranes fabricated from mixed oxygen ionic-electronic conducting oxides can separate oxygen from air, or any other oxygen-containing gas, contacted to one side of the membrane, by exposing the other side of the membrane to a purge gas, or a reactive gas mixture, as long as the oxygen partial pressure at this side of the membrane is lower than that at the air side of the membrane. The ceramic membranes, commonly referred to as oxygen-transport membrane, are fabricated dense, free of cracks and connected-through porosity. The membranes have infinite selectivity for oxygen separation over other gases, because only oxygen ions can occupy and be transported among the crystal lattice positions. A simultaneous transport of electronic charge carriers occurs to maintain overall charge neutrality. The oxygen exiting the surface at the permeate side of the

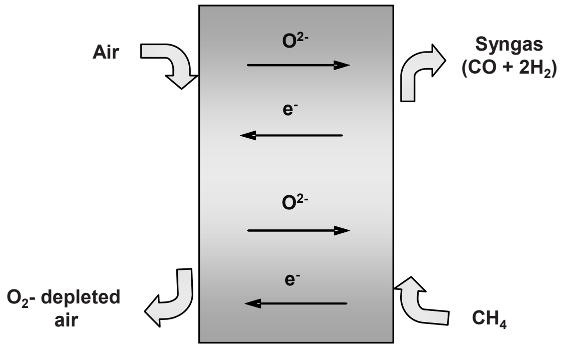

Fig. 1.2 Operating principle of a ceramic membrane reactor employing an oxygen selective membrane for the partial oxidation of methane to syngas

membrane may be used, for example, for oxidative conversion of hydrocarbons. Research in the field has increased substantially over the last decades, which is evidenced by numerous publications and filing of patents. Both integration of the membrane technology in the production of syngas[1] (Fig. 1.2) and in power plant scenarios for capturing (and storage) of CO_2 are explored intensively to date, since integration eliminates the need of costly oxygen produced by cryogenic distillation [7, 8].

1.2 Importance of the oxygen surface exchange reaction

The rate of oxygen permeation through a mixed oxygen ionic-electronic conducting membrane is determined not only by the rate of oxygen diffusion through the oxide lattice, but also by the interfacial kinetics of oxygen exchange at the membrane surfaces. Under steady-state conditions, the available oxygen chemical potential gradient across the membrane, which is the driving force for oxygen transport, is distributed across the membrane in such manner that the rate determining process receives the greater

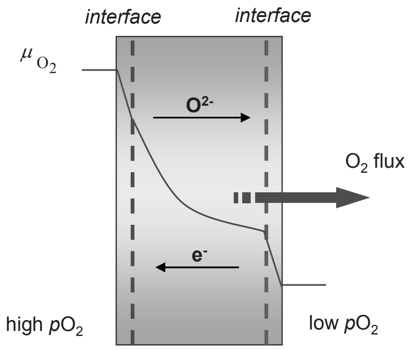

Fig. 1.3 The drop in oxygen chemical potential across a mixed conducting oxide membrane during steady-state oxygen permeation

---

[1] Syngas, a mixture of carbon monoxide and hydrogen, is an important intermediate for the gas-to-liquid (GTL) process for the conversion of natural gas to liquid fuels.

proportion (Fig. 1.3). The oxygen flux can be increased by reducing the thickness of the membrane, until its thickness becomes less than a characteristic value, L_c, at which point the oxygen flux is under mixed control of the surface exchange kinetics and bulk diffusion. No appreciable gain in the oxygen flux can be obtained by fabricating thinner membranes, unless the rate of the oxygen surface exchange kinetics at the relevant gas/solid interface(s) can be significantly increased.

The mixed conducting oxides represent a class of materials that are also actively studied as electrocatalysts. By using them as the cathode in the SOFC, the oxygen reduction is no longer confined at the triple phase boundary as in the case of precious metal electrodes or commonly employed Sr-doped $LaMnO_3$. In fact, the oxygen exchange process expands to all over the available surface area of the mixed conductor. Very good electrode performance has been experimentally observed for $La_2NiO_{4+\delta}$ [9], $La_{1-x}Sr_xCo_{1-y}Fe_yO_{3-\delta}$ [10], $Ba_{1-x}Sr_xCo_{1-y}Fe_yO_{3-\delta}$ [11], $Sm_{1-x}Sr_xCoO_{3-\delta}$ [12] and $PrBaCo_2O_{5+\delta}$ [13].

1.3 Experimental methods to study surface oxygen exchange

In this section, commonly used methods for measurement of the oxygen surface exchange kinetics are briefly described.

The first of the methods to be discussed is *Isotopic Exchange Depth-Profiling* (IEDP), involving the *ex-situ* analysis of the ^{18}O diffusion profile in a solid after an exchange anneal at elevated temperature by secondary ion mass spectrometry [14-17]. Analysis enables determination of both the tracer diffusion coefficient, D^*, and the surface exchange coefficient, k^*. During the anneal, the rate of isotopic exchange across the gas/solid interfacial surface (at ordinate $x = 0$) is taken to be proportional to the difference in the ^{18}O concentrations in the gas phase and solid, which leads to the following boundary condition for the tracer flux j^* [18]:

$$j^* = -D^* c_\mathrm{o} \cdot \left. \frac{\partial f_\mathrm{s}^*(t)}{\partial x} \right|_{x=0} = k^* c_\mathrm{o} \left(f_\mathrm{g}^* - f_\mathrm{s}^*(t) \right) \tag{1.1}$$

where c_o is the (exchangeable) concentration of oxygen anions in the oxide, and $f_\mathrm{s}^*(t)$ and $f_\mathrm{g}^*(t)$ refer to the ^{18}O-isotope fractions in the solid and gas phase, respectively. The latter is usually taken to be constant. Fitting the experimental data to the appropriate diffusion equation yields both k^* in [cm·s^{-1}] and D^* in [cm^2·s^{-1}]. In accord with Eq. 1.1, the balanced surface exchange rate $\Re_0$ in [mol O·cm^{-2}·s^{-1}] at equilibrium is: $\Re_0 = k^* c_\mathrm{o}$.

In recent years, IEDP has been applied extensively for the measurement of the exchange kinetics of acceptor-doped fluorite-structured and perovskite-structured oxides [14, 16]. Analysis, however, is prone to errors if during the exchange anneal boundary condition (1.1) is not maintained, due to either depletion and/or limited diffusion of ^{18}O in the gas phase. A pre-requisite of isotopic exchange measurements is that measurements are conducted at isothermal and iso-$p\mathrm{O}_2$ conditions. An additional drawback of the IEDP method is that the method involves a number of rapid heating, pre- and diffusion annealing, and quenching steps (to facilitate switching between the anneal gas and the ^{18}O-enriched gas with the same $p\mathrm{O}_2$ and the depth-profiling analysis at room temperature, and to avoid exchange during heating/cooling steps). Not only is this time consuming, but also one must exercise great care in order to avoid introducing additional artifacts and errors into the kinetic parameters [19, 20].

Another method for measurement of the oxygen surface exchange is by *in-situ* monitoring the time-dependent equilibration of the ^{18}O-isotope fraction in the gas phase upon exchange at elevated temperature using gas mass spectrometry. During this experiment, a powder of the solid oxide is confined in a closed vessel, preferably with forced gas circulation to prevent external mass transport limitations. The differential equation, describing the exchange of oxygen between the gas phase and the oxide, is given by

$$j^* = \frac{2a}{S} \cdot \frac{\partial f_\mathrm{g}^*(t)}{\partial t} = -k_\mathrm{g} c_\mathrm{g} \left(f_\mathrm{g}^*(t) - f_\mathrm{s}^*(t) \right) \tag{1.2}$$

where S is the available area for exchange, a the number of O_2 molecules in the gas phase, and k_g [cm·s^{-1}] is the appropriate surface exchange coefficient in the gas phase. Under the assumption of fast diffusion in the oxide, a condition leading to flat diffusion profiles in the oxide, and taking into account the proper boundary conditions, it follows that

$$\frac{f_\mathrm{g}^*(t) - f_\mathrm{g}^*(\infty)}{f_\mathrm{g}^*(0) - f_\mathrm{g}^*(\infty)} = \exp\left(-k_\mathrm{g} c_\mathrm{g} \left(\frac{2a+m}{2am} \right) t \right) \tag{1.3}$$

where c_g is the concentration of oxygens in the gas phase, $f_\mathrm{g}^*(0)$ and $f_\mathrm{g}^*(\infty)$ are the corresponding initial and final ^{18}O-isotope fractions, respectively [21], and m the total number of (exchangeable) oxygen atoms in the solid. In accord with Eq. 1.3, the surface exchange rate is expressed by $\Re_0 = k_\mathrm{g} c_\mathrm{g}$ [mol-O·cm^{-2}·s^{-1}]. Eq. 1.4 shows the relationships between the various kinetic parameters describing surface exchange,

$$k^* = \frac{\Re_0}{c_\mathrm{o}} \qquad k_\mathrm{g} = \frac{\Re_0}{c_\mathrm{g}} \tag{1.4}$$

noting that the surface exchange rate coefficient k^* and surface exchange rate $\Re_0$ are commonly employed in literature to compare data obtained for different materials.

As an example, Fig. 1.4 shows the time-dependent distribution of isotopomers with masses 32, 34 and 36 as measured for 25 mol % erbia-stabilized bismuth oxide [22, 23]. The isotopic scrambling mechanism, i.e. the transient distribution of ^{18}O over the gas phase oxygen molecules during exchange, holds kinetic information with regard to the exchange kinetics, enabling to distinguish between oxygen adsorption and oxygen incorporation as the rate determining step of the exchange reaction.

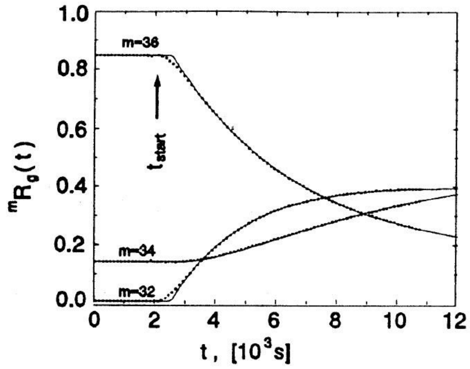

Fig. 1.4 Transient distribution of oxygen isotopomers ($^{18}O_2$, $^{16}O^{18}O$, $^{16}O_2$) upon oxygen isotopic exchange of $Bi_{0.75}Er_{0.25}O_3$ (BE25) powder. Data were recorded at a temperature of 873 K and oxygen partial pressure 0.25 atm. Reproduced from Ref. 23.

Thirdly, chemical relaxation methods offer a tool for determination of the relevant transport parameters of oxide-ion conducting ceramics [24-28]. Here, the change in oxygen stoichiometry following a small, instantaneous change of the oxygen partial pressure surrounding the sample brings about a change in weight [28], electrical conductivity [24-27] (referred to as *Electrical Conductivity Relaxation* (ECR)), which is monitored *in-situ* as a function of time. Here, the expression for the boundary condition (at x = 0) during equilibration of the oxygen concentration $c_o(t)$ to the final value $c_o(\infty)$ fixed by the oxygen partial pressure in the gas phase is

$$j = -\tilde{D} \cdot \left. \frac{\partial c_o(t)}{\partial x} \right|_{x=0} = \tilde{k}_s \left(c_o(\infty) - c_o(t) \right) \qquad (1.5)$$

where $\tilde{k}_s$ [cm·s^{-1}] and $\tilde{D}$ [cm^2·s^{-1}] are the pertinent surface exchange and diffusion coefficients. For the linearized boundary conditions to hold, the step change made in pO_2 needs to be small, since both $\tilde{k}_s$ [cm·s^{-1}] and $\tilde{D}$ [cm^2·s^{-1}] usually are dependent on pO_2.

The notation with the tilde refers to the chemical non-equilibrium conditions associated with chemical relaxation type of experiments. Their values are, respectively, related to the surface exchange coefficient k^*

$$\tilde{k}_s = k^* \gamma \tag{1.6}$$

and the self diffusion coefficient D_s or the tracer diffusion coefficient D^* (ignoring correlation effects) by

$$\tilde{D} = D_s \gamma \approx D^* \gamma \tag{1.7}$$

where γ is the thermodynamic factor

$$\gamma = \frac{1}{2} \frac{\partial \ln p\mathrm{O}_2}{\partial \ln c_o} \tag{1.8}$$

relating differential changes in the oxygen concentration to changes in oxygen partial pressure $p\mathrm{O}_2$.

Finally, another method, referred to as *Steady-State Isotopic Transient Kinetic Analysis* technique (SSITKA) is frequently used in studies of heterogeneous catalysis [29]. The measurement involves the isothermal switching of the feed stream after steady state has been achieved to an equivalent feed stream having labelled one of the reactants, and monitoring the dynamic catalyst response at the outlet of the reactor. SSITKA has also recently been explored to study oxygen surface exchange of $La_{0.8}Sr_{0.2}MnO_{3-\delta}$ and $La_{0.6}Sr_{0.4}Co_{0.2}Fe_{0.8}O_{3-\delta}$ [30].

1.4 Scope of this thesis

Knowledge of the rate of oxygen exchange between gaseous oxygen and oxygen from the oxide is of fundamental importance for the development of devices incorporating high-temperature solid oxide ion conductors, including solid oxide fuel cells and oxygen separation membranes. In Chapter 2, a novel pulse ^{18}O-^{16}O isotopic exchange method for determination of the surface exchange rate of oxide ion conductors is presented. Compared to other methods, the pulse method allows a rapid evaluation of the oxygen surface exchange rate under different operating conditions. The method is exploited to study the influence of oxygen vacancies on oxygen exchange on phases $La_{1-x}Sr_xCoO_{3-\delta}$ ($0.2 \leqslant x \leqslant 0.5$), as described in Chapter 3. In Chapter 4, the influence of CO_2 in the gas phase on the rate of oxygen exchange on the perovskite-type oxide $Ba_{0.5}Sr_{0.5}Co_{0.8}Fe_{0.2}O_{3-\delta}$ (BSCF) is investigated. In Chapter 5, a study is presented towards the use of mixed conducting membranes in the oxidative dehydrogenation of alkanes. Finally, Chapter 6 concludes with an evaluation of the main results obtained in this PhD thesis along with some recommendations for further research.

References

[1] J.B. Goodenough, Ceramic technology - oxide-ion conductors by design, Nature, 404 (2000) 821-823.

[2] J.A. Kilner, Ionic conductors feel the strain, Nat. Mater., 7 (2008) 838-839.

[3] M.F. Liu, D.H. Dong, R.R. Peng, J.F. Gao, J. Diwu, X.Q. Liu, G.Y. Meng, YSZ-based SOFC with modified electrode/electrolyte interfaces for operating at temperature lower than 650 °C, J. Power Sources, 180 (2008) 215-220.

[4] J.H. Joo, D.Y. Kim, G.M. Choi, Thick-film electrolyte-supported SOFC based on lanthanum-gallate electrolyte without using buffer layer, Electrochemical and Solid State Letters, 12 (2009) B65-B68.

[5] F. Abraham, J.C. Boivin, G. Mairesse, G. Nowogrocki, The Bimevox series - a new family of high performances oxide ion conductors, Solid State Ionics, 40-1 (1990) 934-937.

[6] M. Benammar, W.C. Maskell, An oxygen sensor-based upon a zirconia pump-gauge operated in a novel mode providing a linear output, Solid State Ionics, 70 (1994) 559-562.

[7] H.J.M. Bouwmeester, Dense ceramic membranes for methane conversion, Catal. Today, 82 (2003) 141-150.

[8] C.S. Chen, S.J. Feng, S. Ran, D.C. Zhu, W. Liu, H.J.M. Bouwmeester, Conversion of methane to syngas by a membrane-based oxidation-reforming process, Angew. Chem. Int. Ed., 42 (2003) 5196-5198.

[9] J.A. Kilner, C.K.M. Shaw, Mass transport in $La_2Ni_{1-x}Co_xO_{4+\delta}$ oxides with the K_2NiF_4 structure, Solid State Ionics, 154 (2002) 523-527.

[10] L.M. van der Haar, M.W. den Otter, M. Morskate, H.J.M. Bouwmeester, H. Verweij, Chemical diffusion and oxygen surface transfer of $La_{1-x}Sr_xCoO_{3-\delta}$ studied with electrical conductivity relaxation, J. Electrochem. Soc., 149 (2002) J41-J46.

[11] Z.P. Shao, S.M. Haile, A high-performance cathode for the next generation of solid-oxide fuel cells, Nature, 431 (2004) 170-173.

[12] M. Koyama, C.J. Wen, T. Masuyama, J. Otomo, H. Fukunaga, K. Yamada, K. Eguchi, H. Takahashi, The mechanism of porous $Sm_{0.5}Sr_{0.5}CoO_3$ cathodes used in solid oxide fuel

cells, J. Electrochem. Soc., 148 (2001) A795-A801.

[13] C.J. Zhu, X.M. Liu, C.S. Yi, D. Yan, W.H. Su, Electrochemical performance of $PrBaCo_2O_{5+\delta}$ layered perovskite as an intermediate-temperature solid oxide fuel cell cathode, J. Power Sources, 185 (2008) 193-196.

[14] J.M. Bassat, M. Petitjean, J. Fouletier, C. Lalanne, G. Caboche, F. Mauvy, J.C. Grenier, Oxygen isotopic exchange: a useful tool for characterizing oxygen conducting oxides, Appl. Catal., A, 289 (2005) 84-89.

[15] R.J. Chater, S. Carter, J.A. Kilner, B.C.H. Steele, Development of a novel SIMS technique for oxygen self-diffusion and surface exchange coefficient measurements in oxides of high diffusivity, Solid State Ionics, 53-6 (1992) 859-867.

[16] R.A. De Souza, J.A. Kilner, J.F. Walker, A SIMS study of oxygen tracer diffusion and surface exchange in $La_{0.8}Sr_{0.2}MnO_{3+\delta}$, Mater. Lett., 43 (2000) 43-52.

[17] J.A. Kilner, B.C.H. Steele, L. Ilkov, Oxygen self-diffusion studies using negative-ion secondary ion mass-spectrometry (SIMS), Solid State Ionics, 12 (1984) 89-97.

[18] D.S. Tannhauser, J.A. Kilner, B.C.H. Steele, The determination of the oxygen self-diffusion and gas solid exchange coefficients for stabilized zirconia by SIMS, Nuclear Instruments & Methods in Physics Research, 218 (1983) 504-508.

[19] R.A. De Souza, R.J. Chater, Oxygen exchange and diffusion measurements: the importance of extracting the correct initial and boundary conditions, Solid State Ionics, 176 (2005) 1915-1920.

[20] P. Fielitz, G. Borchardt, On the accurate measurement of oxygen self-diffusivities and surface exchange coefficients in oxides via SIMS depth profiling, Solid State Ionics, 144 (2001) 71-80.

[21] K. Klier, J. Novakova, P. Jiru, Exchange reactions of oxygen between oxygen molecules and solid oxides, J. Catal., 2 (1963) 479-484.

[22] P.J. Gellings, H.J.M. Bouwmeester, Ion and mixed conducting oxides as catalysts, Catal. Today, 12 (1992) 1-105.

[23] B.A. Boukamp, H.J.M. Bouwmeester, H. Verweij, A.J. Burggraaf, Surface oxygen exchange kinetics in oxide-ion conducting solids, Mat. Res. Soc. Symp. Proc., 293 (1993) 361-366.

[24] E. Bucher, A. Egger, P. Ried, W. Sitte, P. Holtappels, Oxygen nonstoichiometry and exchange kinetics of $Ba_{0.5}Sr_{0.5}Co_{0.8}Fe_{0.2}O_{3-\delta}$, Solid State Ionics, 179 (2008) 1032-1035.

[25] G. Kim, S. Wang, A.J. Jacobson, L. Reimus, P. Brodersen, C.A. Mims, Rapid oxygen ion diffusion and surface exchange kinetics in $PrBaCo_2O_{5+x}$ with a perovskite related structure and ordered A cations, J. Mater. Chem., 17 (2007) 2500-2505.

[26] J.A. Lane, J.A. Kilner, Measuring oxygen diffusion and oxygen surface exchange by conductivity relaxation, Solid State Ionics, 136 (2000) 997-1001.

[27] B. Ma, U. Balachandran, J.H. Park, C.U. Segre, Determination of chemical diffusion coefficient of $SrFeCo_{0.5}O_x$ by the conductivity relaxation method, Solid State Ionics, 83 (1996) 65-71.

[28] J.E. ten Elshof, M.H.R. Lankhorst, H.J.M. Bouwmeester, Oxygen exchange and diffusion coefficients of strontium-doped lanthanum ferrites by electrical conductivity relaxation, J. Electrochem. Soc., 144 (1997) 1060-1067.

[29] S.L. Shannon, J.G. Goodwin, Characterization of catalytic surfaces by isotopic-transient kinetics during steady-state reaction, Chem. Rev., 95 (1995) 677-695.

[30] C.C. Kan, H.H. Kan, F.M. van Assche, E.N. Armstrong, E.D. Wachsman, Investigating oxygen surface exchange kinetics of $La_{0.8}Sr_{0.2}MnO_{3-\delta}$ and $La_{0.6}Sr_{0.4}Co_{0.2}Fe_{0.8}O_{3-\delta}$ using an isotopic tracer, J. Electrochem. Soc., 155 (2008) B985-B993.

Chapter 2

Pulse-response ^{18}O-^{16}O isotopic exchange - A novel method for rapid determination of the rate of oxygen surface exchange on oxide ion conductors

Parts of this chapter has been published in

H.J. M. Bouwmeester, C. Song, J.J. Zhu, J.Yi, M. van Sint-Annaland, and B.A. Boukamp
Phys. Chem. Chem. Phys., 2009, 11, 9640–9643.

Abstract

A novel pulse ^{18}O-^{16}O isotopic exchange (PIE) technique for measurement of the rate of oxygen surface exchange of oxide ion conductors is presented. The technique employs a continuous flow packed-bed micro-reactor loaded with the oxide powder. The isothermal response to an ^{18}O-enriched pulse passing through the reactor, thereby maintaining chemical equilibrium, is measured by on-line mass spectrometry. Evaluation of the apparent exchange rate follows from the uptake of ^{18}O by the oxide at given reactor residence time and surface area available for exchange. The developed PIE technique is rapid, simple and highly suitable for screening and systematic studies. The technique is further amenable to *in situ* analysis of the effect of gas phase impurities, e.g. CO_2 and H_2O, on oxygen surface exchange. No rapid heating/quenching steps are required to facilitate ^{18}O tracer anneal or analysis, as in other commonly used techniques based upon oxygen isotopic exchange. Moreover, the relative distribution of the oxygen isotopomers $^{18}O_2$, $^{16}O^{18}O$, and $^{16}O_2$ in the effluent pulse provides insight into the mechanism of the oxygen exchange reaction. The PIE technique has been demonstrated by measuring the exchange rate of selected oxides with enhanced oxide ionic conductivity in the range 350 - 900 °C. Analysis of the experimental data in terms of a model with two consecutive, lumped steps for the isotopic exchange reaction shows that for mixed conductors $Ba_{0.5}Sr_{0.5}Co_{0.8}Fe_{0.2}O_{3-\delta}$ (BSCF) and $La_2NiO_{4+\delta}$ the reaction is limited by the apparent rate of dissociative adsorption of O_2 molecules at the oxide surface. The exchange rate found for BSCF is among the highest values reported in literature. For yttria-stabilized zirconia (YSZ) a change-over takes place, from rate-limitations by oxygen incorporation below ~800 °C to rate-limitations by O_2 dissociative adsorption above this temperature. Good agreement is obtained with exchange rates reported for these materials in literature.

2.1 Introduction

The increasing energy demand and cost, in conjunction with the growing public awareness of the need for energy production with minimal environmental impact, have generated significant research endeavors over the past two decades towards development of oxygen transport membranes and solid oxide fuel cells (SOFCs) [1-7]. Both devices incorporate solid oxide electrolytes and/or oxides with highly mobile oxide ions and electronic charge carriers, so-called mixed conductors. Their performance strongly relies on fast oxygen exchange (see Fig. 2.1) at relevant gas/solid interfaces. Since the rate may govern the overall transport kinetics, detailed knowledge of the oxygen surface exchange reaction is a pre-requisite for further development of these devices.

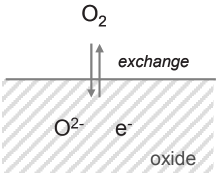

Fig. 2.1 Reversible oxygen exchange between the gas phase and the oxide.

A variety of methods has been used to probe the surface exchange kinetics on oxide surfaces, such as (*i*) electrical conductivity relaxation (ECR) [8-10], (*ii*) oxygen permeation [11], (*iii*) ^{18}O-^{16}O isotopic exchange [12-19] and (*iv*) electrochemical impedance spectroscopy (EIS) [20, 21]. Especially, methods based upon isotope exchange are considered useful for obtaining information on surface oxygen exchange. There are, in essence, two different approaches, which are based upon ^{18}O isotope analysis of either the oxide bulk or the gas phase. In the former, referred to as isotope exchange depth-profiling (IEDP), a dense sample is subjected to an ^{18}O-^{16}O exchange anneal, followed by *ex-situ* depth profiling of the ^{18}O tracer diffusion profile by ion beam analysis, such as secondary ion mass spectrometry (SIMS) [19] or nuclear reaction analysis (NRA) [22]. The experiments enable simultaneous determination of the oxygen diffusion coefficient (D^*) and surface exchange coefficient (k^*), which are obtained by fitting the concentration depth profile to the appropriate solution of the diffusion equation. In the second technique, referred to as isotopic exchange gas-phase equilibration (IEGE), the equilibration of the oxygen isotope fractions in the gas phase during the ^{18}O-^{16}O exchange anneal is *in-situ* monitored as a function of time using mass spectrometry [20, 23, 24]. Both techniques have their intrinsic advantages and disadvantages. The advantage of the gas phase technique over the depth-profiling technique is that besides the exchange rate also information is obtained on the mechanism of the surface exchange reaction. The latter may be evaluated from the time-dependence of the concentration of oxygen isotopomers, $^{18}O_2$, $^{16}O^{18}O$, and $^{16}O_2$, formed by isotopic scrambling and recombination of oxygen adatoms at the oxide surface. Both techniques, however, involve a number of rapid heating, pre- and/or diffusion annealing, and quenching steps. Not only is this time consuming, but also one must exercise great care in order to avoid introduction of artefacts and errors into the assessment of the kinetic parameters [25, 26].

In this chapter, we introduce a novel technique, referred to as pulse-response ^{18}O-^{16}O isotopic exchange (PIE). The technique allows rapid assessment of the oxygen surface exchange rates of solid oxide ion conductors at chosen conditions of temperature and oxygen partial pressure. In this work, the PIE technique is demonstrated by measuring the oxygen surface exchange rate of yttria-stabilized zirconia (YSZ), $Ba_{0.5}Sr_{0.5}Co_{0.8}Fe_{0.2}O_{3-\delta}$ (BSCF) and $La_2NiO_{4+\delta}$. YSZ is widely used as oxide solid electrolyte, while the mixed ionic-electronic conductors BSCF and $La_2NiO_{4+\delta}$ have potential for application either as cathode material for the intermediate-temperature SOFC or as oxygen transport membrane [4, 27]. Different from IEDP and IEGE, no rapid heating and/or quenching steps are required in application of the PIE technique. Since the technique relies on gas phase analysis of the concentrations of $^{18}O_2$, $^{16}O^{18}O$, and $^{16}O_2$, also kinetic information of the oxygen surface exchange reaction can be extracted from the experimental data.

2.2 Theory

2.2.1 Principle of pulse isotopic exchange

The pulse isotopic exchange (PIE) technique developed in this work employs a packed-bed micro-reactor loaded with the oxide powder. After equilibration of the oxide at chosen oxygen partial pressure and temperature, the response to an ^{18}O-enriched pulse fed through the reactor operating under continuous flow conditions is measured. The principle of the measurement is shown schematically in Fig. 2.2.

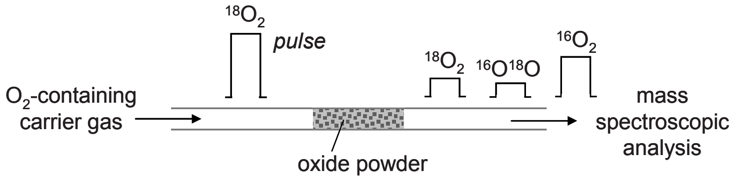

Fig. 2.2 Principle scheme of the pulse ^{18}O-^{16}O isotope exchange technique.

The overall surface exchange rate is calculated from the mean residence time, the total surface area of the oxide powder available for exchange, and the uptake of ^{18}O by the oxide. The latter is evaluated from the known ^{18}O tracer concentration in the injected pulse, and that in the effluent pulse measured by on-line mass spectrometry at the exit of the reactor. After passage of the pulse, the conditions may be changed and the oxide sample equilibrated for another pulse experiment. The PIE technique enables fast acquisition of the surface exchange rate of the oxide under investigation as a function of environmental parameters, e.g., temperature and oxygen partial pressure.

PIE differs from the technique known as SSITKA (steady-state isotopic transient kinetic analysis technique) frequently used in studies of heterogeneous catalysis [28].

SSITKA involves isothermal switching the isotopic composition of the feed stream flowing through the packed bed reactor. For evaluation of the oxygen exchange rate, numerical modelling is required to analyse the kinetic data as a function of time-on-stream [29]. The boundary conditions associated with PIE make evaluation of the surface exchange rate rather simple and straight forward. The mode of gas transport in PIE further differs from that in conventional pulse and TAP (temporal analysis of products) micro-reactors where either an inert gas, such as helium or nitrogen, is used as carrier gas, or the exit of the reactor is exposed to high vacuum conditions [30].

The mathematical analysis of the data of PIE is rather simple. Consider a differential volume element traversing through the reactor. Under the assumption of *(i)* ideal plug flow behaviour, *(ii)* homogeneous packing of the oxide in the reactor, and *(iii)* relative to surface exchange, fast lattice diffusion of oxygen, *i.e.*, a large diffusion length of ^{18}O in the (non-porous) oxide, mass balance analysis yields the first order linear differential equation

$$n_\mathrm{g}\frac{\partial f_\mathrm{g}^{18}}{\partial t} = -\Re_0 S\left(f_\mathrm{g}^{18} - f_\mathrm{o}^{18}\right) \tag{2.1}$$

where $\Re_0$ [mol O.m^{-2}.s^{-1}] is the surface exchange rate, n_g the number of oxygen atoms in the gas phase (mobile phase) contained in a single volume element (which is twice the number of O_2 molecules), and S the associated surface area of the oxide (stationary phase) to which the gas phase is exposed. f_g^{18} and f_o^{18} are the ^{18}O isotope fractions in the gas phase and oxide, respectively. It is noted that f_g^{18} is calculated from the molar fractions of ^{16}O^{18}O and ^{18}O$_2$ in the gas phase: $f_\mathrm{g}^{18} = f_\mathrm{g}^{36} + 0.5 f_\mathrm{g}^{34}$. Eq. 2.1 can be rewritten as,

$$n_\mathrm{r}\frac{\partial f_\mathrm{g}^{18}}{\partial t} = -\Re_0 S_\mathrm{r}\left(f_\mathrm{g}^{18} - f_\mathrm{o}^{18}\right) \tag{2.2}$$

in which n_r and S_r represent the number of gas phase oxygen atoms and surface area of the oxide, respectively, for the entire packed bed reactor. The ^{18}O concentration in the gas phase is much lower than that in the oxide. In the absence of significant accumulation of ^{18}O in the oxide or at the oxide surface, *i.e.* assuming $f_{\mathrm{o}}^{18} \approx 0$, it follows

$$n_{\mathrm{r}} \frac{\partial f_{\mathrm{g}}^{18}}{\partial t} = -\Re_0 S_{\mathrm{r}} f_{\mathrm{g}}^{18} \tag{2.3}$$

Splitting of the variables and integration over a time yields

$$f_{\mathrm{g}}^{18}(t) = f_{\mathrm{g,i}}^{18} \cdot \exp\left(-\frac{\Re_0 S_{\mathrm{r}} t}{n_{\mathrm{r}}}\right) \tag{2.4}$$

which for, $t = \tau_{\mathrm{r}}$, where τ_{r} is the residence time of the reactor, can be re-written as

$$\Re_0 = -\frac{n_{\mathrm{r}}}{\tau_{\mathrm{r}} S_{\mathrm{r}}} \ln\left(\frac{f_{\mathrm{g,o}}^{18}}{f_{\mathrm{g,i}}^{18}}\right) \tag{2.5}$$

In Eqs. 2.4 and 2.5, $f_{\mathrm{g,i}}^{18}$ and $f_{\mathrm{g,o}}^{18}$ denote the ^{18}O isotope fractions in the gas phase at the inlet and outlet of the reactor, respectively. The validity of these equations extends to any finite number of ^{18}O atoms in the pulse volume as long as the boundary conditions adopted during their derivation are satisfied. The residence time (or space time) of the reactor can be calculated from

$$\tau_{\mathrm{r}} = \frac{V_{\mathrm{r}} \varepsilon}{F} \tag{2.6}$$

where V_{r} is the total volume of the packed bed reactor, ε the bed void fraction, and *F* the volumetric flow rate of the gas at chosen temperature. With the aid of Eq. 2.6, Eq. 2.5 can be written in more practical forms, as

$$\begin{aligned} \Re_0 &= -\frac{c_g F}{S_{\mathrm{r}}} \ln\left(\frac{f_{\mathrm{g,o}}^{18}}{f_{\mathrm{g,i}}^{18}}\right) \\ &= -\frac{F_{\mathrm{m}}}{S_{\mathrm{r}}} \ln\left(\frac{f_{\mathrm{g,o}}^{18}}{f_{\mathrm{g,i}}^{18}}\right) \end{aligned} \tag{2.7}$$

where $c_g = n_r / \varepsilon V_r$ is the oxygen concentration in the gas phase , and $F_m = Fc_g$ it is the molar flow rate, or using the ideal gas law, in the form $c_g = 2p\mathrm{O}_2 / RT$, as

$$\Re_0 = -\frac{2p\mathrm{O}_2}{RS_r} \cdot \frac{F}{T} \ln\left(\frac{f_{g,o}^{18}}{f_{g,i}^{18}}\right) \tag{2.8}$$

The factor 2 in this equation arises from the fact that the oxygen atoms in the gas phase are present as O_2 molecules. The flow rate F at temperature T can be converted to the audit flow rate F_0 at temperature T_0, usually room temperature, using $F = (T / T_0)F_0$. Note that in both Eqs. 2.7 and 2.8 the void fraction ε cancels out.

On passing through the oxide bed, the gas phase is considered to retain thermodynamic equilibrium with the oxide. The ^{18}O-containing gas phase pulse passes through a 'sea of ^{16}O' captured by the oxide powder bed, ensuring, along with fast lattice diffusion of oxygen, that ^{16}O is returned to the gas phase upon every successful exchange event. In accord with Eq. 2.4, the main parameters thus governing surface exchange are the kinetic parameter $\Re_0$, which expresses the balanced exchange rate under equilibrium conditions, the available surface area S_r (hence, the amount of oxide powder or length of the packed bed), and the residence time of the reactor, τ_r. Reactor design and experimental conditions are chosen such that channeling, interphase and intraparticle diffusion are considered to be of minor importance and therefore can be neglected. This is further elaborated in the *Supplementary information* of this chapter.

2.2.2 Two-step oxygen exchange mechanism

The surface exchange rate, $\Re_0$, extracted from measurement merely is a lumped parameter, and may involve a sequence of possible reaction steps, each of which may be rate determining. Steps commonly considered include adsorption, dissociation, charge transfer, incorporation of oxygen into the oxide lattice, with possible intermediates like O_2^-, O_2^{2-} and O^-, of which only the superoxide ion, O_2^-, is known to be stable with respect to gaseous O_2 [31].The altered distribution of isotopomers $^{18}O_2$, $^{16}O^{18}O$ and $^{16}O_2$ in the gas phase pulse (see Fig. 2.3), as occurs during passage through the reactor due to isotopic exchange/scrambling reactions at the oxide surface, holds important kinetic information about the exchange mechanism.

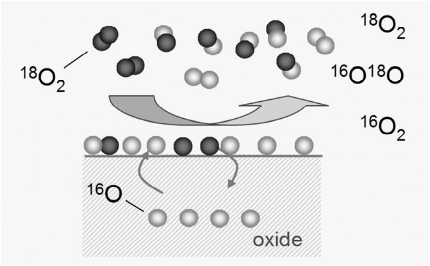

Fig. 2.3 Isotopic scrambling at the oxide surface is altering the distribution of oxygen isotopomers ($^{16}O_2$, $^{16}O^{18}O$, $^{18}O_2$) in the gas phase.

The reversible oxygen exchange reaction may proceed via a consecutive two-step mechanism, as proposed earlier by Boukamp *et al.* [20]

Step 1 $$O_2^* \underset{\bar{\Re}_a}{\overset{\Re_a}{\rightleftarrows}} 2O_{ad}^*$$

Step 2 $$O_{ad}^* \underset{\bar{\Re}_i}{\overset{\Re_i}{\rightleftarrows}} O_{lattice}$$

Each of the two steps, however, may still represent a grouping of specific elementary steps. Relevant for the interpretation of experimental data of isotopic exchange is that isotopic randomization is assumed to take place only after the dissociative adsorption step of oxygen at the surface (1st step). During its residence time at the surface, the oxygen adatom may combine either with another adatom and return to the gas phase as an O_2 molecule, or become exchanged with lattice oxygen (2nd step) before returning to the gas phase. Assuming low coverage of oxygen adatoms on the surface, it is easily shown that the overall rate of surface exchange can be expressed as

$$\Re_0 = \frac{\Re_a \Re_i}{\Re_a + \Re_i} \tag{2.9}$$

where $\Re_a$ is the rate of homolytic dissociative adsorption of O_2 molecules at the oxide surface, and $\Re_i$ that of subsequent incorporation of the formed oxygen adatoms into the oxide lattice. In deriving Eq. 2.9, the occurrence of alternative pathways for oxygen exchange has been excluded, such as (*i*) the mutual exchange of oxygen between O_2 molecules in the gas phase, and (*ii*) possible swapping out of one of the oxygen atoms of the O_2 molecule for another oxygen during hypothetical formation of a three-atom complex between a gas phase O_2 molecule and an O adatom, or any other multi-atom complex between O_2 molecules and adsorbed species.

In deriving the distribution of oxygen isotopomers $^{18}O_2$, $^{16}O^{18}O$ and $^{16}O_2$ in the effluent gas phase pulse, the more general treatment given earlier by Den Otter [14] is followed. Recognizing that

$$p = \frac{\Re_i}{\Re_a + \Re_i} \tag{2.10}$$

represents the probability for successful exchange between oxygen residing on the surface and lattice oxygen, the time dependence of the gas phase fraction for $^{18}O_2$ can be expressed by the differential equation

$$n_{\mathrm{r}}\frac{\partial f_{\mathrm{g}}^{36}}{\partial t}=S_{\mathrm{r}}\Re_{\mathrm{a}}\left(-f_{\mathrm{g}}^{36}+\left(f_{\mathrm{g}}^{18}\left(1-p\right)\right)^{2}\right) \tag{2.11}$$

Substitution of Eq. 2.4 in Eq. 2.11, followed by integration over the time of residence in the reactor, τ_{r}, yields

$$\begin{aligned}f_{\mathrm{g,o}}^{36}=&\frac{\left(1-p\right)^{2}}{1-2p}\left(f_{\mathrm{g,i}}^{18}\right)^{2}\exp\left(-\frac{2\Re_{0}S_{\mathrm{r}}\tau_{\mathrm{r}}}{n_{\mathrm{r}}}\right)\\&+f_{\mathrm{g,i}}^{36}\exp\left(-\frac{\Re_{0}S_{\mathrm{r}}\tau_{\mathrm{r}}}{pn_{\mathrm{r}}}\right)-\frac{\left(1-p\right)^{2}}{1-2p}\left(f_{\mathrm{g,i}}^{18}\right)^{2}\exp\left(-\frac{\Re_{0}S_{\mathrm{r}}\tau_{\mathrm{r}}}{pn_{\mathrm{r}}}\right)\end{aligned} \tag{2.12}$$

where $f_{\mathrm{g,i}}^{36}$ and $f_{\mathrm{g,o}}^{36}$ denote the $^{18}O_2$ fractions in the gas phase pulse at the inlet and outlet of the reactor, respectively. The corresponding $^{16}O^{18}O$ and $^{16}O_2$ fractions can be calculated from the conservation equations

$$f_{\mathrm{g}}^{34}=2\left(f_{\mathrm{g}}^{18}-f_{\mathrm{g}}^{36}\right) \tag{2.13}$$

$$f_{\mathrm{g}}^{32}=1-f_{\mathrm{g}}^{34}-f_{\mathrm{g}}^{36} \tag{2.14}$$

which are valid at all coordinates in the reactor, ignoring axial dispersion in the plug flow reactor. In the theory developed by Klier *et al.* [16, 32], and independently by Boreskov and Muzykantov [12, 33], oxygen isotopic exchange is described to occur via three parallel one-step mechanisms: the O_2 molecule may exchange either one or both atoms with lattice oxygen (hetero exchange), at rates R_1 and R_2, respectively, or, without the involvement of lattice oxygen, i.e. only with oxygen from the gas phase (homo exchange), at a rate R_0. As discussed previously [14, 34], if no other pathways for oxygen exchange are vivid, these three rates are constrained in the above 2-step model as: $R_1=2\sqrt{R_0R_2}$.

2.3 Experimental

$(Y_2O_3)_{0.08}$-$(ZrO_2)_{0.92}$ (YSZ) powder (TOSOH, Japan, purity 99.9%) was calcined in air at 900 °C for 10 h. BSCF powder was prepared by solvent evaporation, and subsequent thermal decomposition of the precursor complexes, of an aqueous solution of metal nitrates in appropriate stoichiometry and to which ethylenediaminetetraacetic (EDTA) was added as complexing agent. The powder obtained was calcined in air at 800 °C for 24 h, and subsequently ball-milled in ethanol for 5 h. The milled powder was pressed into a disk *via* cold isostatic pressing at 4000 bar, and then sintered in air at 1100 °C for 10 h. The sintered disk was crushed to powder. The fraction of the powder passing a 120 mesh metal sieve was calcined in air at 950 °C for 10 h, and sieved again to remove possibly formed agglomerates. Heating and cooling rates in all cases were 3 °C min^{-1}. $La_2NiO_{4+\delta}$ powder was prepared similarly to BSCF, except that (*i*) the raw powder was calcined in air at 1000 °C for 10 h, (*ii*) the disk was sintered in air at 1370 °C for 10 h, and (*iii*) the crushed powder was calcined in air at 1100 °C for 10 h. The powders were characterized by X-ray powder diffraction (Philips PANalytical PW1830), Brunauer-Emmet-Teller BET surface area (Micromeritics ASAP 2020M), and particle size (Mastersizer 2000, Malvern) measurements. The particle sizes were in the range 2-5 μm, with BET surfaces of 10.12, 0.210 and 0.156 m^2g^{-1} for YSZ, BSCF and $La_2NiO_{4+\delta}$, respectively. X-ray diffraction confirmed that in all cases the desired structures were formed. Within the detection limit of XRD, no evidence was found for second phase formation or presence of other phase impurities.

PIE measurements were performed in the temperature range 350 – 900 °C, with 25 or 50 °C intervals, at $pO_2 = 0.21$ atm, using a continuous flow packed-bed micro-reactor. The oxide powder was loaded between two quartz wool plugs in the center of the quartz tubular micro-reactor, having an inner diameter of 2 mm. The packed-bed length was typically in the range 10-20 mm. Two quartz rods with diameter ~1 mm were used to minimize the free volume of the reactor. $^{16}O_2$ balanced with He to a pO_2 of 0.21 atm was used as carrier gas. The flow rate was 50 NTP ml min^{-1}, if not specified otherwise. Prior to measurements, the packed-bed micro-reactor was pre-treated at 850 °C for 2 h under a continuous flow of the carrier gas in order to remove possibly adsorbed water and CO_2, and subsequently cooled to room temperature, using heating/cooling rates of 3 °C min^{-1}. The response to an $^{18}O_2/N_2$ gas phase pulse (500 µl), with similar pO_2 as the carrier gas, passing through the reactor, was analyzed by online mass spectrometry (Omni Star^{TM} GSD 301 Pfeiffer-Vacuum). Oxygen isotope gas (> 99 atom% $^{18}O_2$) was purchased from ISOTEC, Sigma-Aldrich. Nitrogen used as diluent for $^{18}O_2$ was also used for internal calibration of the mass spectrometer. A six-port valve with sample loop was used for injection of the pulse into the main carrier gas flow. The reactor was equilibrated for 15 min under continuous flow of the carrier gas prior to pulse injection. Measurements were conducted as a function of temperature, from room temperature onwards, by determining the $^{18}O_2$ and $^{16}O^{18}O$ concentrations in the effluent pulse. The integrated peak area of the oxygen isotope fraction of $^{16}O^{18}O$ was corrected for tailing, if present, by linear interpolation of the background. Average values of three pulse experiments at given temperature were used for calculations of the exchange rates. The mean residence time of the reactor varied between 5 to 40 ms, depending on the volumetric flow rate of the carrier gas at the temperature of the measurement, and the packed bed length. Additional measurements were carried out to check the presence of interphase (external) concentration gradients by varying the volumetric flow rate, and, in case of YSZ, the packed bed length in the range 25-100 NTP ml min^{-1} and 6-27 mm, respectively. Experimental data obtained from heating and cooling runs agreed within experimental error. Within the range of temperatures studied, blank experiments carried out at a carrier gas flow rate of 50 NTP ml min^{-1} revealed no significant exchange activity of the empty quartz micro-reactor (See *Supplementary information*).

2.4 Results and discussion

2.4.1 PIE measurements

Mass spectroscopic data for $^{18}O_2$ and $^{16}O^{18}O$ obtained from PIE measurements on YSZ, BSCF and $La_2NiO_{4+\delta}$ as a function of temperature are shown in Fig. 2.4. Corresponding isotope fractions $f_{g,o}^{36}$ and $f_{g,o}^{34}$ calculated from the integrated peak areas are shown in Fig. 2.5. $f_{g,o}^{32}$ was calculated using Eq. 2.14. Under the conditions of the experiments, the uptake of ^{18}O by the oxide becomes pronounced at elevated temperature. The corresponding onset temperatures are, however, different for the three compositions studied. This is, besides comparatively small differences in available surface area for exchange, mainly accounted for by the different specific activities for exchange exhibited by the materials. As seen from both figures, above the onset temperature of surface

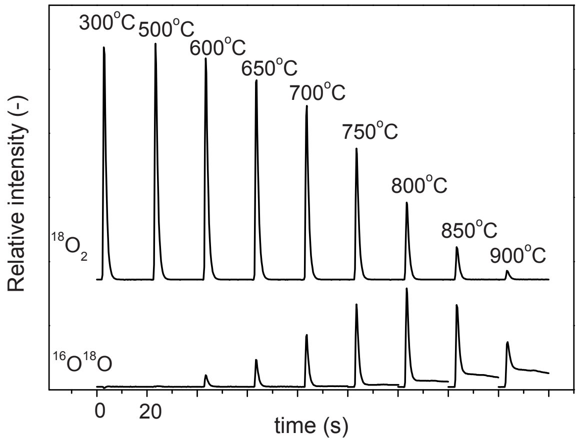

Fig. 2.4 (a)

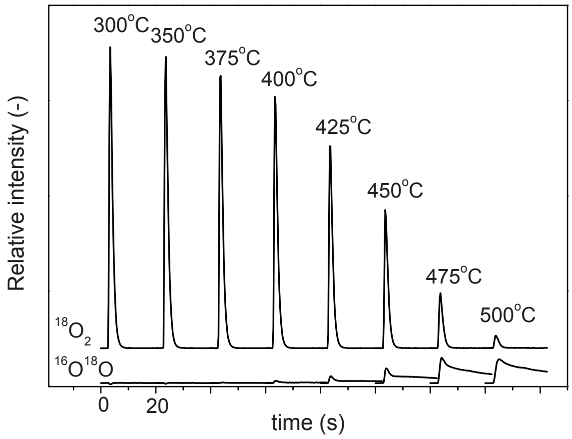

Fig. 2.4 (b)

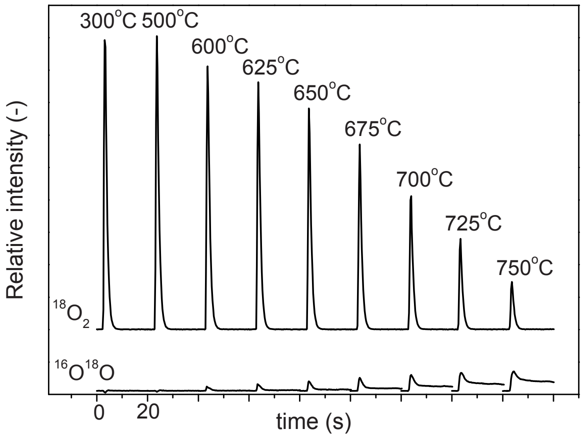

Fig. 2.4 (c)

Fig. 2.4 Mass spectroscopic peaks for $^{18}O_2$ (m/z = 36) and $^{16}O^{18}O$ (m/z = 34) from PIE measurements as a function of temperature, for (a) YSZ, (b) BSCF, and (c) $La_2NiO_{4+\delta}$. Peaks obtained at different temperatures are shifted with respect to each other for reasons of clarity. Note that peak tailing is observed at the highest temperatures, and is only manifest for the $^{16}O^{18}O$ peak. This is further discussed in the text.

exchange, the $^{18}O_2$ signal and, hence, the corresponding isotope fraction, $f_{\mathrm{g,o}}^{36}$, are found to decrease gradually with increasing temperature. This brings about associated changes in the isotope fractions of $^{16}O_2$ ($f_{\mathrm{g,o}}^{32}$) and $^{16}O^{18}O$ ($f_{\mathrm{g,o}}^{34}$) with increasing temperature. The latter behavior, found to be different for the three compositions, can be regarded as a *fingerprint* for the mechanism of surface oxygen exchange, i.e., the rate of oxygen dissociative adsorption relative to that of oxygen incorporation, as discussed in more detail below.

As seen from Fig. 2.4, tailing of the $^{16}O^{18}O$ peak occurs at the highest temperature in the experiments. This observation is closely linked to the operating principle of the PIE technique, which essentially exploits the temporary hold-up of the ^{18}O isotope by (partial) incorporation into the oxide. The solid oxide forms a large reservoir of ^{16}O oxygen atoms. Hence, every successful exchange event implies a single transfer of ^{16}O to the gas phase, either in the form of $^{16}O^{18}O$ or $^{16}O_2$, depending on the relative rates of oxygen dissociative adsorption and oxygen incorporation, in conjunction with the extent of depletion of ^{18}O from the gas phase. Once the pulse has passed through the reactor, the (remaining) exchanged ^{18}O will be released from the oxide, with an approximate release time constant $\tau_{\mathrm{release}} = m_{\mathrm{r}} / \Re_0 S_{\mathrm{r}}$, where m_{r} is the total number of oxide lattice oxygen in the reactor volume. The latter time constant should be compared with that of ^{18}O uptake during passage of the pulse, $\tau_{\mathrm{uptake}} = n_{\mathrm{r}} / \Re_0 S_{\mathrm{r}}$, where n_{r} is the total number of gas phase oxygen atoms in the reactor volume (*c.f.* Eq. 2.4). Since $m_{\mathrm{r}} >> n_{\mathrm{r}}$, it is obvious that $\tau_{\mathrm{release}} >> \tau_{\mathrm{uptake}}$. At high temperatures, where oxygen exchange is comparatively fast, τ_{release} approaching the time scale of the pulse experiment, the release of ^{18}O from the oxide may induce peak tailing. Since the concentration of ^{18}O atoms in the oxide is small, their recombination to O_2 molecules occurs predominantly with excess ^{16}O. Significant peak tailing therefore might be manifest only for the $^{16}O^{18}O$ peak. Since a master equation for peak tailing was lacking, integrated $^{16}O^{18}O$ peak areas were corrected for tailing, if present, by a simple linear interpolation of the background. For calculation of the ^{18}O uptake by the oxide and, hence, the effective surface exchange rate, the peak tailing correction of the $^{16}O^{18}O$ peak at high temperature was usually found to be marginal relative to the concomitant decrease of the $^{18}O_2$ peak as a result of oxygen exchange.

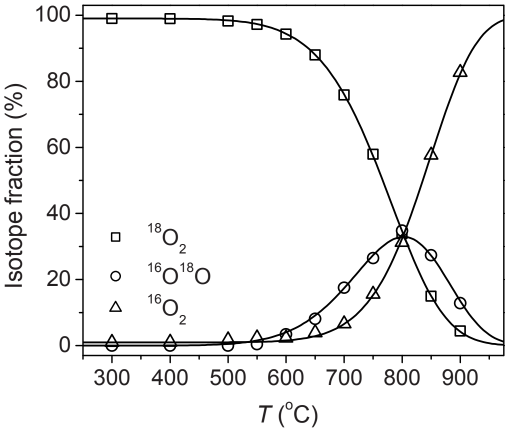

Fig. 2.5 (a)

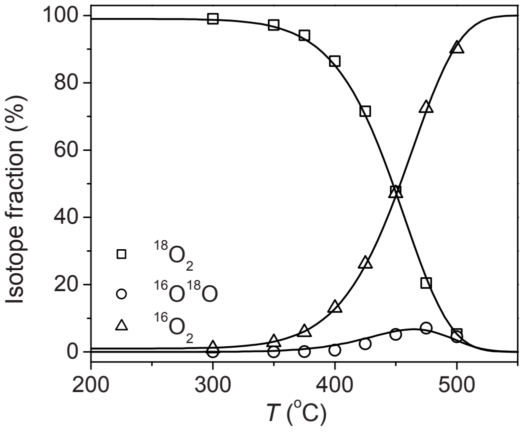

Fig. 2.5 (b)

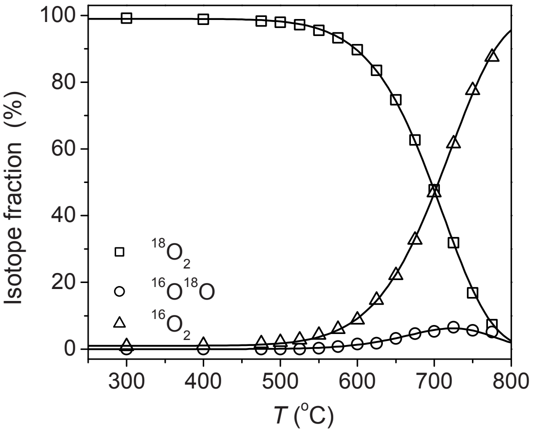

Fig. 2.5 (c)

Fig. 2.5 Oxygen isotope fractions ($^{18}O_2$, $^{16}O^{18}O$ and $^{16}O_2$) as a function of temperature from PIE measurements on (a) YSZ , (b) BSCF, and (c) $La_2NiO_{4+\delta}$. Full lines are from model calculations, assuming constant activation energies for the rates of O_2 dissociative adsorption ($\Re_a$) and incorporation of oxygen adatoms into the oxide lattice ($\Re_i$). Maximum error bars are smaller than the size of the symbols.

2.4.2 Oxygen surface exchange rate

Fig. 2.6 shows Arrhenius plots of the overall surface exchange rate, $\Re_0$, for the three compositions studied, calculated using Eq. 2.5. The results confirm that BSCF exhibits comparatively high exchange rates, which values are among the highest reported in literature [35]. The exchange rate of BSCF, at 500 °C, is found to be almost 4 orders of magnitude higher than that of YSZ. Activation energies for $\Re_0$ extracted from the Arrhenius plots are listed in Table 2.1.

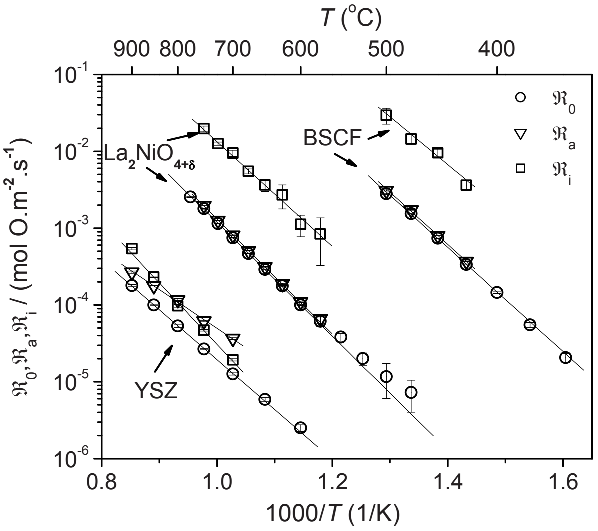

Fig. 2.6 Temperature dependence of the rate of oxygen exchange ($\Re_0$), oxygen dissociative adsorption ($\Re_a$), and oxygen incorporation ($\Re_i$) for YSZ, BSCF, and $La_2NiO_{4+\delta}$. The error bars show the maximum errors.

Table 2.1 Apparent activation energies of $\Re_0$, $\Re_a$ and $\Re_i$ from PIE measurements

Oxide	$\Re_0$ (kJ mol^{-1})	$\Re_a$ (kJ mol^{-1})	$\Re_i$ (kJ mol^{-1})
YSZ	121.4 ± 1.3	95.6 ± 2.9	156.3 ± 6.0
BSCF	132.1 ± 1.2	128.1 ± 3.5	120.5 ± 12.0
$La_2NiO_{4+\delta}$	130.3 ± 2.1	140.4 ± 1.2	132.0 ± 5.2

To prevent intraparticle concentration gradients, possibly developing in micro- or mesopores of the oxide, the exchange measurements were conducted on powders obtained by crushing sintered ceramics. To check for the presence of interphase (external) concentration gradients, additional measurements were conducted at 25 and 100 NTP ml min^{-1}, besides at 50 NTP ml min^{-1}. In addition, in the case of YSZ, the length of the packed bed was varied in the range 6.3-26.4 mm. Corresponding results are presented in the *Supplementary information*. In neither experiment evidence could be found for interphase concentration gradients. The exchange rates obtained from the different experiments carried out for each composition are found to agree within experimental error. It should be noted that the apparent activation energies as listed in Table 2.1 also do not suggest the presence of significant interphase concentration gradients. Only if the apparent activation energy is less than 20 kJ mol^{-1}, interphase diffusion limitations might be suspected [36].

For each of the compositions studied, the exchange rates are found to be in good agreement with data from previous studies, measured using either electrical conductivity relaxation and/or the isotopic exchange depth-profiling (IEDP) technique [35, 37-40].

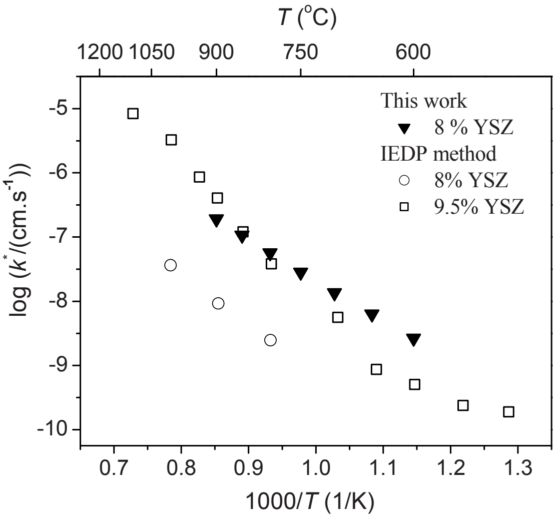

Fig. 2.7 Comparison of k^* of YSZ measured by this work ($pO_2 = 0.21$ atm) and by IEDP method ($pO_2 = 1$ atm): 8% YSZ in Ref. 37 and 9.5% YSZ in Ref. 40.

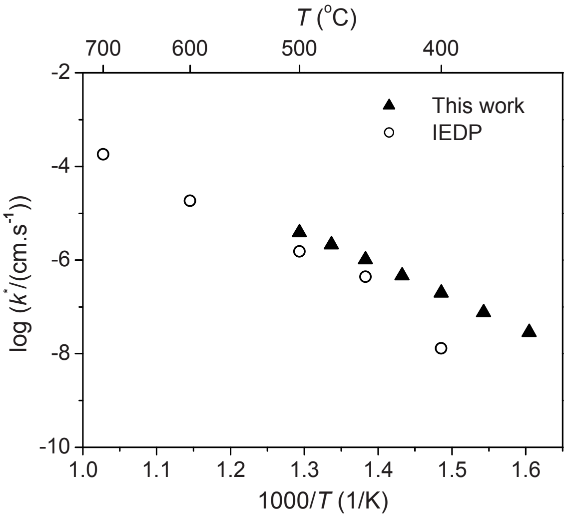

Fig. 2.8 Comparison of k^* of BSCF measured by this work ($pO_2 = 0.21$ atm) and by IEDP method ($pO_2 = 0.5$ atm) in Ref. 35.

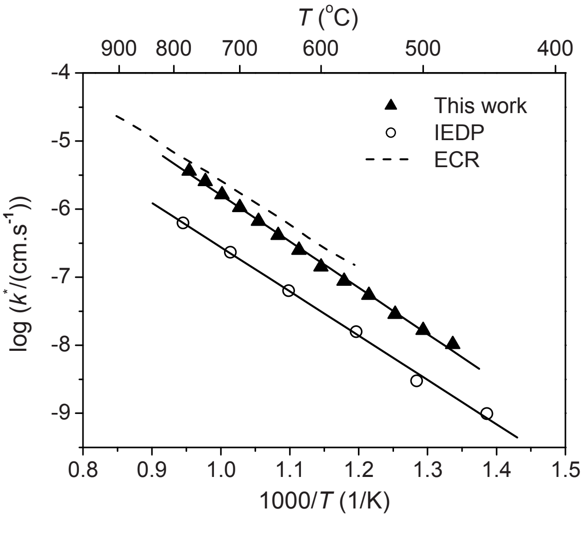

Fig. 2.9 Comparison of k^* of $La_2NiO_{4+\delta}$ measured by this work and by IEDP in Ref. 38 and ECR methods in Ref. 39, all at $pO_2 = 0.21$ atm.

Data obtained from different studies are compared in Figs. 2.7, 2.8 and 2.9 for YSZ, BSCF and $La_2NiO_{4+\delta}$, respectively. To enable comparison, the surface exchange rate, $\Re_0$ [mol O m^{-2} s^{-1}], was recalculated to the surface exchange coefficient, k^* [m s^{-1}], using $k^* = \Re_0 / c_o$, where c_o is the concentration of oxygen in the oxide. Discrepancies between the values obtained in different studies for each of the compositions can be, at least partly, accounted for by differences in the experimental conditions, pre-annealing procedures, and morphology of the samples (e.g. single crystal versus polycrystalline samples).

2.4.3 Two-step oxygen exchange mechanism

As discussed in Section 2.2, the observed distribution of $^{18}O_2$, $^{16}O^{18}O$ and $^{16}O_2$ isotopomers in the effluent pulse allows one to deconvolute the overall exchange rate, $\Re_0$, into $\Re_a$ and $\Re_i$, representing the apparent rate of O_2 dissociative adsorption and that of the subsequent incorporation of oxygen adatoms into the oxide lattice, respectively. Results of such calculations, using Eqs. 2.9-2.12, are displayed in Fig. 2.6. Apparent activation energies of $\Re_a$ and $\Re_i$ for the different materials are listed in Table 2.1. These were assumed to be constant within the investigated temperature range and used in re-calculation of the isotope fractions $f_{g,o}^{36}$, $f_{g,o}^{34}$ and $f_{g,o}^{32}$ in the effluent pulse as a function of temperature, as displayed (full lines) in Fig. 2.5.

Under the conditions of the experiments, oxygen surface exchange on both mixed ionic-electronic conductors $La_2NiO_{4+\delta}$ and BSCF appears to be limited by the apparent rate of O_2 dissociative adsorption. As can be seen from Fig. 2.6, for both materials $\Re_i$ is almost one order of magnitude higher than $\Re_a$. More systematic studies are needed to clarify which elementary step controls the lumped reaction rate, $\Re_a$ (for example, chemisorption). The results line up with observations made for other oxide ion conducting solids, including the perovskite oxides $La_{0.6}Sr_{0.4}Co_{1-y}Fe_yO_{3-\delta}$ (y=0.2, 0.5, 0.8) [34] and the fluorite-structured 25 mol% erbia-stabilized Bi_2O_3 [13, 20]. In the cited studies, data of oxygen isotopic exchange was obtained using the IEGE technique and analysed using the current two-step exchange model. For the solid electrolyte YSZ investigated in the current study, the rates of O_2 dissociative adsorption and oxygen incorporation reactions are found to compete with each other in the range of temperatures investigated. For this material, an apparent change-over takes place from exchange limited by the rate of oxygen incorporation below ~800 °C to exchange limited by the rate of O_2 dissociative adsorption above this temperature.

2.5 Summary and conclusions

In summary, we have developed a highly versatile technique for measuring the rate of oxygen surface exchange on solid oxide ion conductors. The developed PIE technique is rapid, simple and highly suitable for screening studies to identify candidate materials for potential applications, which rely on oxide materials exhibiting fast surface exchange kinetics (such as solid oxide fuel cells and oxygen transport membranes). The technique can be used in systematic studies towards factors governing oxygen surface exchange. Possible factors include the partial ionic and electronic conductivities, oxygen nonstoichiometry, catalytic properties of the constituent ions, etc. The PIE technique is further amenable to *in situ* analysis of the effect of environmental conditions (temperature and oxygen partial pressure) and gas phase impurities, e.g., H_2O and CO_2, on oxygen surface exchange. No rapid heating/quenching steps are required to facilitate ^{18}O tracer anneal or analysis, as for example in commonly used IEDP and IEGE techniques, while data collection and analysis in the application of PIE are simple and straightforward. Direct measurement of the $^{18}O_2$, $^{16}O^{18}O$, and $^{16}O_2$ isotope fractions in the effluent pulse, i.e., after passing through a continuous flow packed-bed micro-reactor loaded with the oxide powder, by on-line mass spectrometry at the exit of the reactor, enables evaluation of the exchange rate from the net uptake of ^{18}O by the sample, the residence time and surface area available for exchange. The relative distribution of the oxygen isotopomers in the effluent pulse provides insight into the mechanism of the oxygen exchange reaction.

In the current work, the PIE technique has been demonstrated by measuring the exchange rate of selected well-known oxides showing enhanced oxide ionic conductivity, including YSZ, BSCF and $La_2NiO_{4+\delta}$. Measurements were performed, at $pO_2 = 0.21$ atm, in the temperature range 350-900 °C. The results confirm that BSCF exhibits comparatively high exchange rates, which are among the highest values reported in literature. Comparison is made with experimental data from previous studies measured by electrical conductivity relaxation and isotopic exchange depth-profiling methods. For all three materials good agreement is obtained with published data. Analysis of the data from PIE in terms of a model with two consecutive, lumped steps for the exchange reaction shows that the exchange rate exhibited by the mixed conductors $La_2NiO_{4+\delta}$ and BSCF is limited by the apparent rate of dissociative adsorption of O_2 molecules at the oxide surface. For the solid electrolyte YSZ a change-over takes place, from rate-limitations by oxygen incorporation below ~800 °C to rate-limitations by O_2 dissociative adsorption above this temperature. More systematic studies are needed to clarify the elementary reaction(s) controlling both lumped reaction steps in the adopted two-step model.

Acknowledgement

Prof. dr. ir. M. van Sint-Annaland (Eindhoven University of Technology, the Netherlands) is acknowledged for fruitful discussions and suggestions regarding the design and analysis of the plug flow reactor.

References

[1] B.A. Boukamp, The amazing perovskite anode, Nat. Mater., 2 (2003) 294-296.

[2] C.S. Chen, S.J. Feng, S. Ran, D.C. Zhu, W. Liu, H.J.M. Bouwmeester, Conversion of methane to syngas by a membrane-based oxidation-reforming process, Angew. Chem. Int. Ed., 42 (2003) 5196-5198.

[3] T. Hibino, A. Hashimoto, T. Inoue, J. Tokuno, S. Yoshida, M. Sano, A low-operating-temperature solid oxide fuel cell in hydrocarbon-air mixtures, Science, 288 (2000) 2031-2033.

[4] Z.P. Shao, S.M. Haile, A high-performance cathode for the next generation of solid-oxide fuel cells, Nature, 431 (2004) 170-173.

[5] B.C.H. Steele, H. Angelika, Materials for fuel-cell technologies, Nature, 414 (2001) 345-352.

[6] J. Sunarso, S. Baumann, J.M. Serra, W.A. Meulenberg, S. Liu, Y.S. Lin, J.C.D. da Costa, Mixed ionic-electronic conducting (MIEC) ceramic-based membranes for oxygen separation, J. Membr. Sci., 320 (2008) 13-41.

[7] J.R. Wilson, W. Kobsiriphat, R. Mendoza, H.Y. Chen, J.M. Hiller, D.J. Miller, K. Thornton, P.W. Voorhees, S.B. Adler, S.A. Barnett, Three-dimensional reconstruction of a solid-oxide fuel-cell anode, Nat. Mater., 5 (2006) 541-544.

[8] J.A. Lane, J.A. Kilner, Measuring oxygen diffusion and oxygen surface exchange by conductivity relaxation, Solid State Ionics, 136 (2000) 997-1001.

[9] B. Ma, U. Balachandran, J.H. Park, C.U. Segre, Determination of chemical diffusion coefficient of $SrFeCo_{0.5}O_x$ by the conductivity relaxation method, Solid State Ionics, 83 (1996) 65-71.

[10] J.E. ten Elshof, M.H.R. Lankhorst, H.J.M. Bouwmeester, Oxygen exchange and diffusion coefficients of strontium-doped lanthanum ferrites by electrical conductivity relaxation, J. Electrochem. Soc., 144 (1997) 1060-1067.

[11] T.H. Lee, Y.L. Yang, A.J. Jacobson, B. Abeles, M. Zhou, Oxygen permeation in dense $SrCo_{0.8}Fe_{0.2}O_{3-\delta}$ membranes: surface exchange kinetics versus bulk diffusion, Solid State Ionics, 100 (1997) 77-85.

[12] G.K. Boreskov, The catalysis of isotopic exchange in molecular oxygen, Adv. Catal.,

15 (1964) 285-339.

[13] B.A. Boukamp, I.C. Vinke, K.J. Devries, A.J. Burggraaf, Surface oxygen-exchange properties of bismuth oxide-based solid electrolytes and electrode materials, Solid State Ionics, 32-3 (1989) 918-923.

[14] M.W. den Otter, B.A. Boukamp, H.J.M. Bouwmeester, Theory of oxygen isotope exchange, Solid State Ionics, 139 (2001) 89-94.

[15] J.A. Kilner, B.C.H. Steele, L. Ilkov, Oxygen self-diffusion studies using negative-ion secondary ion mass-spectrometry (SIMS), Solid State Ionics, 12 (1984) 89-97.

[16] K. Klier, J. Novakova, P. Jiru, Exchange reactions of oxygen between oxygen molecules and solid oxides, J. Catal., 2 (1963) 479-484.

[17] E.K. Kurumchin, M.V. Perfiliev, An isotope exchange study of the behavior of electrochemical systems, Solid State Ionics, 42 (1990) 129-133.

[18] J. Novakova, Isotopic exchange of oxygen ^{18}O between gaseous phase and oxide catalysts, Catalysis Reviews, 4 (1970) 77-89.

[19] D.S. Tannhauser, J.A. Kilner, B.C.H. Steele, The determination of the oxygen self-diffusion and gas solid exchange coefficients for stabilized zirconia by SIMS, Nuclear Instruments & Methods in Physics Research, 218 (1983) 504-508.

[20] B.A. Boukamp, B.A. Vanhassel, I.C. Vinke, K.J. Devries, A.J. Burggraaf, The oxygen-transfer process on solid oxide noble-metal electrodes, studied with impedance spectroscopy, dc polarization and isotope-exchange, Electrochim. Acta, 38 (1993) 1817-1825.

[21] S. Diethelm, A. Closset, J. van Herle, K. Nisancioglu, Determination of chemical diffusion and surface exchange coefficients of oxygen by electrochemical impedance spectroscopy, J. Electrochem. Soc., 149 (2002) E424-E432.

[22] M. Borysiuk, P. Kristiansson, N. Arteaga-Marrero, M. Elfman, P. Golubev, E.J.C. Nilsson, C. Nilsson, J. Pallon, N. Salim, Optimization of ^{18}O measurement using NRA for studies of isotopic content in fossil meteorites, Nuclear Instruments & Methods in Physics Research Section B-Beam Interactions with Materials and Atoms, 269 (2011) 2229-2232.

[23] S. Bedrane, C. Descorme, D. Duprez, $^{16}O/^{18}O$ isotopic exchange: A powerful tool to

investigate oxygen activation on M/$Ce_xZr_{1-x}O_2$ catalysts, Appl. Catal., A, 289 (2005) 90-96.

[24] F. Dong, A. Suda, T. Tanabe, Y. Nagai, H. Sobukawa, H. Shinjoh, A. Sugiura, C. Descorme, D. Duprez, Characterization of the dynamic oxygen migration over Pt/CeO_2-ZrO_2 catalysts by $^{18}O/^{16}O$ isotopic exchange reaction, Catal. Today, 90 (2004) 223-229.

[25] R.A. De Souza, R.J. Chater, Oxygen exchange and diffusion measurements: the importance of extracting the correct initial and boundary conditions, Solid State Ionics, 176 (2005) 1915-1920.

[26] P. Fielitz, G. Borchardt, On the accurate measurement of oxygen self-diffusivities and surface exchange coefficients in oxides via SIMS depth profiling, Solid State Ionics, 144 (2001) 71-80.

[27] E. Boehm, J.M. Bassat, M.C. Steil, P. Dordor, F. Mauvy, J.C. Grenier, Oxygen transport properties of $La_2Ni_{1-x}Cu_xO_{4+\delta}$ mixed conducting oxides, Solid State Sci., 5 (2003) 973-981.

[28] S.L. Shannon, J.G. Goodwin, Characterization of catalytic surfaces by isotopic-transient kinetics during steady-state reaction, Chem. Rev., 95 (1995) 677-695.

[29] C.C. Kan, H.H. Kan, F.M. van Assche, E.N. Armstrong, E.D. Wachsman, Investigating oxygen surface exchange kinetics of $La_{0.8}Sr_{0.2}MnO_{3-\delta}$ and $La_{0.6}Sr_{0.4}Co_{0.2}Fe_{0.8}O_{3-\delta}$ using an isotopic tracer, J. Electrochem. Soc., 155 (2008) B985-B993.

[30] A. Bueno-Lopez, K. Krishna, M. Makkee, Oxygen exchange mechanism between isotopic CO_2 and Pt/CeO_2, Appl. Catal., A, 342 (2008) 144-149.

[31] S.B. Adler, X.Y. Chen, J.R. Wilson, Mechanisms and rate laws for oxygen exchange on mixed-conducting oxide surfaces, J. Catal., 245 (2007) 91-109.

[32] K. Klier, E. Kucera, Theory of exchange reactions between fluids and solids with tracer diffusion in solid, J. Phys. Chem. Solids, 27 (1966) 1087-1093.

[33] V.S. Muzykantov, G.K. Boreskov, G.I. Panov, Kinetics of exchange and species of oxygen on surface of oxide catalysts, React. Kinet. Catal. Lett., 1 (1974) 315-319.

[34] M.W. den Otter, PhD thesis A study of oxygen transport in mixed conducting

oxides using isotopic exchange and conductivity relaxation, University of Twente, Enschede, 2000.

[35] L. Wang, R. Merkle, J. Maier, T. Acarturk, U. Starke, Oxygen tracer diffusion in dense $Ba_{0.5}Sr_{0.5}Co_{0.8}Fe_{0.2}O_{3-\delta}$ films, Appl. Phys. Lett., 94 (2009) 071908-1-3.

[36] C. Perego, S. Peratello, Experimental methods in catalytic kinetics, Catal. Today, 52 (1999) 133-145.

[37] Y. Ji, J.A. Kilner, M.F. Carolan, Electrical properties and oxygen diffusion in yttria-stabilised zirconia (YSZ)-$La_{0.8}Sr_{0.2}MnO_{3-\delta}$ (LSM) composites, Solid State Ionics, 176 (2005) 937-943.

[38] J.A. Kilner, C.K.M. Shaw, Mass transport in $La_2Ni_{1-x}Co_xO_{4+\delta}$ oxides with the K_2NiF_4 structure, Solid State Ionics, 154 (2002) 523-527.

[39] G. Kim, S. Wang, A.J. Jacobson, L. Reimus, P. Brodersen, C.A. Mims, Rapid oxygen ion diffusion and surface exchange kinetics in $PrBaCo_2O_{5+x}$ with a perovskite related structure and ordered A cations, J. Mater. Chem., 17 (2007) 2500-2505.

[40] P.S. Manning, J.D. Sirman, R.A. De Souza, J.A. Kilner, The kinetics of oxygen transport in 9.5 mol % single crystal yttria stabilised zirconia, Solid State Ionics, 100 (1997) 1-10.

Supplementary information

S2.1 Reactor analysis

A series of semi-empirical relations to assure that the reactor operates under plug flow conditions is discussed below. The analysis is mainly based on recommendations and criteria as, for example, reviewed by Perez-Ramirez *et al.* [1], Mederos *et al.* [2], and Kapteyn and Moulijn [3].

1. Minimum reactor diameter. Wall flow leads to enhanced axial dispersion because of a higher flow in regions near the wall where the packing void fraction is higher. A criterion to neglect wall effects in fixed-bed reactors is [1]

$$\frac{d_\mathrm{r}}{d_\mathrm{p}} > 10 \tag{S2.1}$$

where d_r and d_p are the reactor and particle diameters, respectively.

2. Minimum packed-bed length. Axial mass dispersion is always present, but can be minimized by selecting a proper value of the bed length, $L_\mathrm{pb,}$ to particle diameter, d_p, ratio [1]

$$\frac{L_\mathrm{pb}}{d_\mathrm{p}} > \frac{20n}{Pe}\ln\left(\frac{1}{1-x}\right) \tag{S2.2}$$

where n denotes the reaction order, x the fractional conversion, and Pe the Péclet particle number. A first order rate law for isotopic exchange is in accord with McKay's law [4, 5]. For operation in laboratory scale reactors (i.e., at low Reynold numbers), a value of $Pe \approx 0.5$ is commonly used to check the criterion [6]. A rule of thumb for criterion (S2.2) is [1]

$$\frac{L_{\mathrm{pb}}}{d_{\mathrm{p}}} > 50 \qquad \text{(S2.3)}$$

3. Interphase (external or extraparticle) mass transfer. To minimize concentration gradients between the external surface of oxide particles and adjacent bulk gas regions, the following criterion must be fulfilled for an isothermal n^{th} order irreversible reaction [1]

$$Ca = \frac{0.5\,\Re_{\mathrm{vol}}}{S_{\mathrm{p}} k_{\mathrm{O_2}} c_{\mathrm{b}}} < \frac{0.05}{|n|} \qquad \text{(S2.4)}$$

where Ca denotes the dimensionless Carberry number, $\Re_{\mathrm{vol}}$ the exchange rate per unit particle volume, S_{p} the specific surface area of the particle, $k_{\mathrm{O_2}}$ the mass transfer coefficient, and c_{b} the concentration of oxygen in the bulk gas, respectively. The presence of interphase concentration gradients can be recognized when the apparent exchange rate is a function of the reactant flow rate [3]. Moreover, if the apparent activation energy is less than 20 kJ mol^{-1}, interphase diffusion limitations are highly suspected [7]. A list of symbols is provided at the end of this section.

4. Intraparticle (internal) mass transfer. Internal concentration gradients may arise in pores of individual oxide particles. These are excluded in the present study by measuring oxide powders obtained by crushing dense ceramics.

5. Pressure drop across the packed bed. The axial pressure drop across the entire bed can be calculated using the Ergun equation [8]

$$\Delta P_{\mathrm{b}} = L_{\mathrm{pb}}\left(\frac{150\,\mu_{\mathrm{g}}}{d_{\mathrm{p}}^{2}}\frac{(1-\varepsilon)^{2}}{\varepsilon^{3}}u + \frac{1.75\,\rho_{\mathrm{g}}}{d_{\mathrm{p}}}\frac{(1-\varepsilon)}{\varepsilon^{3}}u^{2}\right) \qquad \text{(S2.5)}$$

where μ_{g} is the (dynamic) gas viscosity, ε the void fraction of the bed, u the superficial velocity, and ρ_{g} the gas density. A rule of thumb is that the pressure drop should be lower than ~20%. If the particle size d_p is too small a significant pressure drop is obtained. In this case the problem may be resolved by mixing the oxide particles with inert particles with larger size [9].

To exemplify the validity of the different criteria in PIE measurements, calculations were performed using experimental conditions and data for $La_2NiO_{4+\delta}$. Results of these calculations are given in Table S2.1.

Table S2.1 Evaluation of selected plug flow criteria (see text).

T (°C)	x	$\frac{20n}{Pe}\ln\left(\frac{1}{1-x}\right)$	Ca	ΔP_b (atm)
500	1.1%	0.4	1.1E-06	0.14
550	3.4%	1.4	3.5E-06	0.16
600	8.6%	3.6	8.8E-06	0.17
650	23.0%	10.4	2.5E-05	0.19
700	49.1%	27.0	6.2E-05	0.21
750	80.2%	64.7	1.4E-04	0.23

The experimental values for L_{pb} = 15 mm, d_p=28.9 µm, d_r = 2 mm yield

$$L_{pb}/d_p = 519 \quad \text{and} \quad d_r/d_p = 69.2$$

which ratios comply with the requirements for a minimum reactor diameter and minimum bed length. The calculated Carberry numbers are very small (mainly due to the small particle size), and indicate the absence of interphase concentration gradients up to a high conversion (x), which corresponds to a high level of depletion of ^{18}O from the gas phase. The calculations further demonstrate that in this case the use of larger particles could have been considered to overcome the pressure drop problem at high temperatures.

S2.2 Blank experiments, variation of packed-bed length and carrier gas flow rate

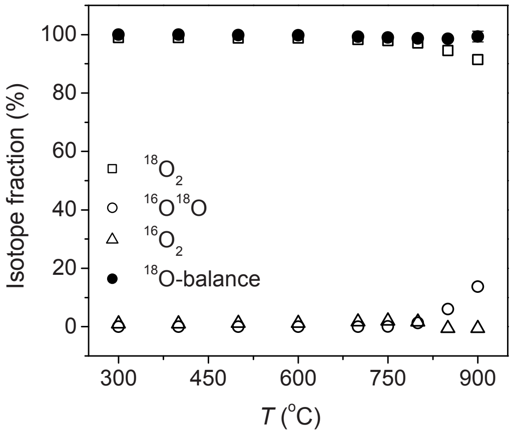

Fig. S2.1 (a)

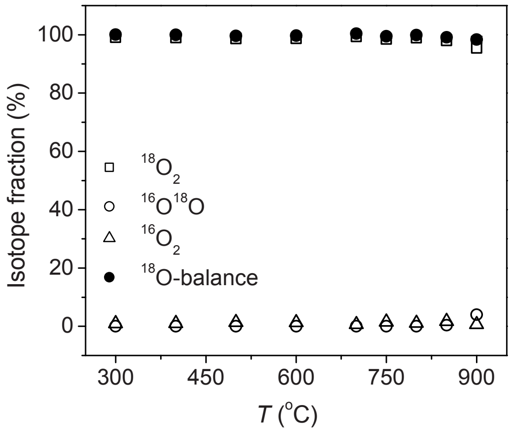

Fig. S2.1 (b)

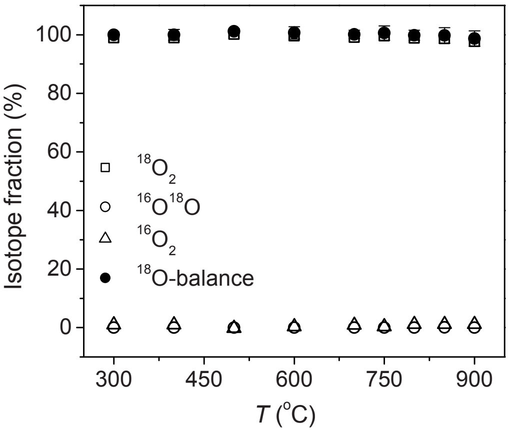

Fig. S2.1(c)

Fig. S2.1 Oxygen isotope fractions ($^{18}O_2$, $^{16}O^{18}O$ and $^{16}O_2$) in the effluent pulse and ^{18}O-balance as a function of temperature from PIE measurements for an empty reactor carried out at different carrier gas flow rates: (a) F_0 = 25 NTP ml min^{-1}, (b) F_0 = 50 NTP ml min^{-1}, and (c) F_0 = 100 NTP ml min^{-1}. Note that some isotope fractionation only occurs at the highest temperatures and lowest flow rate (F_0 = 25 NTP ml min^{-1}), indicating some gas mixing of the pulse with the carrier gas (due to axial dispersion) and catalytic activity of the empty quartz reactor.

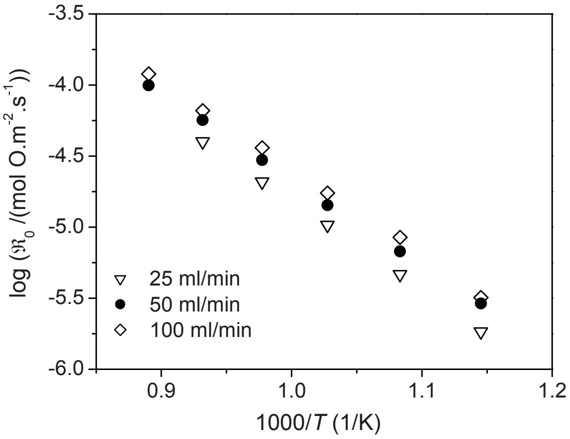

Fig. S2.2 (a)

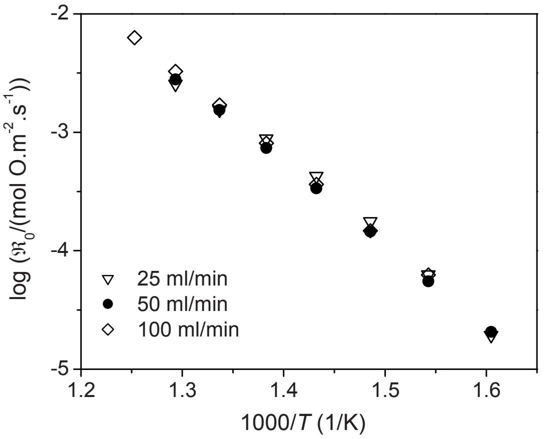

Fig. S2.2 (b)

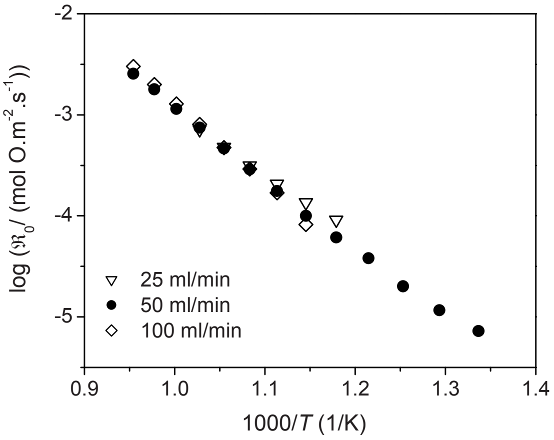

Fig. S2.2(c)

Fig. S2.2 Oxygen exchange rate ($\Re_0$) as a function of inverse temperature assessed from PIE measurements carried out at different carrier gas flow rates, for (a) YSZ, (b) BSCF, and (c) $La_2NiO_{4+\delta}$. Flow rates are indicated in the figures. The good agreement noted between the exchange rates obtained at different flow rates suggests the absence of significant interphase concentration gradients in the experiments.

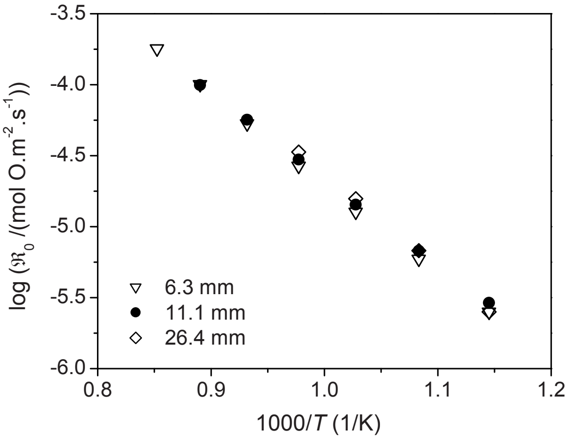

Fig. S2.3 Oxygen exchange rate ($\Re_0$) of YSZ as a function of inverse temperature assessed from PIE measurements carried out at different packed-bed lengths as indicated in the figure. Like the results in Fig. S2.2, the results verify the absence of significant interphase concentration gradients.

S2.3 List of symbols

Ca	Carberry number [-]
c_b	concentration of oxygen in the bulk gas [mol.m^{-3}]
d_p	particle diameter [m]
d_r	reactor diameter [m]
k_{O_2}	mass transfer coefficient [m.s^{-1}]
L_{pb}	bed length [m]
n	reaction order [-]
Pe	Péclet particle number [-]
u	superficial velocity [m.s^{-1}]
$\Re_{vol}$	exchange rate per unit particle volume [mol O. s^{-1}.m^{-3}]
S_p	specific surface area of the particle [m^2.m^{-3}]
x	fractional conversion [-]
ΔP_b	pressure drop across the packed bed [Pa]
μ_g	(dynamic) gas viscosity [kg.m^{-1}.s^{-1}]
ε	void fraction of the bed [-]
ρ_g	gas density [kg.m^{-3}]

References

[1] J. Perez-Ramirez, R.J. Berger, G. Mul, F. Kapteijn, J.A. Moulijn, The six-flow reactor technology - a review on fast catalyst screening and kinetic studies, Catal. Today, 60 (2000) 93-109.

[2] F.S. Mederos, J. Ancheyta, J.W. Chen, Review on criteria to ensure ideal behaviors in trickle-bed reactor, Appl. Catal., A, 355 (2009) 1-19.

[3] F. Kapteijn, J.A. Moulijn, Handbook of Heterogeneous Catalysis, 2nd Ed., Wiley-VCH Verlag GmbH & Co. KGaA, Weinheim, 2008.

[4] K. Klier, J. Novakova, P. Jiru, Exchange reactions of oxygen between oxygen molecules and solid oxides, J. Catal., 2 (1963) 479-484.

[5] D.S. Tannhauser, J.A. Kilner, B.C.H. Steele, The determination of the oxygen self-diffusion and gas solid exchange coefficients for stabilized zirconia by SIMS, Nuclear Instruments & Methods in Physics Research, 218 (1983) 504-508.

[6] J. Perez-Ramirez, J.M. Garcia-Cortes, F. Kapteijn, G. Mul, J.A. Moulijn, C.S.M. de Lecea, Characterization and performance of Pt-USY in the SCR of NO_x with hydrocarbons under lean-burn conditions, Appl. Catal., B, 29 (2001) 285-298.

[7] C. Perego, S. Peratello, Experimental methods in catalytic kinetics, Catal. Today, 52 (1999) 133-145.

[8] S. Ergun, Mass-transfer rate in packed columns - its analogy to pressure loss, Chem. Eng. Prog., 48 (1952) 227-236.

[9] M.H. Al-Dahhan, Y.X. Wu, M.P. Dudukovic, Reproducible technique for packing laboratory-scale trickle-bed reactor with a mixture of catalyst and fines, Ind. Eng. Chem. Res., 34 (1995) 741-747.

Chapter 3

Importance of oxygen vacancies in oxygen surface exchange on phases $La_{1-x}Sr_xCoO_{3-\delta}$

Acknowledgement

Dr. Jianxin Yi is gratefully acknowledged for preparation of samples, measurements of the oxygen exchange rate, and fruitful discussions.

Abstract

To elucidate the relationship between the rate of oxygen surface exchange and the oxygen vacancy concentration in perovskites $La_{1-x}Sr_xCoO_{3-\delta}$, pulse-response ^{18}O-^{16}O isotope exchange measurements were conducted on different compositions in the series. The results show, at $pO_2 = 0.21$ atm and $T = 500$ °C, an exponent of ~0.75 in the power law dependence of the surface exchange rate on oxygen vacancy concentration. The observed correlation clarifies that oxygen vacancies play a major role in the kinetics of surface exchange on $La_{1-x}Sr_xCoO_{3-\delta}$, but does not rule out that other factors, for example, the mobility of oxygen vacancies, play a role. More research is deemed necessary to arrive at a more fundamental understanding of the oxygen surface exchange reaction on these materials.

3.1 Introduction

During the last years, great effort has been devoted to lowering the operating temperature of the solid oxide fuel cell (SOFC) to 500-750 °C, which contributes to lower costs and less demanding material and system requirements [1, 2]. However, the penalty is that the kinetics of the electrode reactions becomes more sluggish and, hence, the SOFC performance diminishes accordingly. Especially, the oxygen reduction reaction at the cathode becomes rate limiting at lower temperatures. To date acceptor-doped perovskite oxides containing late transition metals, e.g., $La_{1-x}Sr_xFe_{1-y}Co_yO_{3-\delta}$, with high electronic and oxygen-ionic conductivities are considered as potential candidates for application as cathodes in intermediate-temperature SOFCs [3, 4].

The performance of a mixed ionic-electronic conducting electrode depends on both oxygen ion diffusion within the bulk and associated surface exchange kinetics [5]. No longer is the electrode reaction confined to the triple-phase boundary (TPB) zone between electrolyte, electrode and gas phase, but is rather distributed across the entire surface area of the mixed conducting electrode. Very high oxide ion diffusivities are observed in acceptor-doped perovskite oxides. Collecting data of isotopic exchange depth-profiling using secondary ion mass spectroscopy (IEDP-SIMS), De Souza and Kilner [6, 7] noted a gross relationship between the surface exchange coefficient, k^*, and the tracer diffusion coefficient, D^*, for different groups of acceptor-doped perovskite and fluorite oxides. For the group of perovskite oxides with high electronic conductivity, comprising $La_{1-x}Sr_xMn_{1-y}Co_yO_{3-\delta}$, $Sm_{1-x}Sr_xCoO_{3-\delta}$, and $La_{0.6}Sr_{0.4}Fe_{0.8}Co_{0.2}O_{3-\delta}$, this relationship to a reasonable approximation can be represented by [8],

$$\log k^* = a + b \log D^* \tag{3.1}$$

where $a \approx -1$ and $b \approx 0.5$. Diffusional transport in the perovskite oxides occurs by hopping between neighbouring lattice sites, and is mediated by the presence of oxygen vacancies. An important corollary of the presumed relationship is that the concentration, or mobility, of the oxygen vacancies plays an important role in the oxygen surface exchange kinetics. To date, however, the origin of Eq. 3.1 still remains unknown.

The oxygen nonstoichiometry of perovskites $La_{1-x}Sr_xCoO_{3-\delta}$ has been widely investigated [9, 10], whilst fast surface exchange kinetics has been demonstrated for $La_{0.3}Sr_{0.7}CoO_{3-\delta}$ [11]. In an attempt to elucidate a possible relationship between the rate of oxygen surface exchange and the concentration of oxygen vacancies in $La_{1-x}Sr_xCoO_{3-\delta}$, the surface exchange rate of different compositions in this series has been investigated using pulse-response ^{18}O-^{16}O isotope exchange (PIE) measurements. The possible role of oxygen vacancies in oxygen surface exchange kinetics is discussed.

3.2 Experimental

3.2.1 Sample preparation and characterization

Powders of $La_{1-x}Sr_xCoO_{3-\delta}$ (x = 0.3 and 0.5) were prepared via a wet-chemical route using EDTA as a complexing agent [12]. To this end, metal nitrates were dissolved with appropriate stoichiometry in deionized water. EDTA was dissolved under stirring in concentrated ammonia (25 %). The EDTA solution was added to the nitrate solution, in an EDTA-to-metal-molar ratio of 1.5:1, and the pH value of the mixed solution was adjusted to ~8 - 9 by adding ammonia. Subsequently, the latter solution was evaporated under heating and stirring until it became highly viscous. Pyrolysis occurred when the gel was further heated in a furnace at 240 °C. The obtained powder was calcined for 2 h in air both at 900 °C and 1000 °C, using heating and cooling rates of 3 °C min^{-1} with milling in between the calcination steps. The thus obtained powder was used for PIE measurements, as described below.

Powders of $La_{1-x}Sr_xCoO_{3-\delta}$ (x = 0.2 and 0.4) were prepared by spray-pyrolysis (CERPOTECH, Trondheim, Norway). These powders were isostatically pressed into discs at 400 MPa, and sintered at 1150 °C for 3 h in air. For pulse isotope exchange measurements, the ceramic discs were crushed into a coarse powder. The fraction passing a 125 μm stainless steel sieve was pre-annealed at 1000 °C for 2 h in air, and sieved again to remove formed agglomerates.

All powders were characterized by X-ray diffraction (Philips PANalytical PW1830), BET surface area (Micromeritics Tristar 3000), and particle size (Mastersizer 2000, Malvern) measurements.

3.2.2 Pulse-response ^{18}O - ^{16}O isotope exchange measurements

PIE measurements were performed in the temperature range 300 - 750 °C, at $pO_2 = 0.21$ atm, using a continuous flow packed-bed microreactor. During the measurement, the oxide powder was loaded between two quartz wool plugs in the center of the quartz tubular micro-reactor with inner diameter 2 mm. The length of the packed bed varied typically between 6 - 9 mm. Values for the mass of the powder, together with the surface area determined by the multipoint Brunauer, Emmett and Teller (BET) method using N_2 (77 K) gas adsorption data, are listed in Table 3.1. The estimated average particle size, d_{50}, of all powders was in the range of 0.3-0.6 μm. Prior to the measurements, the oxide bed was pre-annealed under flowing synthetic air (50 NTP ml min^{-1}) at 850 °C for 2 h in order to remove possible adsorbates such as CO_2 and H_2O, and subsequently cooled at a rate of 3 °C min^{-1} to the temperature where the

Table 3.1 BET surface area and mass of powder used in PIE measurements of different compositions $La_{1-x}Sr_xCoO_{3-\delta}$.

$La_{1-x}Sr_xCoO_{3-\delta}$	S_{BET} ($m^2 g^{-1}$)	Mass (g)
$x = 0.2^*$	0.31	0.0315
$x = 0.3$	2.54	0.0393
$x = 0.4^*$	0.31	0.0281
$x = 0.5$	3.09	0.0433

* Powders obtained from crushed ceramics; see Section 3.2.1.

measurements were started, usually at room temperature. The response to an $^{18}O_2/N_2$ pulse, with the same pO_2 as the carrier gas passing through the reactor was analyzed by on-line mass spectrometry (Omni Star^{TM} GSD 301 Pfeiffer-Vacuum) at the exit of the reactor. A six-port valve with a 500 µl sample loop was used for injection of the $^{18}O_2/N_2$ pulse into the $^{16}O_2$/He carrier gas flow stream. Oxygen isotope gas was purchased from Sigma-Aldrich (> 99 atom % $^{18}O_2$). Nitrogen used as diluent for the $^{18}O_2$ gas was also used for internal calibration of the mass spectrometer. A detailed description of the experimental procedure and equipment used for PIE measurements is presented in Chapter 2 of this thesis.

The packed-bed microreactor was designed to approximate ideal plug flow behavior. Different flow rates of 25, 50 and 100 NTP ml min^{-1} were employed. No evidence of external mass transfer limitations was observed in this range of flow rates. The mean residence time varied between 3 to 26 ms, being a function of the gas flow rate, packed bed and temperature. The isotopic exchange measurements were performed under conditions of negligible uptake of ^{18}O by the oxide, relative to the number of ^{16}O oxygen present in the oxide. The overall surface exchange rate, $\Re_0$, was calculated from

$$\Re_0 = \frac{n_\mathrm{r}}{\tau_\mathrm{r} S_\mathrm{r}} \ln\left(\frac{f_\mathrm{g,i}^{18}}{f_\mathrm{g,o}^{18}}\right) \tag{3.2}$$

where $f_\mathrm{g,i}^{18}$ and $f_\mathrm{g,o}^{18}$ are the ^{18}O isotope molar fractions in the pulse at the inlet and outlet of the reactor, respectively, n_r the total number of oxygen atoms in the free volume of the packed bed, S_r the total surface area of the powder within the packed bed, and τ_r the average residence time of the labeled gas in the reactor. The value of f_g^{18} was calculated from

$$f_\mathrm{g}^{18} = 0.5 f_\mathrm{g}^{34} + f_\mathrm{g}^{36} \tag{3.3}$$

where f_g^{34} and f_g^{36} are the isotope fractions of $^{16}O^{18}O$ and $^{18}O_2$, respectively.

3.3 Results and discussion

3.3.1 X-ray powder diffraction

X-ray diffraction patterns of as-calcined $La_{1-x}Sr_xCoO_{3-\delta}$ powders recorded at room temperature are shown in Fig. 3.1. For each of the compositions, a single phase perovskite structure is observed. No evidence is found for second phase formation. At room temperature, the crystal structure of $La_{1-x}Sr_xCoO_{3-\delta}$ changes from rhombohedral (space group $R\bar{3}c$) to cubic (space group $Pm\bar{3}m$) for x ≥ 0.55. This gradual transition can be monitored by the degree of peak slitting. The present results are in agreement with data published by van Doorn *et al.* [13] and Mastin *et al.* [14].

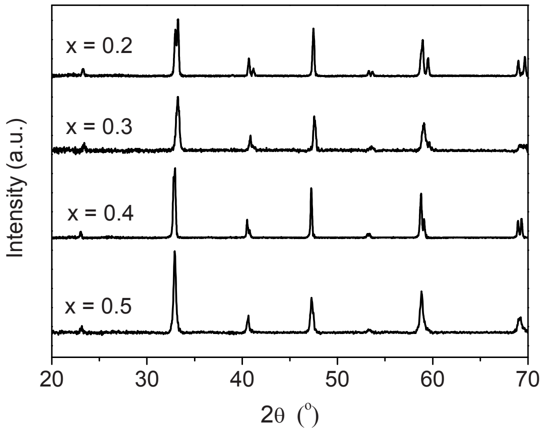

Fig. 3.1 X-ray powder diffraction patterns of $La_{1-x}Sr_xCoO_{3-\delta}$.

3.3.2 Oxygen surface exchange

The overall surface exchange rate, $\Re_0$, calculated from data of PIE measurements on different compositions $La_{1-x}Sr_xCoO_{3-\delta}$, using Eq. 3.2, as a function of inverse temperature is shown in Fig. 3.2. Corresponding activation energies for $\Re_0$ are listed in Table 3.2. Values of $\Re_0$ for $La_{1-x}Sr_xCoO_{3-\delta}$ are compared to data obtained using other techniques in Fig. 3.3. To enable comparison, $\Re_0$ from this study was recalculated to obtain the corresponding surface exchange coefficient, using $k^* = \Re_0/c_o$, where c_o is the concentration of oxygen in the oxide. The data from PIE measurements tends to be slightly higher than that measured by isotopic exchange depth-profiling (IEDP) [7]. Good

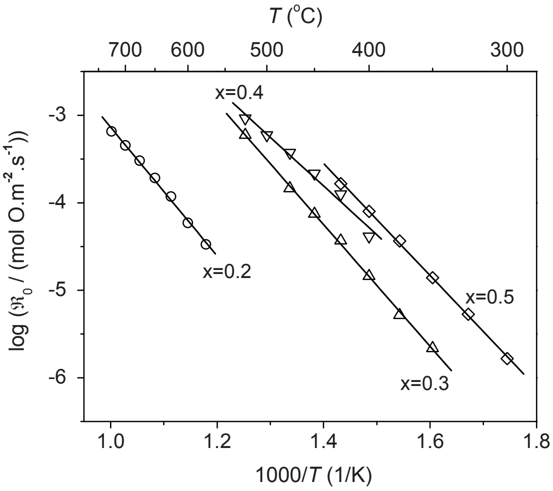

Fig. 3.2 Temperature dependence of the oxygen surface exchange rate for different compositions of $La_{1-x}Sr_xCoO_{3-\delta}$. Flow rate of carrier gas: 50 NTP ml min^{-1}.

Table 3.2 Activation energies (E_a) of the oxygen surface exchange rate for different compositions of $La_{1-x}Sr_xCoO_{3-\delta}$. Values were evaluated from data presented in Fig. 3.2.

x	0.2	0.3	0.4	0.5
E_a (kJ mol^{-1})	141 ± 4	133 ± 2	107 ± 7	123 ± 2

agreement is noted for x = 0.5 with data obtained using electrical conductivity relaxation (ECR) [15].

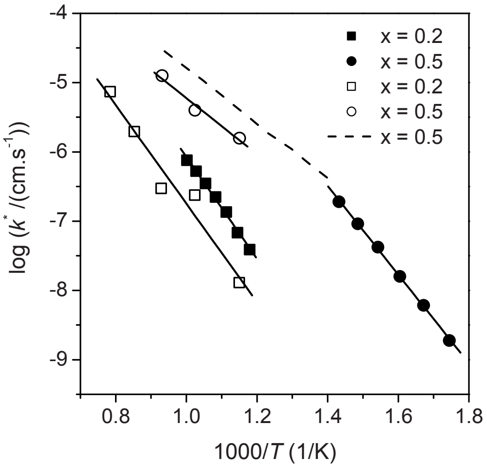

Fig. 3.3 Temperature dependence of the surface exchange coefficient, k^*, for different compositions of $La_{1-x}Sr_xCoO_{3-\delta}$. Full symbols: this work (pO_2 = 0.21 atm); empty symbols: data from IEPD/SIMS (pO_2 = 1 atm) in Ref. 7; dashed line: data from ECR (pO_2 = 0.21 atm) in Ref. 15.

The experimentally accessible temperature window for measurement of $\Re_0$ is constrained by, e.g., residence time and available surface area, and can only be enlarged, shifted down or upwards to a limited extent. Extrapolation is necessary to compare $\Re_0$ for different compositions at similar temperature. Accordingly, Fig. 3.4 compares data of $\Re_0$ for $La_{1-x}Sr_xCoO_{3-\delta}$ at 500 °C. It is evident from this figure that $\Re_0$ increases with x in $La_{1-x}Sr_xCoO_{3-\delta}$. The increase is 2-3 orders in magnitude as one moves from x = 0.2 to x = 0.5. This behavior is concomitant with the associated increase in the oxygen vacancy concentration in $La_{1-x}Sr_xCoO_{3-\delta}$ upon substitution of La for Sr.

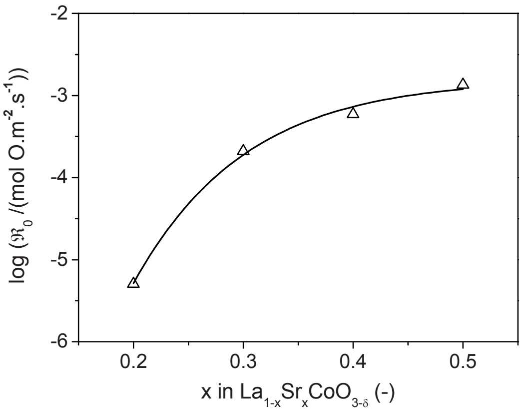

Fig. 3.4 Oxygen surface exchange rate, at 500 °C, as a function of Sr fraction (x) in $La_{1-x}Sr_xCoO_{3-\delta}$.

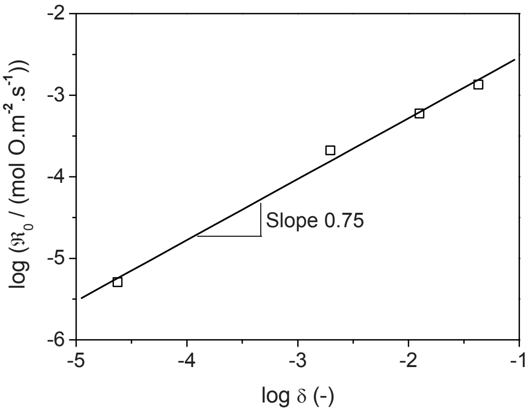

Fig. 3.5 Oxygen surface exchange rate, at 500 °C, as a function of the oxygen vacancy concentration, expressed by the nonstoichiometry parameter δ, for different compositions of $La_{1-x}Sr_xCoO_{3-\delta}$. δ was calculated using the method and thermodynamic parameters outlined in Refs. 9 and 10.

Fig. 3.5 shows a double logaritmic plot of $\Re_0$ as a function of δ, at 500 °C, for $La_{1-x}Sr_xCoO_{3-\delta}$. The corresponding oxygen nonstoichiometry, at $pO_2 = 0.21$ atm, for each of the compositions was calculated using values of the partial molar enthalpy and partial molar entropy evaluated from data of thermogravimetry of the $La_{1-x}Sr_xCoO_{3-\delta}$ system by Mizusaki *et al.* [9, 10]. $\Re_0$ follows a power law with the oxygen vacancy concentration with exponent ~0.75. This value is slightly higher than ~0.5, which may be inferred from the observed correlation (see Eq. 3.1) between the surface exchange coefficient, k^*, and the tracer diffusion coefficient, D^*, for perovskite oxides with prevailing electronic conductivity by De Souza and Kilner [7]. It should, however, be noted that the gradient of the lines in the analysis performed by these authors for a single composition simply reflects the ratio between the activation energies of k^*, and D^*. For $La_{1-x}Sr_xCoO_{3-\delta}$ (x = 0.2, x = 0.5) it is found that $b \approx 0.69$ [7], considerably different from the value of ~0.5, but reasonably close to the value of ~0.75 evaluated from Fig. 3.5.

Given the lack of understanding of the oxygen surface exchange process it is difficult to explain the observed ~0.75 power law dependence on oxygen vacancy concentration. A linear dependence is expected if a single surface vacancy would be involved in the rate-determining step, for example, for trapping of an O_2 molecule. An exponent smaller than unity might expected if, for example, due to partial ordering, the contribution of oxygen vacancies to surface exchange becomes partly annihilated at high vacancy concentrations. The ~0.75 power law dependence is seen to extend over more than 4 orders of magnitude in the concentration of oxygen vacancies. The exponent and wide range, however, do not rule out the possibility that, in part, the mobility of oxygen vacancies plays a role in the determining rate of oxygen surface exchange. In a recent study, using impedance spectroscopy and SIMS depth profiling on thin film microelectrodes, Wang *et al.* [16] arrived at the conclusion that, contrary to perovskites $La_{1-x}Sr_xMn_{1-y}Co_yO_{3-\delta}$, changes of the surface exchange rate induced by compositional variation in the system $Ba_{1-x}Sr_xCo_{1-y}Fe_yO_{3-\delta}$ are predominantly governed by corresponding changes in the oxygen vacancy mobility. Clearly, more research is needed to clarify observations made in this study, and to arrive at a more fundamental understanding and expressions, with which to describe the oxygen exchange process on oxide surfaces.

3.4 Conclusions

The oxygen surface exchange behaviour of perovskites $La_{1-x}Sr_xCoO_{3-\delta}$ (x=0.2, 0.3, 0.4, 0.5) has been evaluated, using pulse-response ^{18}O-^{16}O isotope exchange measurements, with the primary aim to assess the role of oxygen vacancies in surface exchange. The results show, at $pO_2 = 0.21$ atm and $T = 500$ °C, an exponent of ~0.75 in the power law dependence of the surface exchange rate on oxygen vacancy concentration. It is concluded that oxygen vacancies play a major role in the kinetics of oxygen exchange of $La_{1-x}Sr_xCoO_{3-\delta}$. The observed correlation, however, does not rule out that other factors, for example, the mobility of oxygen vacancies, also play a role. More research is deemed necessary to arrive at a more fundamental understanding of the surface exchange process.

References

[1] J.B. Goodenough, Ceramic technology - oxide-ion conductors by design, Nature, 404 (2000) 821-823.

[2] Z.P. Shao, S.M. Haile, A high-performance cathode for the next generation of solid-oxide fuel cells, Nature, 431 (2004) 170-173.

[3] L. Dieterle, P. Bockstaller, D. Gerthsen, J. Hayd, E. Ivers-Tiffee, U. Guntow, Microstructure of nanoscaled $La_{0.6}Sr_{0.4}CoO_{3-\delta}$ cathodes for intermediate-temperature solid oxide fuel cells, Advanced Energy Materials, 1 (2011) 249-258.

[4] H.W. Nie, S.R. Wang, Z.R. Wang, J.Q. Qian, T.L. Wen, Optimization of $La_{0.6}Sr_{0.4}CoO_3$-$Ce_{0.8}Gd_{0.2}O_{1.9}$ composite cathodes for ITSOFCs, Solid State Ionics, 192 (2011) 483-485.

[5] G.W. Coffey, L.R. Pederson, P.C. Rieke, Competition between bulk and surface pathways in mixed ionic electronic conducting oxygen electrodes, J. Electrochem. Soc., 150 (2003) A1139-A1151.

[6] R.A. De Souza, A universal empirical expression for the isotope surface exchange coefficients (k^*) of acceptor-doped perovskite and fluorite oxides, Phys. Chem. Chem. Phys., 8 (2006) 890-897.

[7] R.A. De Souza, J.A. Kilner, Oxygen transport in $La_{1-x}Sr_xMn_{1-y}Co_yO_{3\pm\delta}$ perovskites part II. oxygen surface exchange, Solid State Ionics, 126 (1999) 153-161.

[8] R. Merkle, J. Maier, H.J.M. Bouwmeester, A linear free energy relationship for gas-solid interactions: correlation between surface rate constant and diffusion coefficient of oxygen tracer exchange for electron-rich perovskites, Angew. Chem. Int. Ed., 43 (2004) 5069-5073.

[9] J. Mizusaki, Nonstoichiometry, diffusion, and electrical-properties of perovskite-type oxide electrode materials, Solid State Ionics, 52 (1992) 79-91.

[10] J. Mizusaki, Y. Mima, S. Yamauchi, K. Fueki, H. Tagawa, Nonstoichiometry of the perovskite-type oxides $La_{1-x}Sr_xCo_{3-\delta}$, J. Solid State Chem., 80 (1989) 102-111.

[11] R.H.E. van Doorn, I.C. Fullarton, R.A. De Souza, J.A. Kilner, H.J.M. Bouwmeester, A.J. Burggraaf, Surface oxygen exchange of $La_{0.3}Sr_{0.7}CoO_{3-\delta}$, Solid State Ionics, 96 (1997)

1-7.

[12] R.H.E. van Doorn, H. Kruidhof, A. Nijmeijer, L. Winnubst, A.J. Burggraaf, Preparation of $La_{0.3}Sr_{0.7}CoO_{3-\delta}$ perovskite by thermal decomposition of metal-EDTA complexes, J. Mater. Chem., 8 (1998) 2109-2112.

[13] R.H.E. van Doorn, A.J. Burggraaf, Structural aspects of the ionic conductivity of $La_{1-x}Sr_xCoO_{3-\delta}$, Solid State Ionics, 128 (2000) 65-78.

[14] J. Mastin, M.A. Einarsrud, T. Grande, Structural and thermal properties of $La_{1-x}Sr_xCoO_{3-\delta}$, Chem. Mater., 18 (2006) 6047-6053.

[15] G. Kim, S. Wang, A.J. Jacobson, L. Reimus, P. Brodersen, C.A. Mims, Rapid oxygen ion diffusion and surface exchange kinetics in $PrBaCo_2O_{5+x}$ with a perovskite related structure and ordered A cations, J. Mater. Chem., 17 (2007) 2500-2505.

[16] L. Wang, R. Merkle, J. Maier, Surface kinetics and mechanism of oxygen incorporation into $Ba_{1-x}Sr_xCo_yFe_{1-y}O_{3-\delta}$ SOFC microelectrodes, J. Electrochem. Soc., 157 (2010) B1802-B1808.

Chapter 4

Influence of CO_2 on stability and surface oxygen exchange of the perovskite-type oxide $Ba_{0.5}Sr_{0.5}Co_{0.8}Fe_{0.2}O_{3-\delta}$

Presented at 10th International Conference on Inorganic Membrane (ICIM10), August 18-22, 2008, Tokyo, Japan

Abstract

The influence of CO_2 exposure on the stability and surface oxygen exchange rate of the perovskite-type oxide $Ba_{0.5}Sr_{0.5}Co_{0.8}Fe_{0.2}O_{3-\delta}$ (BSCF) has been investigated in a combined study using thermogravimetry (TG), X-ray powder diffraction (XRD), X-ray photoelectron spectroscopy (XPS), temperature-programmed desorption - mass spectrometry (TPD-MS) and pulse ^{18}O-^{16}O isotope exchange (PIE). The carbonation reaction of BSCF is thermally activated, and found to be fastest at 900 °C, corresponding to the maximum temperature used in the TG experiments. Thermal decomposition of the surface carbonates occurs in a CO_2-free air stream, and is found to be complete beyond a temperature of ~790 °C. The recorded TPD profiles reveal the presence of two peaks, suggesting that the decomposition occurs in a two-stage process. More research is, however, necessary to explain details of the decomposition kinetics. Though at 450 °C, under the exposure conditions studied in this work, only a superficial carbonate layer is formed, with a thickness down to the nanometer scale, its presence is found to have a huge detrimental impact on the surface exchange kinetics of BSCF. PIE measurements, using *in-situ* CO_2 exposure methods, as a function of gas composition (1-20 % CO_2) and temperature (450-700 °C) demonstrate that the overall surface oxygen exchange rate decreases profoundly upon carbonation of BSCF. The exchange rates may only be partially restored to their original values by subsequent annealing of the samples at 850 °C for 5 h in a CO_2-free atmosphere.

4.1 Introduction

Mixed oxygen ionic and electronic conducting perovskite and perovskite-related oxides have attracted considerable attention during the last decades for their potential application as cathode for solid oxide fuel cells (SOFC), and as membrane for oxygen separation. The latter includes their possible implementation in catalytic reactors for, e.g., selective oxidation of hydrocarbons. Among these oxides, $SrCo_{0.8}Fe_{0.2}O_{3-\delta}$ (SCF) shows a high oxygen permeability, which relates to a high concentration of mobile oxygen vacancy defects [1]. However, SCF undergoes an undesired phase transition from a vacancy-disordered cubic perovskite to a vacancy-ordered brownmillerite phase below an oxygen partial pressure (pO_2) of 0.01 atm at ~790 °C. Besides reducing the rate of oxygen permeation, significant differences in lattice volume and expansion behavior between the brownmillerite and cubic perovskite phases imply potential difficulties in the thermal cycling of SCF membranes [2, 3]. To retain the perovskite structure, Sr^{2+} has been partly substituted by Ba^{2+} [4, 5]. The maximum oxygen permeation rate is found for $Ba_{0.5}Sr_{0.5}Co_{0.8}Fe_{0.2}O_{3-\delta}$ (BSCF) [4, 5]. Presently, BSCF and compositions derived thereof are widely investigated for abovementioned applications [6, 7].

Yet another complication to solve before application of the mixed conducting perovskite become feasible involves the surface poisoning by CO_2. The formation of surface carbonates as a result of exposure to CO_2, during which basic earth-alkaline cations (Sr^{2+}, Ba^{2+}) are extracted from the perovskite structure, blocks the surface exchange processes. Arnold *et al*. [8] observed an immediate cessation of the oxygen flux through the BSCF membrane when pure CO_2 was applied as the sweep gas at 875 °C. Analysis of the microstructure after the permeation measurements using transmission electron microscopy (TEM), X-ray diffraction (XRD) and scanning electron microscopy showed that both microstructure and oxygen permeability are recovered when the sweep gas is switched back to helium again [8].

Major aim of this study is to examine the influence of exposure of CO_2 on surface exchange kinetics of BSCF. Measurements are conducted both before, during (i.e., *in situ*) and after exposure of BSCF powders to different CO_2 concentration ambients, exploiting pulse ^{18}O-^{16}O isotope exchange (PIE) as the technique for measurement of the surface exchange rate. In addition, the stability of BSCF in CO_2-containing atmospheres has been studied using combined thermogravimetry (TG), X-ray powder diffraction (XRD), X-ray photoelectron spectroscopy (XPS) and temperature-programmed desorption - mass spectrometry (TPD-MS).

4.2 Experimental

4.2.1 Sample preparation and characterization

BSCF powder was prepared by thermal decomposition of precursor complexes derived from a solution of metal nitrates in appropriate stoichiometry, using ethylenediaminetetraacetic (EDTA) as the complexing agent. The powder obtained was calcined at 800 °C in air for 24 h, and subsequently ball-milled in ethanol. The milled powder was pressed into a disk *via* cold isostatic pressing at 4000 bar, and then sintered at 1100 °C in air for 10 h. Finally, the sintered disk was crushed again into a powder. The fraction of the powder passing a 120-mesh metal sieve was calcined at 950 °C in air for 10 h, and sieved again through a 120-mesh metal sieve. After the procedure described above, the BSCF powder as used for the experiments had a particle size (d_{50}) of 2.7 μm (Mastersizer 2000, Malvern) and a BET surface of 0.21 m^2 g^{-1} (Micromeritics ASAP 2020M). X-ray diffraction (XRD) powder patterns were recorded at room temperature using a Philips PANalytical PW1830 diffractometer. XRD indicated formation of the cubic perovskite phase, and yielded no evidence of second phases or impurities.

4.2.2 Stability tests

The stability of BSCF powder in CO_2-containing atmospheres was investigated using combined thermogravimetry (TG), X-ray powder diffraction (XRD), X-ray photoelectron spectroscopy (XPS) and temperature-programmed desorption - mass spectrometry (TPD-MS).

TG experiments (Setsys 16/18, Setaram) were conducted under a flowing gas stream (40 NTP ml min^{-1}), containing 20 % of CO_2 balanced with air, in the range from room temperature to 900 °C, using a heating rate of 2 °C min^{-1}, with a dwell of 30 min at the maximum temperature before cooling with the same rate to room temperature.

XRD experiments were carried out on powder samples both before and after exposure to a flowing gas mixture (50 NTP ml min^{-1}) containing 20 % CO_2, 21 % O_2, balanced with He (referred to as 20 % CO_2/21 % O_2/He) at 700 °C for 1 h, and subsequently cooled to room temperature at a rate of 3 °C min^{-1} in the same gas stream. For XPS experiments, the BSCF powder was exposed to this gas stream either at 450 or 700 °C for 1 h. The sample exposed at 700 °C was subsequently furnace-cooled to 450 °C under flowing gas conditions. Then, both samples were flushed (50 NTP ml min^{-1}) for 2 h with a CO_2-free gas stream (21 % O_2/He) to remove any adsorbed CO_2, and then cooled to room temperature. The C 1s photoelectron peaks of both samples, before and after removal of a ~1 nm top layer of the sample surface using a 3 keV Ar^+ ion sputtering for 6 s, were recorded using a Quantera SXM (Physical Electronics, Inc.) scanning XPS microscope.

TPD experiments were carried out using the quartz micro-reactor also used for oxygen isotopic exchange experiments as described below. The reactor was loaded with approximately 0.07 g of the BSCF powder. Quartz wool plugs were used on both sides the packed powder bed to ensure its integrity. A gas mixture, containing 20 % CO_2/21 % O_2/He, was fed through the reactor at a flow rate of 50 NTP ml min^{-1}, and at temperatures 450, 500, 600 and 700 °C, respectively, for 1 h. The samples exposed at 500, 600 and 700 °C were furnace-cooled to 450 °C under the same gas flow conditions. Then, all samples were flushed (50 NTP ml min^{-1}) for 2 h with a 21 % O_2/He gas mixture, and furnace-cooled to room temperature under the same gas flowing conditions. Data acquisition was carried out by heating, either at rate of 2 or 10 °C min^{-1}, each of the samples from room temperature to 850 °C in a CO_2-free gas stream (21 % O_2/He) at a flow rate of 50 NTP ml min^{-1}, and monitoring the mass spectrometer response at m/z 44 for CO_2 at the exit of the reactor.

4.2.3 Oxygen isotopic exchange experiments

Pulse ^{18}O-^{16}O isotope exchange (PIE) measurements were performed in the range of temperature 350-700 °C at a pO_2 of 0.21 atm, using a continuous flow packed-bed micro-reactor. During measurements, approximately 0.07 g of BSCF powder was loaded in the center of the quartz tubular micro-reactor having an inner diameter of 2 mm. A $^{16}O_2$-based gas mixture was used as the carrier gas with a flow rate of 50 NTP ml min^{-1}. The response to an $^{18}O_2$-enriched gas pulse (500 μl) fed through the reactor, with the same pO_2 as the carrier gas, was analyzed by on-line mass spectrometry (Omni Star^{TM} GSD 301, Pfeiffer-Vacuum) at the exit of the reactor. Prior to a series of measurements on a given sample, the sample loaded in the reactor was pre-treated at 850 °C for 2 h under flowing, synthetic air to remove any adsorbed water and CO_2, and subsequently cooled to room temperature at a rate of 3 °C min^{-1}. Measurements were conducted either at fixed temperature, monitoring the surface exchange rate as a function of time during a specific CO_2 exposure treatment, or measured as a function of temperature during heating. In the latter case, the temperature was increased stepwise to a new set point, with a heating rate of 3 °C min^{-1}, at which the packed-bed micro-reactor was pre-equilibrated 0.5 h before data collection. Blank experiments revealed no exchange activity of the quartz micro-reactor.

Data acquisition was carried out by measuring integrated pulse values of oxygen isotopomers $^{18}O_2$ and $^{16}O^{18}O$. The average result of three measurements was used for calculation of the surface exchange rate, $\Re_0$ (mol O.m^{-2}.s^{-1}), from:

$$\Re_0 = \frac{n_r}{\tau_r S_r} \ln\left(\frac{f_{g,i}^{18}}{f_{g,o}^{18}}\right) \tag{4.1}$$

where $f_{g,i}^{18}$ and $f_{g,o}^{18}$ are the ^{18}O isotope molar fractions in the pulse at the inlet and outlet of the reactor, respectively, n_r the total number of oxygen atoms in the free volume of the packed bed, S_r the total surface area of the powder within the packed bed, and τ_r the average residence time of the labeled gas in the reactor. f_g^{18} was calculated from

$$f_g^{18} = 0.5 f_g^{34} + f_g^{36} \tag{4.2}$$

where f_g^{34} and f_g^{36} are the isotope fractions of $^{16}O^{18}O$ and $^{18}O_2$, respectively. More details of the pulse isotope exchange experiments and theory are described in Chapter 2 of this thesis.

To study the influence of CO_2 on surface oxygen exchange of BSCF, different tests were performed, in which PIE measurements were conducted on BSCF powder samples before, during (i.e., *in situ*) and after they experienced different exposure conditions, e.g. CO_2 concentration, temperature, etc.

(i) In the first of these, PIE measurements were conducted as a function of temperature before and after exposure of the sample to a gas mixture containing 20 % CO_2 at a selected temperature. The latter treatment was carried out *in situ* in the reactor at 700 °C for 1 h, during which the sample was exposed to a gas mixture of 20 % CO_2/21 % O_2/He at a flow rate of 50 NTP ml min^{-1}, and cooled to room temperature at a rate of 3 °C min^{-1} in the same gas stream. After these experiments, the sample was annealed again at 850 °C for 5 h under flowing CO_2-free synthetic air, and subsequently cooled to room temperature at a rate of 3 °C min^{-1} under the same gas flow condition. Hereafter, additional PIE measurements were conducted to see to which extent recovery of the exchange rate had occurred by the latter treatment.

(ii) The surface exchange rate was monitored as a function of temperature during *in-situ* exposure of a pristine sample to a gas mixture containing 20 % CO_2. In this experiment, the carrier gas during PIE measurements was changed from 21 % $^{16}O_2$/ He to 20 % CO_2/21 % $^{16}O_2$ /He.

(iii) In this test, the surface exchange rate of a pristine sample was first measured under CO_2-free conditions at 450 °C. Next, the carrier gas was changed from 21 % $^{16}O_2$ / He to 1 % CO_2 / 21 % $^{16}O_2$ / He and the surface exchange rate exhibited by the sample was monitored as a function of time. After one full hour of exposure and measurement, the CO_2 concentration in the carrier gas was further increased, which procedure was repeated a number of times to cover the following series of concentrations of CO_2 in the carrier gas: 1, 2, 4 and 8 %. Finally, the carrier gas was changed back to 21 % $^{16}O_2$/He again, thus re-installing CO_2-free conditions, in order to see whether or not the exchange rate would restore to its original value.

(iv) In the final test, the influence of the temperature at which samples are exposed to CO_2 on the recovery of the exchange rate - by subsequent annealing of the samples at elevated temperature in a CO_2-free atmosphere - was investigated. To this end, BSCF powders were exposed to a flowing gas stream with composition 20 % CO_2/21 % O_2/He at either 450, 500, 600 or 700 °C, for 1 h. Those exposed at 500, 600 and 700 °C were furnace-cooled after the treatment to 450 °C in the same gas stream. This was usually accomplished within a few minutes. Subsequently, the samples were flushed (50 NTP ml min^{-1}) for 2 h with a 21 %O_2/He gas mixture, annealed at 850 °C for 5 h and cooled again to 450 °C in the same gas stream, using heating/cooling rates of 3 °C min^{-1}. At the latter temperature, the exchange rate was measured, and compared with that found for the pristine sample.

4.3 Results and discussion

4.3.1 Stability of BSCF under CO_2-containing atmospheres

Fig. 4.1 shows typical experimental data of thermogravimetry of BSCF powder obtained under an atmosphere containing 20 % CO_2. A progressive increase in weight is observed with increasing temperature. The weight increase becomes much more pronounced at temperatures above ~780 °C, and extends up to the maximum temperature of 900 °C. A further weight increase is observed during the half an hour dwell at this temperature, and upon subsequent cooling to ~780 °C. Below the latter temperature, the weight remains virtually constant.

Consistent with literature reports [9-11], the observed weight increase is attributed to carbonation of BSCF during CO_2 exposure, and relates to the presence of earth-alkaline cations (Sr, Ba). The faster rate of carbonation observed above ~780 °C is

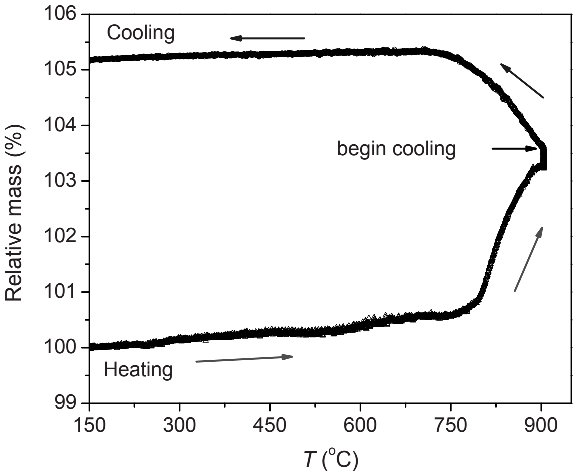

Fig. 4.1 Data of thermogravimetry of BSCF powder. Measurement was performed under flowing 20 % CO_2/air, using heating/cooling rates of 2 °C min^{-1}.

interpreted to reflect the thermal activation of the reaction with CO_2. Even at the highest temperature only partial carbonation has occurred, and, hence, carbonation is found to continue upon subsequent cooling. The overall uptake of CO_2 of ~5.2 wt % observed in the experiment corresponds to approximately 25 % of the BSCF powder that has reacted with CO_2.

According to the data presented in Fig. 4.1, the onset of carbonation occurs in the temperature region 200-300 °C. It should be mentioned here that the oxygen nonstoichiometry of BSCF is known to increase with increasing temperature [4, 5]. Hence, a weight loss is expected upon heating if no reaction with CO_2 would occur. From the powder XRD pattern in Fig. 4.2, it is further evident that BSCF is still the major phase after exposure to 20 % CO_2 at 700 °C for 1 h. The prominent reflections in the diffraction pattern of the carbonated sample are from the cubic perovskite structure. A few small peaks can be assigned to a mixed (Sr, Ba) carbonate [12].

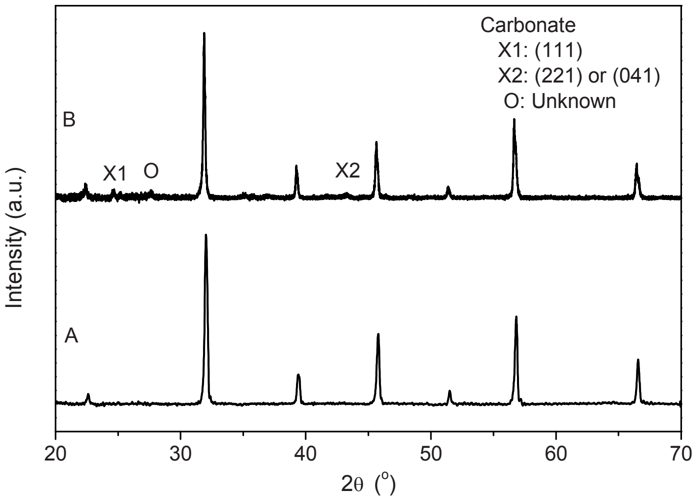

Fig. 4.2 X-ray powder diffraction patterns of BSCF collected at room temperature A) before, and B) after exposure to 20 % CO_2/21 % O_2/He at 700 °C for 1 h.

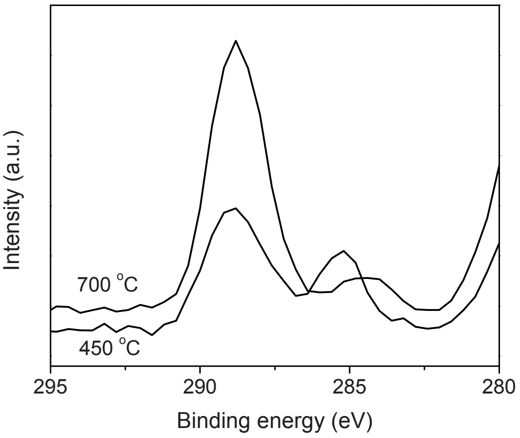

(a)

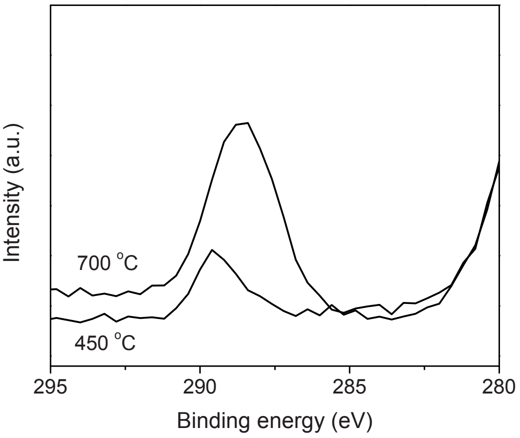

(b)

Fig. 4.3 C 1s XPS spectra of BSCF powder exposed to 20 % CO_2/21 % O_2/He at 450 and 700 °C for 1 h, respectively, (a) before and (b) after Ar^+ sputtering to remove a ~1 nm surface layer.

Analysis of the C 1s spectral region by XPS analysis of samples exposed to 20 % CO_2 for 1 h either at 450 or 700 °C (Fig. 4.3) show two distinct peaks. The peak at binding energy ~289 eV is associated with the presence of CO_3^{2-} groups, while the one at ~285 eV is attributed to some kind of a surface contamination [13]. The data presented in Fig. 4.3 suggests that more carbonates are formed at 700 °C than at 450 °C. The peak associated with the surface contamination vanishes after removal of ~1 nm by short Ar^+ sputtering at an accelerating potential of 3 keV (see Fig. 4.3(b)). However, the intensity of the carbonate peak at ~289 eV is found to decrease concurrently. The latter suggests that under the applied conditions of the treatment, comprising temperature, CO_2 partial pressure and duration of the exposure, only a superficial carbonate layer is formed. In the next paragraph, it is demonstrated that despite its small apparent depth, the carbonated surface forms a passivation layer, greatly reducing the rate of surface oxygen exchange.

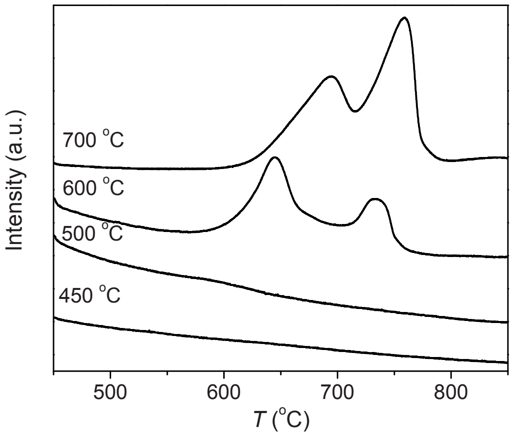

Fig. 4.4 TPD profiles of BSCF powders exposed to 20 % CO_2/21 % O_2/He for 1 h at different temperatures. Data was collected under flowing 21 % O_2/He (50 NTP ml min^{-1}) at a heating rate of 2 °C min^{-1}.

Fig. 4.4 shows the results from TPD experiments on BSCF powders exposed to 20 % CO_2 for 1 h at different temperatures. Distinctly more CO_2 is released, following exposure to CO_2 at higher temperatures. The onset temperature of CO_2 desorption is found to occur at ~620 °C, albeit that the desorption of CO_2 after exposure at 500 and 450 °C is below the detection limit of the mass spectrometric analysis. Under the applied experimental conditions during the TPD experiments, the formed carbonates are effectively decomposed beyond a temperature of ~790 °C.

A noticeable observation is that two peaks are apparent in the TPD profiles obtained after exposure at 600 and 700 °C, suggesting the decomposition of separate and distinct carbonate phases. In general, the decomposition temperature of carbonates is a function of the partial pressure of CO_2, and thus will be influenced by experimental conditions such as flow rate, grain size, etc. Efimov *et al.* [14] calculated the decomposition temperatures of $SrCO_3$ and $BaCO_3$ under different partial pressures of CO_2. At a partial pressure of 10^{-5} bar, decomposition temperatures of ~610 and ~760 °C were calculated for pure $SrCO_3$ and $BaCO_3$, respectively. Rather than the formation of separate carbonate phases, a mixed (Sr, Ba) carbonate may have formed during exposure of BSCF to CO_2. $SrCO_3$ and $BaCO_3$ are known to form solid solutions over the entire range of composition. The decomposition of $Sr_xBa_{1-x}CO_3$ has been observed to take place in a single step [12]. However, it cannot be excluded that if the CO_2 arising from decomposition is not effectively flushed away (e.g., in the case of a low flow rate), a secondary reaction leads to formation of a more stable carbonate, decomposing in second stage. The data presented in Fig. 4.4 was recorded using a heating rate of 2 °C min^{-1}. Fig. 4.5 compares TPD profiles of the samples, carbonated for 1 h at 700 °C, using different heating rates. Contrary to the data recorded at heating rate of 2 °C min^{-1}, CO_2 desorption elutes as a single major peak at the higher heating rate of 10 °C min^{-1}. This may be due to the poorer resolution at the latter heating rate, causing that Yan *et al.* [15] observed one CO_2 desorption peak as well. Supplementary TPD experiments on BSCF, 3 mol %

Zr-substituted BSCF, and 5 and 10 mol % Nb-substituted BSCF, carried out in our laboratory under conditions similar to those in the present study, while employing a heating rate of 2 °C min^{-1}, revealed the presence of two peaks in TPD profiles of the former two, but only a single peak for the latter two compositions [16]. Clearly, more research is necessary to clarify the observations.

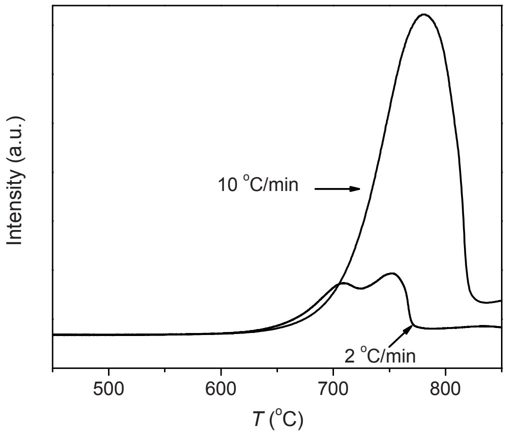

Fig. 4.5 TPD profiles of BSCF powder exposed to 20 % CO_2/21 % O_2/He for 1 h at 700 °C. Data was collected, under flowing 21 % O_2/He (50 NTP ml min^{-1}), at heating rates of 2 and 10 °C min^{-1}.

4.3.2 Oxygen isotopic exchange

Experimental data for the isotopic exchange fractions (f_g^{32} , f_g^{34} and f_g^{36}) as a function of temperature measured after pulsing $^{18}O_2$ (500 μl) through the packed-bed micro-reactor, at a pO_2 of 0.21 atm, loaded with BSCF powder before and after exposure to 20 % CO_2/21 % O_2/He at 700 °C for 1 h are shown in Fig. 4.6. Under the conditions of the experiments, the uptake of ^{18}O by the BSCF powder becomes significant at ~350 °C before and at ~525 °C after carbonation, reflecting the acquired loss of the effective surface exchange rate during CO_2 exposure.

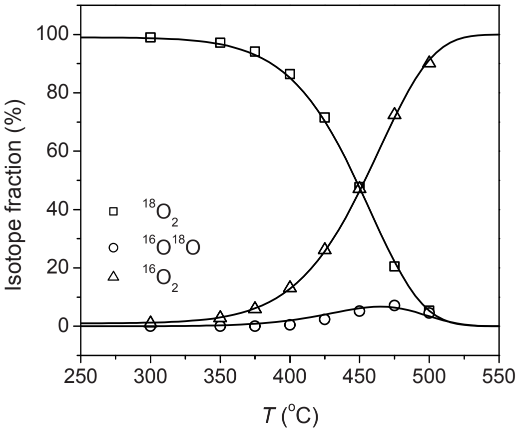

(a)

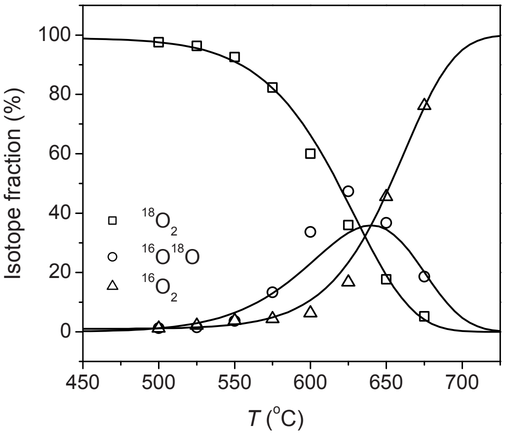

(b)

Fig. 4.6 Temperature dependence of the isotope fractions of $^{18}O_2$, $^{16}O^{18}O$ and $^{16}O_2$ from PIE measurements on (a) pristine BSCF, and (b) after exposure to 20 % CO_2 at 700 °C for 1 h. The drawn lines are a guide to the eyes.

Note further that the decrease in the isotope fraction of $^{18}O_2$ (f_g^{36}) with increasing temperature induces changes in the corresponding fractions of $^{16}O_2$ (f_g^{32}) and $^{18}O^{16}O$ (f_g^{34}). The characteristics of these is regarded as a *fingerprint* for the relative rate of O_2 adsorption to that of oxygen incorporation, as discussed for BSCF and other compositions in Chapter 2 of this thesis. Note the change in these characteristics before and after the exposure to CO_2, which might suggest a corresponding change in the mechanism of the surface exchange reaction. The phenomenon may arise from the heterogeneous nature of the carbonated BSCF surface, and no further attention was given to it.

Fig. 4.7 shows Arrhenius plots of the overall surface exchange rate, $\Re_0$, calculated from data of isotopic exchange, using Eq. 4.1. Clearly, the CO_2 treatment at 700 °C for 1 h is seen to have a huge detrimental effect on the exchange rate of BSCF. The surface exchange rate of carbonated BSCF (*curve B*) is almost 2-3 orders of magnitude lower

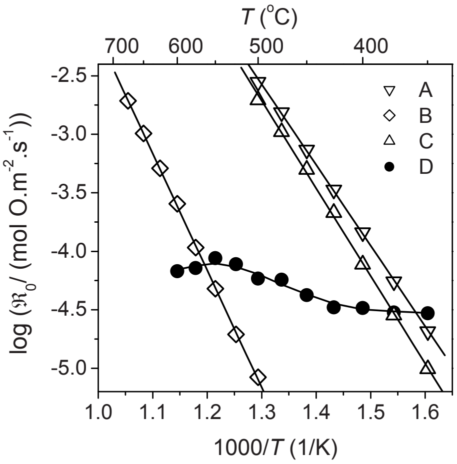

Fig. 4.7 Arrhenius plots of the surface exchange rate ($\Re_0$) of BSCF from PIE measurements: (A) pristine BSCF powder, (B) after exposure to 20 % CO_2 at 700 °C for 1 h, (C) after annealing at 850 °C for 5 h in a CO_2-free atmosphere, and (D) pristine BSCF powder, *in-situ* exposed to 20 % CO_2 during PIE measurements.

than that of pristine BSCF (*curve A*). Also note from Fig. 4.7 (*Curve C*) that the exchange rate is largely recovered after subsequent annealing, at 850 °C for 5 h, of the sample in a CO_2-free atmosphere. The latter observation is consistent with the data from TPD (Fig. 4.4), showing that the carbonates decompose above ~790 °C in a CO_2-free atmosphere. The influence of the exposure temperature maintained during the CO_2 exposure treatment on the recovery of the exchange rate following annealing of the sample at 850 °C in a CO_2-free atmosphere is further discussed below.

The exchange rate of pristine BSCF powder was measured as a function of temperature, the sample being *in-situ* exposed to 20 % CO_2/21 % O_2/He used as the carrier gas in the PIE measurements. Corresponding results are shown in Fig. 4.7 (*Curve D*). Different from the above mentioned results, where the exchange rate of BSCF was found to be detrimentally affected after exposure to 20 % CO_2 containing gas at 700 °C, this result shows that the blocking effect of CO_2 already occurs at moderate temperatures as low as 450 °C. The results are taken to be consistent with those from the XPS experiments presented above (see Fig. 4.3), showing that a superficial carbonate layer is formed after exposure of pristine BSCF powder, at 450 °C to 20 % CO_2 for 1 h.

Additional *in-situ* tests were conducted to study the effect of gas phase concentration of CO_2 on blocking the surface exchange rate of BSCF. These measurements were carried out at a temperature of 450 °C. As seen from Fig. 4.8, the surface exchange rate measured for pristine BSCF powder drops over more than one order of magnitude upon switching to the carrier gas containing 1 % CO_2. As is also obvious from the results, the exchange rate remains on a low level upon further increasing the concentration of CO_2, but does not recover upon switching to a CO_2-free carrier gas again. The results demonstrate that the blocking effect of CO_2 occurs not only at a temperature and gas phase concentration as low as 450 °C and 1 % CO_2, respectively, but also that chemisorption of CO_2 at this temperature leads to irreversible blocking of the surface exchange of BSCF.

Data from TPD confirms that the formed carbonates are decomposed only upon annealing above ~790 °C, by which procedure the exchange rate may be largely recovered, as demonstrated in Figs. 4.4 and 4.7, respectively. The above observations line up with results previously reported by Yan *et al.* [17], showing that the performance of BSCF used as the cathode in a solid oxide fuel cell is adversely and irreversibly affected, in the range 450-500 °C, upon exposure to small concentrations of CO_2 in the gas phase. The authors noted a rapid collapse of the current density, within approx. 20 min after the gas stream was switched from synthetic air to a gas mixture containing 0.28 % CO_2, 21 % O_2, balanced with nitrogen. The performance was found to be partially recovered by switching to the CO_2-free gas stream again, and only full recovery of the electrode kinetics in their study was observed after a thermal treatment at 800 °C for 1 h in pure oxygen [17]. In a more recent study, Bucher *et al.* [9] showed, by means of electrical conductivity relaxation experiments, a severe degradation of the surface oxygen

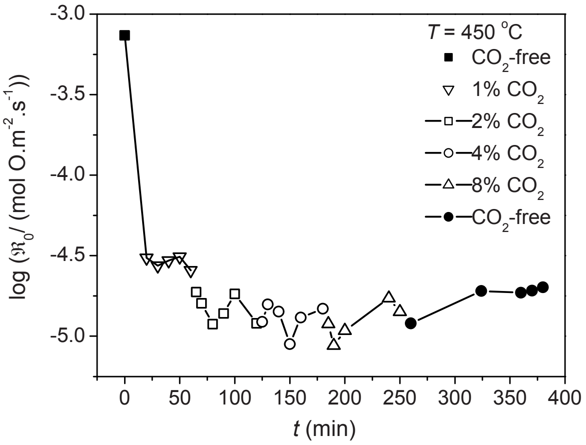

Fig. 4.8 Oxygen surface exchange rate ($\Re_0$) of BSCF, at 450 °C, following *in-situ* exposure to different concentrations of CO_2 in the gas phase. The latter is effectuated by switching to different carrier gases in the PIE measurements.

exchange rate of BSCF after 7 days of operation, at 600 °C, in ambient air (containing 400 ppm of CO_2).

Finally, the influence of the temperature during CO_2 exposure on the extent to which the exchange rate (at 450 °C) can be recovered - by subsequent annealing at 850 °C for 5 h in a CO_2-free atmosphere - was investigated. Corresponding results are shown in Fig. 4.9. These clarify that the adopted post-exposure treatment can only partially regenerate the surface exchange activity of BSCF powder. For example, when BSCF powder is exposed to 20 % CO_2 at 700 °C for 1 h, the post-exposure treatment can recover the surface exchange rate only up to approx. 68 %. It is obvious that a thicker carbonate layer will be produced at a higher temperature and longer duration of the CO_2 exposure. A possible explanation for the data presented in Fig. 4.9 is therefore that the anneal treatment at 850 °C is not effectively enough to form the perovskite phase after extensive exsolution of barium and strontium by the CO_2 exposure treatment. Increasing the temperature of annealing will undoubtedly improve the reformation kinetics of the perovskite phase. The issue was, however, not further investigated.

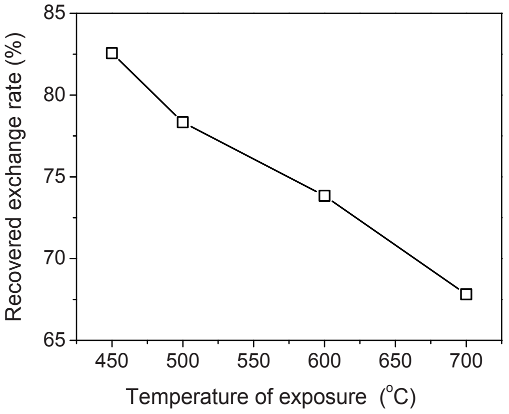

Fig. 4.9 Influence of the temperature during CO_2 exposure on the percentage to which the exchange rate, at 450 °C, can be recovered by post-exposure annealing at 850 °C in a CO_2-free atmosphere.

4.4 Conclusions

The results from this study first of all demonstrate that BSCF is subject to severe carbonation when exposed to CO_2-containing atmospheres. The carbonation reaction is found to be thermally activated. Though at 450 °C, under the exposure conditions studied in this work, only a superficial carbonate layer is formed, the surface of BSCF appears to be highly passivated with respect to surface oxygen exchange as demonstrated by *in-situ* pulse isotopic exchange (PIE) measurements. Thermal decomposition of the surface carbonates occurs in a CO_2-free air stream, and is found to be completed above ~790 °C. Temperature-programmed desorption (TPD) reveals the presence of two peaks, suggesting that the carbonate decomposition occurs in a two-stage process. More research is, however, necessary to explain details of the decomposition kinetics. The exchange rates may only be partially restored to their original values by annealing of the samples at 850 °C for 5 h in a CO_2-free atmosphere. The present results imply severe limitations of using BSCF in CO_2-containing atmospheres, which includes ambient air.

References

[1] Y. Teraoka, H.M. Zhang, S. Furukawa, N. Yamazoe, Oxygen permeation through perovskite-type oxides, Chem. Lett., (1985) 1743-1746.

[2] H. Kruidhof, H.J.M. Bouwmeester, R.H.E. van Doorn, A.J. Burggraaf, Influence of order-disorder transitions on oxygen permeability through selected nonstoichiometric perovskite-type oxides, Solid State Ionics, 63-65 (1993) 816.

[3] S. McIntosh, J.F. Vente, W.G. Haije, D.H.A. Blank, H.J.M. Bouwmeester, Phase stability and oxygen non-stoichiometry of $SrCo_{0.8}Fe_{0.2}O_{3-\delta}$ measured by in situ neutron diffraction, Solid State Ionics, 177 (2006) 833-842.

[4] Z.P. Shao, G.X. Xiong, J.H. Tong, H. Dong, W.S. Yang, Ba effect in doped $Sr(Co_{0.8}Fe_{0.2})O_{3-\delta}$ on the phase structure and oxygen permeation properties of the dense ceramic membranes, Sep. Purif. Technol., 25 (2001) 419-429.

[5] Z.P. Shao, W.S. Yang, Y. Cong, H. Dong, J.H. Tong, G.X. Xiong, Investigation of the permeation behavior and stability of a $Ba_{0.5}Sr_{0.5}Co_{0.8}Fe_{0.2}O_{3-\delta}$ oxygen membrane, J. Membr. Sci., 172 (2000) 177-188.

[6] Z.P. Shao, S.M. Haile, A high-performance cathode for the next generation of solid-oxide fuel cells, Nature, 431 (2004) 170-173.

[7] H.H. Wang, Y. Cong, W.S. Yang, Investigation on the partial oxidation of methane to syngas in a tubular $Ba_{0.5}Sr_{0.5}Co_{0.8}Fe_{0.2}O_{3-\delta}$ membrane reactor, Catal. Today, 82 (2003) 157-166.

[8] M. Arnold, H.H. Wang, A. Feldhoff, Influence of CO_2 on the oxygen permeation performance and the microstructure of perovskite-type $Ba_{0.5}Sr_{0.5}Co_{0.8}Fe_{0.2}O_{3-\delta}$ membranes, J. Membr. Sci., 293 (2007) 44-52.

[9] E. Bucher, A. Egger, G.B. Caraman, W. Sitte, Stability of the SOFC cathode material $(Ba,Sr)(Co,Fe)O_{3-\delta}$ in CO_2-containing atmospheres, J. Electrochem. Soc., 155 (2008) B1218-B1224.

[10] G. Juhasz, Z. Homonnay, K. Nomura, T. Hayakawa, S. Hamakawa, A. Vertes, Microstructural study of the CO_2 absorption in $Sr_xCa_{1-x}Fe_{0.5}Co_{0.5}O_{3-\delta}$, Solid State Ionics, 139 (2001) 219-231.

[11] K. Nomura, Y. Ujihira, T. Hayakawa, K. Takehira, CO_2 absorption properties and characterization of perovskite oxides, (Ba,Ca) (Co,Fe) $O_{3-\delta}$, Appl. Catal., A, 137 (1996) 25-36.

[12] J.M. Criado, M.J. Dianez, M. Macias, M.C. Paradas, Crystalline-structure and thermal-stability of double strontium and barium carbonates, Thermochim. Acta, 171 (1990) 229-238.

[13] V.V. Atuchin, T. Hasanov, V.G. Kesler, A.E. Kokh, L.D. Pokrovsky, Amorphization and chemical modification of β-BaB_2O_4 surface by polishing, Opt. Mater., 23 (2003) 385-392.

[14] K. Efimov, T. Klande, N. Juditzki, A. Feldhoff, Ca-containing CO_2-tolerant perovskite materials for oxygen separation, J. Membr. Sci., 389 (2012) 205-215.

[15] A.Y. Yan, L. Bin, Y.L. Dong, Z.J. Tian, D.Z. Wang, M.J. Cheng, A temperature programmed desorption investigation on the interaction of $Ba_{0.5}Sr_{0.5}Co_{0.8}Fe_{0.2}O_{3-\delta}$ perovskite oxides with CO_2 in the absence and presence of H_2O and O_2, Appl. Catal., B, 80 (2008) 24-31.

[16] C.Y. Yoo, PhD thesis in press, University of Twente, Enschede.

[17] A. Yan, M. Cheng, Y.L. Dong, W.S. Yang, V. Maragou, S.Q. Song, P. Tsiakaras, Investigation of a $Ba_{0.5}Sr_{0.5}Co_{0.8}Fe_{0.2}O_{3-\delta}$ based cathode IT-SOFC - I. The effect of CO_2 on the cell performance, Appl. Catal., B, 66 (2006) 64-71.

Chapter 5

Oxidative dehydrogenation of alkanes using an oxygen-permeable ceramic membrane reactor

Acknowledgement

Prof. dr. ir. Leon Lefferts and Dr. Salvatore Davide Crapanzano are gratefully acknowledged for their support and fruitful discussions.

Abstract

The oxidative dehydrogenation (ODH) reactions of propane and ethane were investigated in a catalytic membrane reactor, incorporating oxygen-permeable membranes based upon $La_2Ni_{0.9}V_{0.1}O_{4+\delta}$ (LNV10) or $Ba_{0.5}Sr_{0.5}Co_{0.8}Fe_{0.2}O_{3-\delta}$ (BSCF). As a compromise between the occurrence of a measureable oxygen flux and excessive homogenous gas phase reactions, the measurements were conducted at an intermediate temperature, either at 550 °C or 650 °C. The results show the dominating role of the oxygen flux across the membrane and that of available sites at the membrane surface in primary activation of the alkane and, hence, in achieving high alkane conversions. The experimental data of ODH of propane and ethane on both membrane materials can be reconciled on the basis of a Mars-van Krevelen mechanism, in which the alkane reacts with lattice oxygen on the membrane surface to produce the corresponding olefin. It is further demonstrated that the oxygen concentration in the gas phase and on the membrane surface is crucial for determining the olefin selectivity.

5.1 Introduction

One of the main ways to utilize light alkanes is their transformation into corresponding olefins. Major techniques for olefin production include steam cracking, fluid catalytic cracking, and catalytic dehydrogenation [1]. Over the past few years, however, oxidative dehydrogenation (ODH) of alkanes has gained much interest [1-7]. While ODH is exothermal, both catalytic dehydrogenation and thermal cracking are endothermal [1]. In the present study, we are primarily concerned with heterogeneous ODH, using a redox-active oxide catalyst, rather than the homogenous gas phase reaction in the presence of gaseous oxygen. The former is consistent with a redox cycle known as the Mars-van Krevelen mechanism [1, 8]. In the reduction cycle, lattice oxygen abstracts hydrogen from the alkane. The resulting alkyl species desorbs as an olefin, while the surface hydroxyl groups formed during reaction recombine and desorb as water, leaving a surface oxygen vacancy (and a reduced metal center) behind. In the oxidation cycle, the catalyst is re-oxidized. Usually, this is done by gas phase oxygen.

The selective oxidation reaction can occur either with insertion of oxygen, such as in the formation of acrolein from propane, or without insertion of oxygen, such as in oxidative dehydrogenation, e.g., the formation of propylene from propane. The importance of lattice oxygen in selective oxidation reactions of hydrocarbons has been recognized already in the early 1950s [9]. How to re-oxidize the catalyst in order to complete the Mars-van Krevelen redox cycle is, though relevant, of second concern, and is further discussed below. The metal-oxygen bond strength of active oxygen sites at the catalyst surface needs be of intermediate strength [8]. If too strong, no reaction at all will occur, if too weak, over-oxidation might occur, leading to combustion products CO_x. It is thus required that the oxide catalyst has an appropriate host structure, containing redox active metal cations, and is able to adopt oxygen-deficient stochiometries without a collapse of the structure. Favorable catalysts usually are multi-metal oxides with, e.g., a scheelite, fluorite or perovskite structure, often containing vanadium or molybdenum as one of the active constituents [2, 4, 8].

To avoid the presence of unselective weakly-bonded adsorbed oxygen species (e.g. O_2^-, O_2^{2-}, O^-) at the surface, oxygen concentrations in the gas phase need to be minimized during reaction. Several approaches have been pursued to separate reduction and oxidation steps compliant with Mars-van Krevelen type of kinetics, either in time by periodic operation of the reaction by alternate feeding of alkane and oxygen [1], or spatially by using moving bed technology [10] or a catalytic membrane reactor [5, 11-15]. In the latter, a mixed oxide ionic-electronic conducting membrane, endowed with suitable catalytic properties or modified with a suitable catalyst, is employed. The membrane facilitates a continuous and controlled flux of oxide ions to the permeate side exposed to the alkane feed, as illustrated in Fig. 5.1 [13, 15]. The oxygens arrive at the surface via solid-state diffusion exclusively. Accumulation of oxygen in the gas phase can be avoided by matching the oxygen flux through the membrane with the rate of consumption of oxygen by the selective oxidation reaction at the immediate membrane surface.

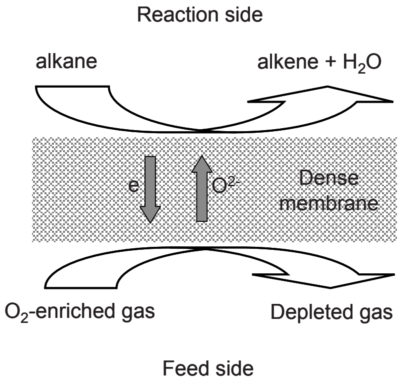

Fig. 5.1 Schematics of catalytic membrane reactor.

Wang *et al.* [13] reported a selectivity of 80.1 % towards ethylene at ethane conversion of 84.2 %, using a catalytic membrane reactor made of $Ba_{0.5}Sr_{0.5}Co_{0.8}Fe_{0.2}O_{3-\delta}$ (BSCF), at 800 °C, whereas a selectivity and conversion of 53.7 % and 83.6 %, respectively, were obtained using BSCF powder in a conventional fixed-bed reactor. When propane was used as reactant, a selectivity of 23.9 % towards propylene at a conversion of 71.8 % was obtained, at 750 °C [15]. In a similar study of ODH of ethane to ethylene, Rebeilleau-Dassonneville *et al.* [12] observed substantial formation of hydrogen as by-product, indicating that the reaction significantly proceeds via gas phase dehydrogenation. The authors arrived at the conclusion that more research is required to clarify the role of the membrane, where it should be noted that both selectivity and yield were found to be enhanced by application of a surface catalyst at the permeate side of the BSCF membrane [12].

The initial principal aim of this research was to explore candidate membrane materials for catalytic selective oxidation of simple alkanes. To this end, the oxygen permeation properties of a number of mixed ionic-electronic conducting oxides were explored, amongst $La_2NiO_{4+\delta}$, $La_2Ni_{0.9}V_{0.1}O_{4+\delta}$, $La_{0.5}Sr_{0.5}CoO_{3-\delta}$, $La_{0.4}Sr_{0.6}Co_{0.8}Fe_{0.2}O_{3-\delta}$, $PrBaCo_2O_{5+\delta}$ and BSCF, which all adopt a perovskite or perovskite-related structure. Unfortunately, none of the membrane materials displayed an oxygen permeation rate which was considered high enough to explore true heterogeneous selective oxidation, i.e., based upon Mars-van Krevelen type of kinetics, without involvement of extensive homogenous gas phase reactions. In this chapter, catalytic membrane reactors, made of either $La_2Ni_{0.9}V_{0.1}O_{4+\delta}$ (LNV10) or BSCF, are exploited for ODH of propane and ethane. Major aim of the present work is to study the influence of the catalytic membrane on the ODH reaction. As a compromise between a measurable oxygen flux, at one hand, and occurrence and extent of the gas phase reactions, at the other hand, the measurements were conducted at an intermediate temperature, either at 550 °C or 650 °C.

5.2 Experimental

5.2.1 Membrane preparation and characterization

Powders of LNV10 and BSCF were prepared by thermal decomposition of precursor complexes derived from a mixed solution, containing the corresponding metal ions in the appropriate stoichiometry, using ethylenediaminetetraacetic (EDTA) as complexing agent. The vanadium-containing solution was prepared by dissolving V_2O_5 in diluted HNO_3. Metal nitrates were used for preparing the other solutions. The powders obtained were calcined in air for 10 h, at 1050 °C and 950 °C for LNV10 and BSCF, respectively. After calcination, the powder was ball-milled in acetone for 5 h. Phase purity of the powders was checked by X-ray diffraction, using a Philips PANalytical PW1830 diffractometer. Powders of LNV10 were pressed into either green tubes or discs via cold isostatic pressing at 400 MPa, and subsequently sintered in air at 1420 °C for 10 h, using heating and cooling rates of 3 °C min^{-1}. Similarly, BSCF powders were pressed into discs and sintered at 1220 °C. The relative density of the dense ceramics was higher than 95 %. Surface of the membranes were carefully polished by hand using 240-mesh SiC grinding paper.

Oxygen permeation through the LNV10 disc membrane (0.97 mm thickness) was measured in the range 575-700 °C. Soda lime silicate glass (AR-glass) rings were used for sealing of the disc into the reactor. After sealing, synthetic air and high purity helium were fed to opposite sides of the membrane at flow rates of 100 and 10 ml min^{-1}, respectively. The effluent gas was analyzed by on line gas chromatography (Varian CP 4900 equipped with molecular sieve 5A PLOT and PoraPLOT Q columns). The gas chromatograph was calibrated using standard gas mixtures (O_2, N_2 balanced with He). Oxygen leakage due to imperfect sealing was evaluated by measuring the nitrogen concentration in the effluent gas. Permeation data were corrected for oxygen leakage, using the corresponding nitrogen concentration. Corrections were less than 1 % of the total oxygen concentration in the effluent gas.

5.2.2 Catalytic experiments

ODH of propane was studied, at 650 °C, using a tubular LNV10 membrane reactor of length 33 mm, and with outside and inside diameters, 6 mm and 4.1 mm, respectively. A gas mixture of oxygen balanced with nitrogen (~100 NTP ml min^{-1}), having oxygen partial pressures in the range 0.1-0.8 atm, was fed to the feed side, while 10 % propane balanced with helium (~10 NTP ml min^{-1}) was fed to the reaction (permeate) side of the LNV10 membrane.

Similarly, studies of ODH of ethane and propane, using BSCF disc membranes, were conducted, at either 550 or 650 °C. The thickness of the membranes varied between 0.8-1.0 mm, while the effective membrane area at the reaction side was about ~0.8 cm^2. For ODH of propane, 10 % propane balanced with helium (~10 NTP ml min^{-1}) was swept along the reaction side, feeding nitrogen (~100 NTP ml min^{-1}) on the opposite side of the membrane. Next, the nitrogen was diluted with oxygen (~100 NTP ml min^{-1}) to give oxygen partial pressures in the range 0.02-0.4 atm. Prior to experiment, the membrane was pre-equilibrated for 5 h, using nitrogen (~100 NTP ml min^{-1}) and helium (~10 NTP ml min^{-1}) as sweep gases along both sides of the membrane. For ODH of ethane, oxygen balanced with nitrogen (~100 NTP ml min^{-1}), having an oxygen partial pressure of 0.1-0.8 atm, was fed to the feed side, while diluted ethane (~10 NTP ml min^{-1}), in the range 24-76 % (v/v) in helium, was fed to the reaction side of the BSCF membrane.

To investigate thermal cracking and/or dehydrogenation of the alkanes in the gas phase, experiments were carried out, using either a quartz tube or discs, replacing tubular or planar membranes, respectively, but keeping reactor volume and flow rate, hence residence times, similar to those as used in the membrane reactor experiments. These experiments, referred to as blank experiments, were carried out both in the absence and presence of gaseous oxygen.

Reactor effluents were analyzed using online gas chromatography, as specified in Section 5.2.1. All reactant gases passed through an ice-bath condenser before injection into the gas chromatograph. The absence of nitrogen in the effluents was taken as evidence that no leakage occurred through the membrane or glass seal. Conversions and selectivities were calculated based on the carbon balance [15]. The conversion was calculated from

$$C = 1 - \frac{nY_{C_nH_{2n+2}}}{\sum m_i Y_i} \tag{5.1}$$

where m_i and Y_i are the number of carbon atoms, and molar fraction of, the *i*-th carbon-containing product, respectively. The selectivity towards the *i*-th carbon-containing product was calculated from

$$S_i = \frac{m_i Y_i}{\sum m_i Y_i - nY_{C_nH_{2n+2}}} \tag{5.2}$$

For all catalytic tests, the carbon balance was within 100 ± 1 %.

5.3 Results and discussion

5.3.1 Characterization of membrane materials

The XRD powder diffraction pattern of LNV10 is presented in Fig. 5.2. Like that of parent La_2NiO_4, its pattern can be indexed on the basis of a tetragonal unit cell, with cell parameters a = 3.873(2) Å and c = 12.659(2) Å. The diffraction pattern of BSCF (not shown) could be indexed on the basis of a simple cubic perovskite structure. In neither case evidence was found for the presence of phase impurities or second phase formation.

Fig. 5.3 shows data of oxygen permeation measurements of LNV10 from this study. Also shown in the figure are literature results for BSCF [16]. From these data it is immediately apparent that, at the moderate temperatures covered experimentally, oxygen transport in LNV10 is much lower than in BSCF. A value of 164 kJ mol^{-1} was calculated from the data in Fig. 5.3 for the activation energy for oxygen permeation through LNV10.

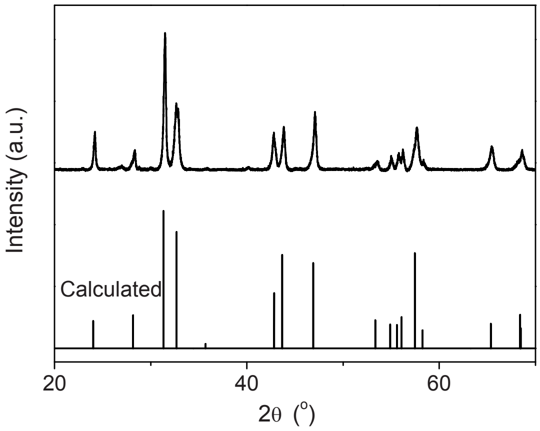

Fig. 5.2 X-ray powder diffraction pattern of LNV10 collected at room temperature. Also shown is the calculated pattern.

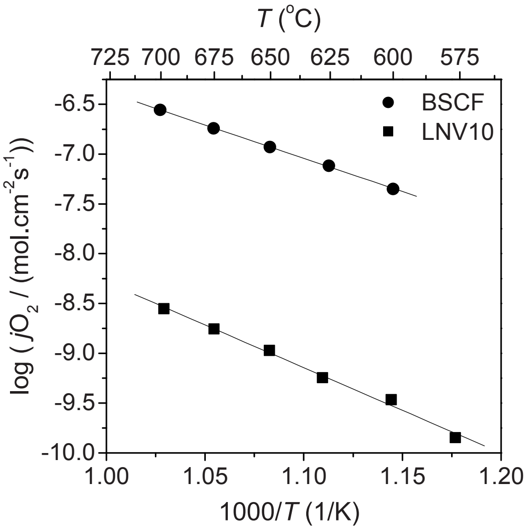

Fig. 5.3 Oxygen permeation flux (jO_2) through a disc LNV10 membrane with thickness 0.97 mm. Synthetic air was used as feed gas (100 NTP ml min^{-1}), while helium was used as purge gas (10 NTP ml min^{-1}) at the permeate side of the membrane. Also shown are data for a BSCF membrane with thickness of 1.5 mm from Ref. 16.

5.3.2 ODH of propane using catalytic membrane reactors

Quantifiable reaction products observed when propane was passed through the tubular LNV10 membrane reactor were H_2, CH_4, CO, CO_2, H_2O, C_2H_4, C_2H_6 and C_3H_6. No evidence was found for the formation of oxygenated products, e.g., C_3H_8O (acrolein). Fig. 5.4 shows the distribution of products, at 650 °C, while maintaining a pO_2 of 0.8 atm at the feed side of the membrane. Also shown in the figure are corresponding data from pyrolysis experiments in an empty reactor (referred to as blank experiments). Comparison of the data sets makes clear that under the conditions of the experiments there is a significant contribution from gas phase reactions. Besides H_2O, combustion products CO_x are formed when oxygen is fed to propane via the LNV10 membrane.

In Fig. 5.5 (a), the product concentrations are plotted against the oxygen flux. The latter was varied by maintaining different oxygen partial pressures, in the range 0.1-0.8 atm, at the feed side of the membrane during the experiments. The results show that the oxygen concentration at the reaction side remains virtually zero, while the formation of all products, including H_2O and CO_x, increases with increasing the oxygen flux.

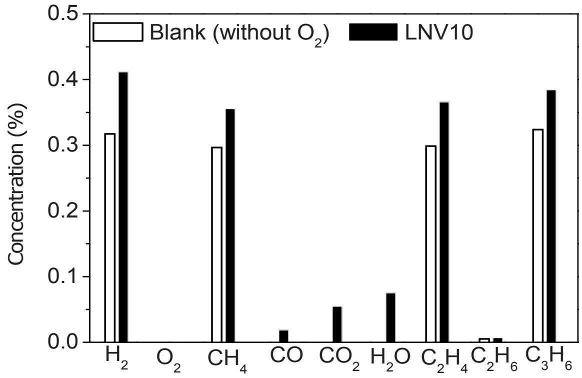

Fig. 5.4 Product distribution in ODH of propane, at 650 °C, from experiments using the LNV10 membrane reactor. Reactant side: 10 % C_3H_8 (NTP 10 ml min^{-1}), feed side: pO_2 = 0.80 atm. Also shown are corresponding results of propane pyrolysis experiments (blank), at 650 °C, performed in an empty quartz reactor.

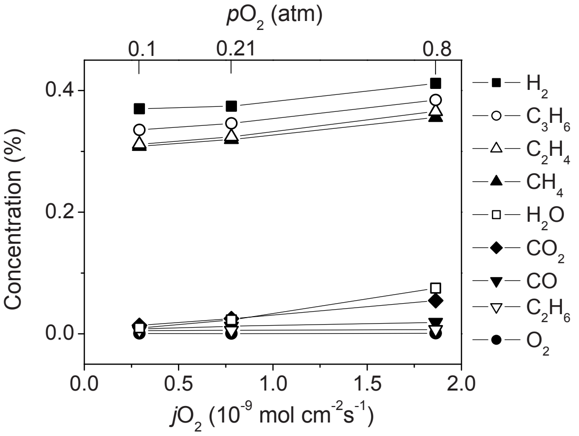

(a)

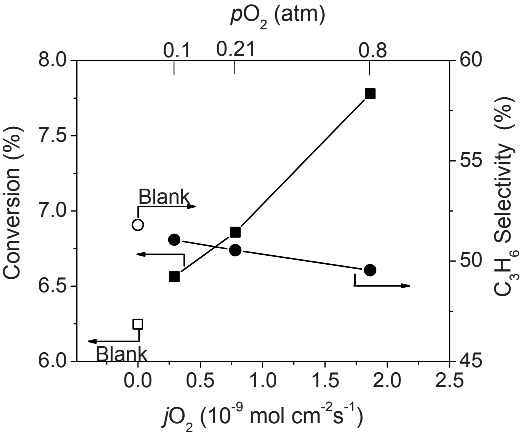

(b)

Fig. 5.5 Catalytic performance of the LNV10 membrane reactor in ODH of propane, at 650 °C, as a function of the oxygen permeation flux (jO_2); (a) product distribution, and (b) conversion and propylene selectivity. Reactant side: 10 % C_3H_8 (NTP 10 ml min^{-1}). Oxygen partial pressures maintained at the feed side of the membrane are indicated in the figures. Also indicated in Fig. 5.5 (b) are corresponding results from propane pyrolysis experiments (blank), at 650 °C, performed in an empty quartz reactor.

As shown in Fig. 5.5 (b), the conversion of propane increases concomitantly from 6.3 % to 7.8 %, without a significant change in the propylene selectivity. In the range of the experiments, the latter slightly decreases from 51.8 % to 49.5 %. The emerging picture is that, at given experimental conditions, the oxygen flux through LNV10 is too small, while the gas phase reactions are too prominent, to demonstrate the determining role of lattice oxygen on propylene selectivity.

Fig. 5.6 shows the reaction products upon passing propane through the BSCF membrane reactor, at 550 °C, while maintaining a pO_2 of 0.05 atm at the feed side of the membrane. Reaction products include H_2, CH_4, CO, CO_2, H_2O, C_2H_4, C_2H_6 and C_3H_6. As in the case of the LNV10 membrane reactor, no evidence is found for formation of oxygenated products. Also shown in Fig. 5.6 are data of thermal pyrolysis and ODH of propane, at 550 °C, in an empty reactor (referred to as blank experiments, without and with O_2, respectively).

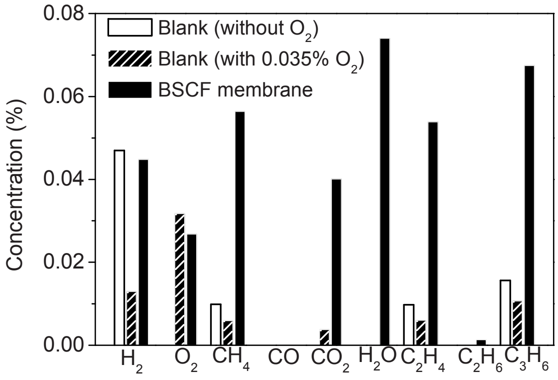

Fig. 5.6 Product distribution in ODH of propane, at 550 °C, from experiments using the BSCF membrane reactor. Reactant side: 10 % C_3H_8 (NTP 10 ml min^{-1}), feed side: $pO_2 =$ 0.05 atm. Also shown are corresponding data of thermal pyrolysis experiments (blank, without O_2) and ODH of propane (blank, with O_2), at 550 °C, performed in an empty quartz reactor.

It is generally accepted that the homogeneous gas phase reactions during ODH of alkanes occur via a free-radical chain mechanism [17]. Oxygen may be involved in the initiation reaction, e.g., through hydrogen abstraction from the alkane. Also, thermal cracking may generate free radical species, causing a large variety of successive elementary chain reactions [17]. The data presented in Fig. 5.6 suggests that, at given experimental conditions, amongst which the absence of a catalyst is considered important, molecular oxygen acts as a scavenger of free radicals. Compared to the data from pyrolysis experiments, addition of oxygen to the propane stream is found to lower propane conversion. The conversion is further lowered upon increasing the oxygen/ propane ratio in the gas phase, as can be judged from the data presented in Table 5.1. Under the conditions of the experiments with O_2, the oxygen consumption by gas phase reactions is limited. As seen in Fig. 5.6., free, i.e., unreacted, oxygen can still be detected, while only limited oxygen is traced back in the form of CO_2, but none in the form of H_2O. The situation alters when oxygen is supplied to the propane stream via the BSCF membrane. Although free oxygen can still be detected in the gas phase, significantly enhanced conversion to olefins (C_2H_4, C_3H_6) is found.

Table 5.1 Conversion and selectivity in thermal pyrolysis and ODH of propane, at 550 °C, performed in an empty quartz reactor.

Inlet gas composition	Conversion (%)	C_3H_6 Selectivity (%)
10 % C_3H_8/He	0.25	61.4
0.035 % O_2/8.64 % C_3H_8/ He	0.21	59.5
0.070 % O_2/7.20 % C_3H_8/He	0.15	63.6

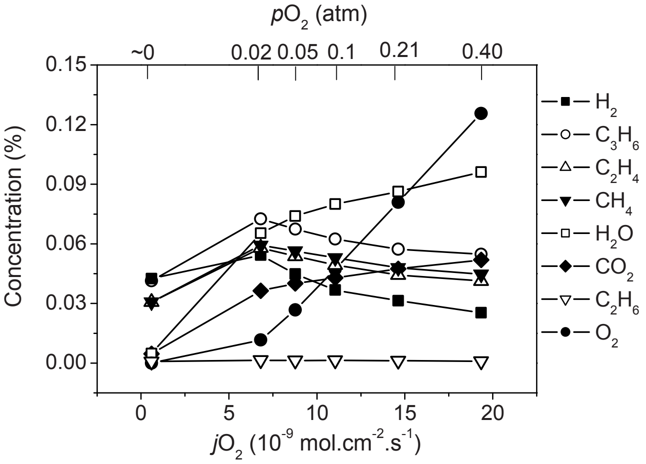

(a)

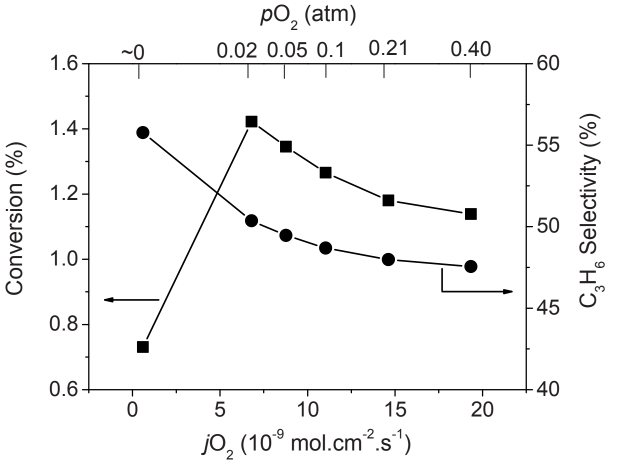

(b)

Fig. 5.7 Catalytic performance of the BSCF membrane reactor in ODH of propane, at 550 °C, as a function of the oxygen permeation flux; (a) product distribution, and (b) conversion and propylene selectivity. Reactant side: 10 % C_3H_8 (NTP 10 ml min^{-1}). Oxygen partial pressures maintained at the feed side of the membrane are indicated in the figures.

The data shown in Fig. 5.6 emphasize the catalytic role of BSCF in the dehydrogenation of propane. It is assumed that propyl radicals are generated at the BSCF surface involving a mechanism in which lattice oxygen is responsible for C-H bond activation, and one which is consistent with a Mars-van Krevelen redox mechanism [1]. The propyl radical desorbs as olefin with concomitant formation of H_2O. The presence of reaction products CH_4 and C_2H_4, however, indicate that under the conditions of the experiments gas phase reactions are active. The enhanced formation of CO_2, relative to the blank experiments in an empty reactor, i.e. in the presence of oxygen, suggests that CO_2 is essentially formed at the BSCF surface. Increasing the oxygen flux, by maintaining a higher oxygen partial pressure at the feed side of the BSCF membrane in a series of experiments, from $pO_2 = 0.02$ atm to $pO_2 = 0.40$ atm, as shown in Fig. 5.7, increases production of $CO_{2,}$ but lowers conversion of propane. The propylene selectivity is only slightly reduced. It thus emerges that the membrane-assisted catalytic conversion of propane is an interplay between operating constraints - like the number of sites at the surface, residence time, feed concentrations, etc. -, the oxygen flux, and the occurrence and extent of homogenous gas phase reactions. A distinct oxygen flux is required to achieve the desired conversion of the alkane into the corresponding olefin. A too high oxygen flux, however, leads to (*i*) unselective weakly-bonded adsorbed oxygen species, oxidizing alkyl radicals at the catalytic membrane surface, thereby producing CO_2, and (*ii*) increases the concentration of gaseous oxygen, limiting the extent of the gas phase reactions.

5.3.3 ODH of ethane using the BSCF catalytic membrane reactor

Few experiments were conducted to study the catalytic performance of the BSCF membrane reactor, at 650 °C, in ODH of ethane. Typical results obtained upon passing 40.5 % ethane, balanced with helium, through the reactor, while maintaining a pO_2 of 0.8 atm at the feed side of the BSCF membrane, are shown in Fig. 5.8. Quantifiable

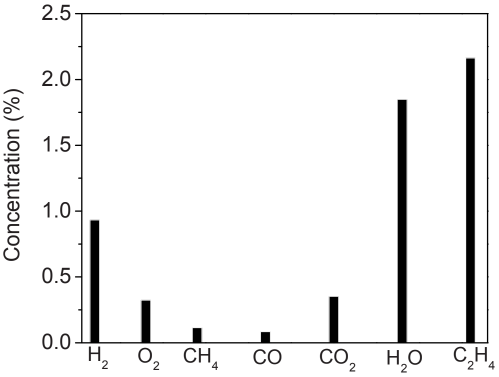

Fig. 5.8 Product distribution in ODH of ethane, at 650 °C, from experiments using the BSCF membrane reactor. Reactant side: 40.5 % C_2H_6 (NTP 10 ml min^{-1}), feed side: $pO_2 = 0.80$ atm.

reaction products at the exit of the reactor were H_2, CH_4, CO, CO_2, H_2O, and C_2H_4. Under the conditions of the experiments, ethane conversion was 6.09 % with ethylene selectivity of 87.7 %. Results of thermal pyrolysis experiments (blank experiments) carried out in an empty reactor are shown in Table 5.2. It is seen that the corresponding ethylene selectivities are close to 100 %, albeit that these are at low ethane conversions in the range 0.37-0.42 %, obtained using different feed concentrations of ethane (see Table 5.2). In accord with the data presented in Fig. 5.9, ethane conversion is found to increase pronouncedly if oxygen is fed via the BSCF membrane to the reaction side where the ethane is passed. The loss in ethylene selectivity observed in the membrane experiment, relative to that obtained during thermal pyrolysis in the empty reactor, is explained by the fact that the oxygen flux exceeds the rate of oxygen consumption by the catalytic reaction at the membrane surface. The presence of weakly adsorbed oxygen species in conjunction with gas phase oxygen lowers the overall ethylene selectivity.

Table 5.2 Conversion and selectivity derived from ethane pyrolysis experiments, at 650 °C, performed in an empty quartz reactor.

C_2H_6 (%)	Conversion (%)	C_2H_4 Selectivity (%)
25.3	0.42	99.6
42.9	0.41	99.5
61.6	0.39	99.5
81.0	0.37	99.4

Table 5.3 Catalytic performance of the BSCF membrane reactor in ODH of ethane, at 650 °C, using different inlet concentrations of ethane (NTP 10 ml min^{-1}). Feed side: pO_2 = 0.80 atm. Also given are the gas phase oxygen concentrations measured at the reaction side of the membrane.

C_2H_6 (%) Inlet concentration	Conversion (%)	Selectivity (%)	O_2 (%) at reaction side
24.3	3.48	78.8	1.18
40.5	6.09	87.7	0.32
57.2	5.31	90.1	0.17
73.9	4.40	91.5	0.11

In essence, this is confirmed by the results from measurements, in which either the inlet concentration of ethane was varied, i.e., at constant pO_2 at the feed side of the BSCF membrane, as listed in Table 5.3, or those in which the pO_2 at the feed side of the BSCF membrane was varied, i.e., at constant inlet concentration of ethane, as shown in Fig. 5.9. Both data sets demonstrate that the ethylene selectivity increases when the oxygen flux and rate of oxygen consumption by the catalytic reaction are better in balance. On the whole, the oxygen concentration both in the gas phase and on the surface of the catalyst membrane is crucial for determining the selectivity for ODH of ethane and propane.

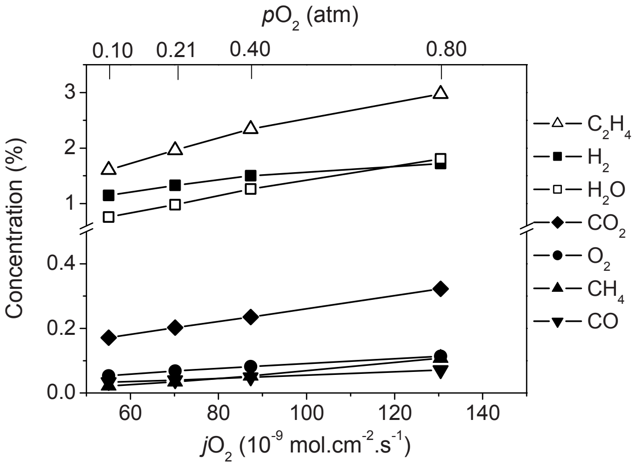

(a)

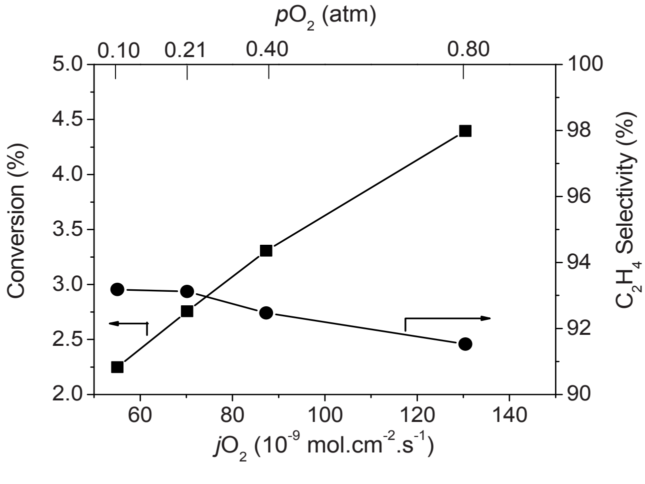

(b)

Fig. 5.9 Catalytic performance of the BSCF membrane reactor in ODH of ethane, at 650 °C, as a function of the oxygen permeation flux; (a) product distribution, and (b) conversion and ethylene selectivity. Reactant side: 73.9 % C_2H_6 (NTP 10 ml min^{-1}). Oxygen partial pressures maintained at the feed side of the membrane are indicated in the figures.

5.4 Concluding remarks

On the whole, the results show the dominating role of the oxygen flux across the membrane and that of available sites at the membrane surface in primary activation of the alkane and, hence, in achieving high alkane conversions. The results of ODH of propane and ethane on both membrane materials used in this study can be reconciled on the basis of Mars-van Krevelen type of kinetics, in which the alkane reacts with lattice oxygen on the membrane surface to produce the corresponding olefin. Evidence is also provided that, as expected, the oxygen concentration in the gas phase and the presence of weakly-bonded oxygen species on the membrane surface are crucial for determining the residual olefin selectivity. The latter emphasize the paramount importance to carefully match the oxygen flux with the rate of olefin production at the surface of the membrane.

References

[1] F. Cavani, N. Ballarini, A. Cericola, Oxidative dehydrogenation of ethane and propane: how far from commercial implementation?, Catal. Today, 127 (2007) 113-131.

[2] P. Botella, E. Garcia-Gonzalez, A. Dejoz, J.M.L. Nieto, M.I. Vazquez, J. Gonzalez-Calbet, Selective oxidative dehydrogenation of ethane on MoVTeNbO mixed metal oxide catalysts, J. Catal., 225 (2004) 428-438.

[3] S. Gaab, M. Machli, J. Find, R.K. Grasselli, J.A. Lercher, Oxidative dehydrogenation of ethane over novel Li/Dy/Mg mixed oxides: structure-activity study, Top. Catal., 23 (2003) 151-158.

[4] K. Karim, A. Mamedov, M.H. Al-Hazmi, N. Al-Andis, Oxidative dehydrogenation of ethane over MoVMnW oxide catalysts, React. Kinet. Catal. Lett., 80 (2003) 3-11.

[5] M.P. Lobera, S. Escolastico, J.M. Serra, High ethylene production through oxidative dehydrogenation of ethane membrane reactors based on fast oxygen-ion conductors, Chemcatchem, 3 (2011) 1503-1508.

[6] E. Morales, J.H. Lunsford, Oxidative dehydrogenation of ethane over a lithium-promoted magnesium-oxide catalyst, J. Catal., 118 (1989) 255-265.

[7] J.M.L. Nieto, P. Botella, P. Concepcion, A. Dejoz, M.I. Vazquez, Oxidative dehydrogenation of ethane on Te-containing MoVNbO catalysts, Catal. Today, 91-92 (2004) 241-245.

[8] R.K. Grasselli, Fundamental principles of selective heterogeneous oxidation catalysis, Top. Catal., 21 (2002) 79-88.

[9] P. Mars, D.W. van Krevelen, Oxidations carried out by means of vanadium oxide catalysts, Chem. Eng. Sci., 3 (1954) 41-59.

[10] V. Balcaen, I. Sack, M. Olea, G.B. Marin, Transient kinetic modeling of the oxidative dehydrogenation of propane over a vanadia-based catalyst in the absence of O_2, Appl. Catal., A, 371 (2009) 31-42.

[11] F.T. Akin, Y.S. Lin, Selective oxidation of ethane to ethylene in a dense tubular membrane reactor, J. Membr. Sci., 209 (2002) 457-467.

[12] M. Rebeilleau-Dassonneville, S. Rosini, A.C. van Veen, D. Farrusseng, C. Mirodatos, Oxidative activation of ethane on catalytic modified dense ionic oxygen conducting

membranes, Catal. Today, 104 (2005) 131-137.

[13] H.H. Wang, Y. Cong, W.S. Yang, Continuous oxygen ion transfer medium as a catalyst for high selective oxidative dehydrogenation of ethane, Catal. Lett., 84 (2002) 101-106.

[14] H.H. Wang, Y. Cong, W.S. Yang, High selectivity of oxidative dehydrogenation of ethane to ethylene in an oxygen permeable membrane reactor, Chem. Commun., (2002) 1468-1469.

[15] H.H. Wang, Y. Cong, X.F. Zhu, W.S. Yang, Oxidative dehydrogenation of propane in a dense tubular membrane reactor, React. Kinet. Catal. Lett., 79 (2003) 351-356.

[16] Z.P. Shao, G.X. Xiong, H. Dong, W.H. Yang, L.W. Lin, Synthesis, oxygen permeation study and membrane performance of a $Ba_{0.5}Sr_{0.5}Co_{0.8}Fe_{0.2}O_{3-\delta}$ oxygen-permeable dense ceramic reactor for partial oxidation of methane to syngas, Sep. Purif. Technol., 25 (2001) 97-116.

[17] M. Machli, C. Boudouris, S. Gaab, J. Find, A.A. Lemonidou, J.A. Lercher, Kinetic modeling of the gas phase ethane and propane oxidative dehydrogenation, Catal. Today, 112 (2006) 53-59.

Chapter 6

Evaluation and recommendations

Abstract

In this chapter, a brief evaluation is made on specific issues described in this thesis. Some recommendations for further research are suggested.

6.1 Measurement of the oxygen surface exchange rate

6.1.1 General

The pulse ^{18}O - ^{16}O isotope exchange (PIE) method introduced in this thesis enables investigation of the surface oxygen exchange rate of solid oxide ion and mixed ionic-electronic conductors. The method is fast compared with other methods, e.g., isotopic exchange depth-profiling [1], and therefore is considered highly suitable for screening studies of candidate cathode and/or membrane materials. Some aspects which deserve more attention include:

- *Mechanism of oxygen exchange*
  In general, the surface oxygen exchange rate is a function of the oxygen partial pressure, which is in part due to the involvement of electronic and ionic charge carriers in the reaction. Studying the oxygen exchange rate as a function of ambient oxygen partial pressure is considered to be a useful strategy to unravel the mechanism of the surface exchange reaction on different materials. Furthermore, the charge carrier concentrations may be varied by partial substitution of the materials under investigation with aliovalent dopants.
- *Influence of gas phase contaminations on surface exchange behavior* The PIE method is considered to be highly useful for *in-situ* studies on the effect of gas phase contaminations on the surface oxygen exchange rate. In this thesis, the effect of CO_2 on (stability and) surface oxygen exchange of $Ba_{0.5}Sr_{0.5}Co_{0.8}Fe_{0.2}O_{3-\delta}$ has been studied (see Chapter 4). In literature, numerous evidence has been collected that water vapor exerts an influence on the oxygen exchange kinetics. The PIE method is considered to be highly useful with regard to *in-situ* assessment of the role of water in the surface oxygen exchange kinetics.

6.1.2 Improvement of experimental set-up

The experimental set-up used in this thesis for pulse ^{18}O-^{16}O isotope exchange measurements may be improved. A novel scheme is proposed as shown in Fig. 6.1. Major advantages to the existing equipment (described in Chapter 2 of this thesis) include

1. Several cryogenic vessels (loaded with a zeolite absorbent) pre-filled with an $^{18}O_2/N_2$ gas mixtures with different oxygen partial pressure facilitates the study of oxygen exchange kinetics as a function of oxygen partial pressure. See 5, in Fig. 6.1.
2. Rather than $^{16}O_2$/He, $^{16}O_2$/Ar is used as the carrier gas. The choice for Ar, rather than He as the balance gas, prevents rapid diffusion of He in the $^{18}O_2/N_2$ pulse.

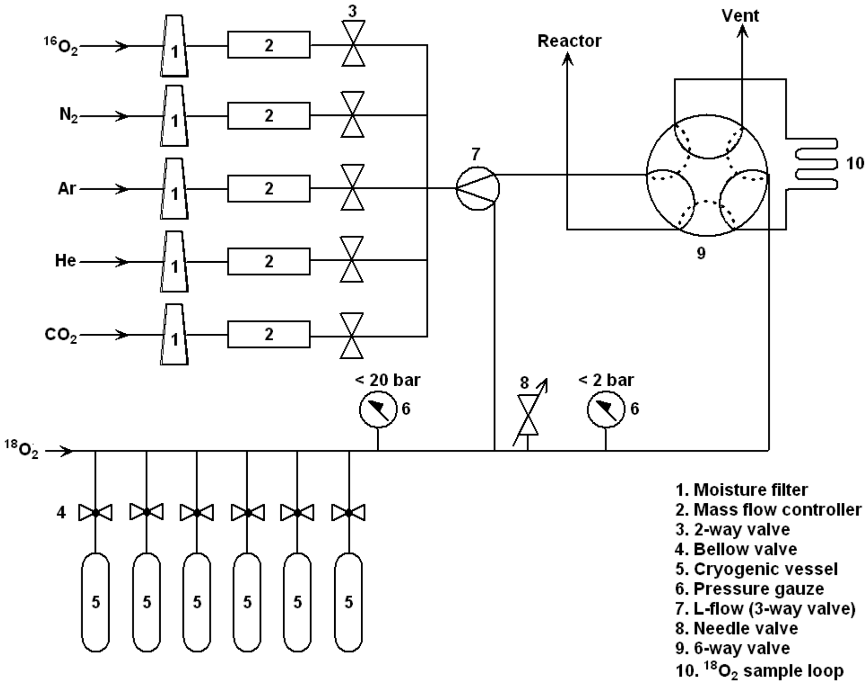

Fig. 6.1 Schematics of a novel set-up for pulse-response ^{18}O -^{16}O isotope exchange measurements.

3. A needle valve before and a vacuum pump after the pulse loop facilitates easy and non-wasteful filling of the loop with an $^{18}O_2$-containing gas mixture and, hence, saves costs. See 8, in Fig. 6.1.

Meanwhile, the above improvements have been realized in the author's laboratory by Yoo *et al*. More details are presented elsewhere [2]. A further improvement of the present equipment includes a mass spectrometer, which allows fast event studies at atmospheric pressures. A mass spectrometer with an improved response time and a faster sampling rate (e.g., 5 ms per point), not only allows application of smaller $^{18}O_2$-pulse volumes than employed currently (500 µl), but also improves accuracy of the experiments.

6.1.3 Accessible range of the surface exchange rate from PIE measurements

The surface exchange rate $\Re_0$ can be calculated from data of PIE measurements, using

$$\Re_0 = -\frac{2pO_2}{RS_r} \cdot \frac{F_0}{T_0} \ln\left(\frac{f_{g,o}^{18}}{f_{g,i}^{18}}\right) \tag{6.1}$$

where $f_{g,i}^{18}$ and $f_{g,o}^{18}$ are the ^{18}O fractions measured at the inlet and outlet of the reactor, F_0 [$m^3.s^{-1}$] is the flow rate at room temperature T_0 [K], S_r [m^2] the total surface area of the oxide powder in the packed bed available for surface exchange, and R the gas constant. Assuming that values of $f_{g,o}^{18} / f_{g,i}^{18}$ can be measured accurately in the range $0.04 < f_{g,o}^{18} / f_{g,i}^{18} < 0.96$, it follows from Eq. 2.11 that values of $\Re_0$ that can be deduced from experiment are in the range $4.3 \times 10^{-5} < \Re_0 < 3.3 \times 10^{-3}$ in [mol $O.m^{-2}.s^{-1}$]. This range corresponds to a temperature window in which $\Re_0$ is accessible from experimental data, as shown in Fig. 6.2. In calculation, typical values were used for the parameters listed in Eq. 6.1:

$S = 0.013$ m^2, $F_0 = 50$ NTP ml.min^{-1} and $pO_2 = 0.21$ bar

It is obvious that all of the listed parameters can be changed to alter the accessible temperature window. Care needs to be taken not to violate design criteria for the packed bed reactor [3], or to challenge the measurement of small surface areas using gas sorption techniques.

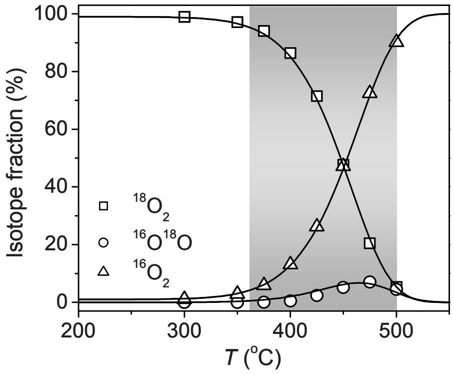

Fig. 6.2 Temperature dependence of the isotope fractions of $^{18}O_2$, $^{16}O^{18}O$ and $^{16}O_2$ from pulse ^{18}O-^{16}O isotope exchange measurements on $Ba_{0.5}Sr_{0.5}Co_{0.8}Fe_{0.2}O_{3-\delta}$. The grey area indicates the experimentally accessible temperature window (see text).

6.2 Membrane-assisted selective oxidation of alkanes

One of the challenges faced in catalytic membrane research, as was one of the aims of this PhD trajectory, is the oxygenation of alkanes to corresponding ketones or alcohols. In particular, major interest has arisen in the selective oxidation of propane to acrylic acid [4]. For selective oxidation, it is often hypothesized that lattice oxygen from the catalyst plays a crucial role. The latter has generated interest in the use of oxygen permeable membranes, which can provide a continuous and distributed supply of oxygen to the catalytically active membrane surface. A key challenge is therefore the development of membranes that allow operation at relatively low temperatures (< 600 °C) in order to avoid decomposition of oxygenates. Unfortunately, most of the currently known mixed ionic-electronic conducting oxides show appreciable levels of ambipolar conductivity at high temperature, which limit their application in many selective oxidation reactions. Besides the discovery of alternative materials with enhanced ambipolar conductivity, an obvious strategy to improve the oxygen fluxes at moderate temperatures is to decrease membrane thickness, and to develop ultra-thin-film supported membranes.

Another appealing strategy is the use of solid electrolytes, which show high enough oxide ion conductivity at moderate temperature (see Fig. 6.3). Abraham, Boivin and co-workers have demonstrated that the family of BiMeVOx electrolytes fulfills the requirement of high ionic conductivity at moderate temperatures [5, 6]. These materials are based upon $Bi_4V_2O_{11}$, where the V-ion has been partly substituted by a lower valent cation, e.g., Co, Cu or Ti. For instance, using a BiCoVOx membrane with gold grid electrodes on both sides enabled separation of oxygen with current densities up to 1000 $mA.cm^{-2}$ in the range of 430-600 °C [6]. The bismuth-based electrolyte itself may act as the catalyst or a known catalyst with high activity for oxygenation, such as BiMo or MoV catalysts - for which it has been claimed that lattice oxygen plays an important role in the catalytic activity [4, 7] - can be deposited on the surface of the electrolyte membrane.

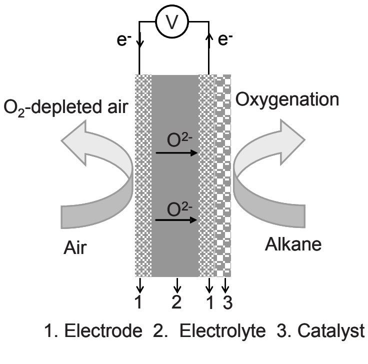

Fig. 6.3 Schematics of a ceramic membrane reactor, using an oxygen pump for the supply of oxygen to the reaction side.

References

[1] J.A. Kilner, B.C.H. Steele, L. Ilkov, Oxygen self-diffusion studies using negative-ion secondary ion mass-spectrometry (SIMS), Solid State Ionics, 12 (1984) 89-97.

[2] C.Y. Yoo, PhD thesis in press, University of Twente, Enschede.

[3] J. Perez-Ramirez, R.J. Berger, G. Mul, F. Kapteijn, J.A. Moulijn, The six-flow reactor technology - a review on fast catalyst screening and kinetic studies, Catal. Today, 60 (2000) 93-109.

[4] J.C. Vedrine, E.K. Novakova, E.G. Derouane, Recent developments in the selective oxidation of propane to acrylic and acetic acids, Catal. Today, 81 (2003) 247-262.

[5] F. Abraham, J.C. Boivin, G. Mairesse, G. Nowogrocki, The BIMEVOX series - a new family of high performances oxide ion conductors, Solid State Ionics, 40-1 (1990) 934-937.

[6] J.C. Boivin, C. Pirovano, G. Nowogrocki, G. Mairesse, P. Labrune, G. Lagrange, Electrode-electrolyte BIMEVOX system for moderate temperature oxygen separation, Solid State Ionics, 113 (1998) 639-651.

[7] M.M. Bettahar, G. Costentin, L. Savary, J.C. Lavalley, On the partial oxidation of propane and propylene on mixed metal oxide catalysts, Appl. Catal., A, 145 (1996) 1-48.

Summary

The research described in this thesis mainly aims at investigation of the rate of oxygen exchange at the surface of oxide ion conductors. Some distinct devices incorporating oxide ion conductors are presented in **Chapter 1**, emphasizing the importance of studying the oxygen surface exchange reaction.

A fast and simple method, referred to as pulse ^{18}O-^{16}O isotopic exchange (PIE), for measurement of the rate of surface exchange on oxide ion conductors has been developed in this PhD work, as described in **Chapter 2**. The method comprises measuring the response to feeding an ^{18}O-enriched gas phase pulse through a continuous flow packed-bed micro-reactor, loaded with the oxide powder, by on-line mass spectrometry. The method is used to measure the rate of oxygen exchange on yttria-stabilized zirconia (YSZ), $La_2NiO_{4+\delta}$, and $Ba_{0.5}Sr_{0.5}Co_{0.8}Fe_{0.2}O_{3-\delta}$ (BSCF). Analysis of the experimental data in terms of a two-step model for the isotopic exchange reaction shows that for the two mixed conductors, $La_2NiO_{4+\delta}$ and BSCF, the exchange reaction is limited by the rate of dissociative adsorption of O_2 molecules at the oxide surface, whilst for the solid electrolyte, YSZ, this reaction is competing with that of incorporation of adsorbed oxygen adatoms into the oxide lattice.

In **Chapter 3**, the PIE method is used for measurement of the oxygen exchange rate of phases $La_{1-x}Sr_xCoO_{3-\delta}$ (LSC). The observed power law dependence of the exchange rate on the concentration of oxygen vacancies in these phases, with exponent ~0.75, at $pO_2 = 0.21$ atm and $T = 500$ °C, emphasizes the importance of the oxygen vacancies in the kinetics of oxygen exchange for these materials. In **Chapter 4**, the PIE method is used for *in-situ* assessment of the role of CO_2 on the rate of oxygen exchange on BSCF. This rate is largely annihilated by the formation of a carbonate layer at the BSCF surface, but can be partially restored by thermal annealing of the oxide in a CO_2-free atmosphere

at 850 ^{o}C for 5 h.

In **Chapter 5**, the oxidative dehydrogenation (ODH) reactions of propane and ethane are investigated in a catalytic membrane reactor, incorporating oxygen-permeable membranes based upon $La_2Ni_{0.9}V_{0.1}O_{4+\delta}$ (LNV10) or $Ba_{0.5}Sr_{0.5}Co_{0.8}Fe_{0.2}O_{3-\delta}$ (BSCF). The results show the dominating role of the oxygen flux across the membrane and that of available sites at the membrane surface in primary activation of the alkane. The experimental data can be reconciled by the so-called Mars-van Krevelen mechanism, in which the alkane reacts with lattice oxygen to produce the corresponding olefin.

Finally, a brief evaluation of the work described in this thesis and some recommendations for further research are provided in **Chapter 6**.

Samenvatting

Het onderzoek beschreven in dit proefschrift richt zich hoofdzakelijk op de bestudering van de snelheid van zuurstofuitwisseling aan het oppervlak van zuurstofionengeleiders. Top of FormEen aantal verschillende devices waarin zuurstofionengeleiders zijn ingebouwd wordt besproken in **Hoofdstuk 1**, hiermee het belang van de bestudering van de oppervlakte-zuurstofuitwisseling benadrukkend.

Een snelle en eenvoudige methode, aangeduid als 'pulse isotopic exchange' (PIE) voor het meten van de snelheid van het oppervlakte-uitwisseling over oxide ion geleiders is ontwikkeld in dit PhD onderzoek, zoals beschreven in **Hoofdstuk 2**. De methode omvat de meting van de response op het doorleiden van een ^{18}O-verrijkte gasfase puls door een gepakt-bed-microreactor met continue doorstroming, geladen met het oxidepoeder, door middel van on-line massaspectrometrie. De methode wordt gebruikt om de snelheid van zuurstofuitwisseling te meten aan yttrium-gestabiliseerd zirconia (YSZ) $La_2NiO_{4+\delta}$ en $Ba_{0.5}Sr_{0.5}Co_{0.8}Fe_{0.2}O_{3-\delta}$ (BSCF). Analyse van de experimentele data in termen van een twee-stappen model voor de isotoop-uitwisselingsreactie laat zien dat voor de twee gemengde geleiders, $La_2NiO_{4+\delta}$ en BSCF, de uitwisselingsreactie beperkt wordt door de snelheid van dissociatieve adsorptie van O_2 moleculen aan het oxideoppervlak, terwijl voor het vaste-stof-elektrolyt, YSZ, deze reactie concurreert met de inbouwreactie van geadsorbeerde zuurstof-adatomen in het oxiderooster.

In **Hoofdstuk 3** wordt de PIE methode gebruikt voor meting van de snelheid van zuurstofuitwisseling aan het oppervlak van fasen $La_{1-x}Sr_xCoO_{3-\delta}$ (LSC). Het waargenomen exponentiële verband tussen de uitwisselingsnelheid en de concentratie van zuurstofvacatures in deze fasen, met exponent ~ 0,75, bij $pO_2 = 0{,}21$ atm en $T = 500$ °C, benadrukt het belang van zuurstofvacatures in de zuurstofuitwisselingskinetiek voor deze materialen. In **Hoofdstuk 4** wordt de PIE methode gebruikt voor *in-situ* beoordeling van de rol van CO_2 op de snelheid van zuurstofuitwisseling aan BSCF. Deze snelheid wordt grotendeels tenietgedaan door de vorming van een carbonaatlaag op het BSCF-oppervlak, maar kan gedeeltelijk worden hersteld door een warmtebehandeling van het oxide in een CO_2-vrije atmosfeer bij 850 °C gedurende 5 uur.

In **Hoofdstuk 5** worden de oxidatieve dehydrogenatie (ODH) reacties van propaan en ethaan onderzocht in een katalytische membraanreactor, waarin zuurstof-doorlaatbare membranen op basis van $La_2Ni_{0.9}V_{0.1}O_{4+\delta}$ (LNV10) or $Ba_{0.5}Sr_{0.5}Co_{0.8}Fe_{0.2}O_{3-\delta}$ (BSCF) geïntegreerd zijn. De resultaten tonen de dominerende rol aan van de zuurstofflux door het membraan en die van beschikbare plaatsen aan het membraanoppervlak in de primaire activering van het alkaan. De experimentele data kunnen in overeenstemming gebracht worden met het zogenaamde Mars-van Krevelen mechanisme waarbij het alkaan met roosterzuurstof reageert en het dienovereenkomstige olefine gevormd wordt.

Ten slotte, wordt in **Hoofdstuk 6** een beknopte evaluatie van het werk beschreven in dit proefschrift gegeven en een aantal aanbevelingen gedaan voor verder onderzoek.

Acknowledgements

I spent five years on finishing my Master and PhD studies, first in the group of Inorganic Materials Science and later in the group of Inorganic Membrane/Membrane Technology, the University of Twente.

I wish to express my gratitude to everyone who contributed to my thesis by scientific discussion, technical support, sample preparation, experimental measurements and personal suggestions etc.

Special thanks go to Dr. Henny J.M. Bouwmeester, my assistant promoter and important daily supervisor. I really appreciate your patience, guiding me step by step scientifically till I understand in which field I was digging. Thank you for your time which we spent together on discussion, talking and traveling. You are humorous and it is enjoyable with you.

Many thanks to Prof. Dr. Ir. Arian Nijmeijer, my promoter, for the support, the inspiring personalities and keeping eyes on me all the time.

Special thanks to ASPECT for the financial support. The joint project for this thesis was carried out with Drs. Salvatore Davide Crapanzano in the group of Catalytic Processes and Materials, the University of Twente. My appreciations also go to Prof. Dr. Ir. L. Lefferts, Dr. Barbara Mojet and Dr. I.V. Babich from CPM group for the fruitful discussion.

Special thanks to Dr. Yi Jianxin for the data measurement for Chapter 4. Many thanks to Dr. Zhu Jianjun and Dr. Ran Shen for useful discussion and suggestions.

Many thanks go to my colleagues and all the friends in the University of Twente. The time I spent with you is very great, it will be in my memory for ever.

I am truly grateful to my Chinese friends who meet me, know me, help me and care about me. When I came to the Netherlands alone, it is you who make me feel warm. We spent so much great time together on BBQ, cooking, playing cards and mah-jong, playing games, playing basketball and football, traveling, sharing the rent, singing, drinking and

talking etc. I must make an apology that I didn't mention your names here (maybe disappointing you), because first of all I don't want to miss any name, secondly, the name list is so long that I can not find a starting point. Believe that you are always in my heart. Please keep in touch wherever you are!

Finally, I express all gratitude to my wife, my parents and younger sister. My wife is always staying with me, taking care of me and encouraging me. My parents and younger sister always give me a strong support when I seek my dream.

Chunlin Song
University of Twente, Enschede

About the author

Chunlin Song was born on Jan. 10, 1979 (according to Chinese calendar) in a small village of Ziyang, Sichuan Province, China, surrounding by a lot of small mountains. He spent all the time in his hometown till he went to University of Science and Technology of China (USTC) (Hefei, Anhui) in 1996, studying in the Department of Materials Science and Engineering. After 4-year study, he graduated with two bachelor degrees: Materials Chemistry (major) and Computer Science and Technology (minor).

In 2000, he continued his master study in the group of Prof. Chusheng Chen, under the supervision of Associate Prof. Guoshun Jiang, focusing on porous materials, dense oxygen permeable membrane and proton conductor.

In 2003, he obtained the Master Degree of Engineering (Material Physics and Chemistry). Then he began to work in China Academy of Engineering Physics (CAEP) (Mianyang, Sichuan) as assistant engineer.

In 2004, he joined the group of Inorganic Materials Science in the University of Twente as a master student, focusing on the hydrothermal stability of porous silica membrane. In 2005, he obtained another Master Degree of Engineering (Chemical Engineering).

From 2005 to 2009, he began PhD study in the group of Inorganic Membrane/Membrane Technology, focusing on surface oxygen exchange and membrane reactor.

After PhD study, Chunlin Song went back to China and joined a company, in charge of R&D.